Numerical Algorithm to Compute the Effects of Breaking Waves on Surface Oil Spilled at Sea

A Final Report Submitted to

The Coastal Response Research Center

Submitted by

Mark Reed, Øistein Johansen, Frode Leirvik, and Bård Brørs

SINTEF Institute for Materials and Chemistry
Department of Marine Environmental Technology
Trondheim 7465
Norway

Project Period, 2007 - 2009

February 27, 2009
Revised April 30, 2009
Second Revision October 29, 2009

Coastal Response Research Center

This project was funded by a grant from NOAA/UNH Coastal Response Research Center.
NOAA Grant Number: NA04NOS4190063. Project Number: 07-060

UNIVERSITY of NEW HAMPSHIRE

NOAA NATIONAL OCEANIC AND ATMOSPHERIC ADMINISTRATION U.S. DEPARTMENT OF COMMERCE

SINTEF

SINTEF Materials and Chemistry

Address: NO-7465 Trondheim, NORWAY
Location: Brattørkaia 17B, 4. etg.
Telephone: +47 4000 3730
Fax: +47 930 70730

Enterprise No.: NO 948 007 029 MVA

SINTEF REPORT

TITLE

Numerical Algorithm to Compute the Effects of Breaking Waves on Surface Oil Spilled at Sea

AUTHOR(S)

Mark Reed, Øistein Johansen, Frode Leirvik, and Bård Brors

CLIENT(S)

NOAA/UNH Coastal Response Research Center

REPORT NO.	CLASSIFICATION	CLIENTS REF.	
SINTEF F10968	Confidential	Dr. Nancy Kinner	
CLASS. THIS PAGE	ISBN	PROJECT NO.	NO. OF PAGES/APPENDICES
Confidential		MK 800704	75 + 2 App.
ELECTRONIC FILE CODE		PROJECT MANAGER (NAME, SIGN.)	CHECKED BY (NAME, SIGN.)
final_report_sintef_natural dispersion_27-02-2009.doc		Mark Reed	Merete Moldestad
FILE CODE	DATE	APPROVED BY (NAME, POSITION, SIGN.)	
	2009-10-29	Tore Aunaas	

ABSTRACT

The purpose of this project has been to extend earlier work on the entrainment of oil into higher viscosity, non-Newtonian regions. The key deliverable is an algorithm for modeling natural entrainment of spilled oil at sea, extending the range of application beyond the 100 – 1000 cP limit of the earlier work. Equations were developed for droplet size distribution as a function of oil film thickness, wave amplitude, oil viscosity, and oil-water interfacial tension. Combined with equations for wave height and period as a functions of wind speed (plus fetch, depth and duration if desired), and whitecap coverage, an algorithm for natural dispersion is presented. This algorithm differs substantially from earlier work in that it is built up from a dimensional analysis of the problem, incorporating both the Weber number and a non-dimensional viscosity group.

KEYWORDS	ENGLISH	NORWEGIAN
GROUP 1	Environment, Modeling, Chemistry	Miljø, Modellering, Kjemi
GROUP 2	Oil, Marine Environment	Olje, Marint Miljø
SELECTED BY AUTHOR	Natural dispersion, Entrainment	Naturlig dispergering
	Droplet size distributions	Dråpestørrelsesfordeling
	Oil Spill Modeling	Oljeutslippsmodellering

Abstract

The purpose of this project has been to develop an algorithm for natural entrainment or dispersion of oil into the water column, working as much as possible from basic principles such as dimensional analysis. An additional goal has been to extend earlier work in this area (Delvigne et al., 1988, 1993, 1994) into higher viscosity, non-Newtonian regions. A secondary goal was to identify the transition between real dispersion (i.e. clouds of droplets being driven into the water column by breaking waves) with breakup and potential submergence of high-viscosity emulsions as globules or mats or patches, probable pre-cursers to tar balls.

Weathering and entrainment experiments were carried out for 3 oil types funded by this contract, plus 3 funded by a parallel project (see Acknowledgements below). Oil types ranged from a light paraffinic to a heavy fuel oil (IFO 380). Entrainment events were simulated using an overhead trough, calibrated to breaking waves in the experimental weathering flume. Droplet size distributions were recorded by high speed photography. Auxiliary data from a laser-diffraction instrument were used to investigate the distribution of droplet sizes below the 100 um limit of the photographic method. Several size distribution functions were investigated, with the lognormal function appearing to provide the best fit to the data.

Maximum energy levels achievable with the experimental setup proved insufficient to produce entrainment for the heaviest crudes and petroleum products, thus reducing the amount of data available for analysis and algorithm development. In addition, even the heaviest oils did not achieve densities exceeding seawater during the 14-day experimental period, such that sinking of oil was not observed. To the extent that entrainment could be induced with the heavier oils, the entrained forms tended to be primarily large (> 10 mm) but irregular bits and pieces, rather than nearly spherical droplets. These irregular oil/emulsion particles tended to return rapidly to the water surface. The bottom line here is that the energy levels available in the test flume were insufficient to allow us to map breakup and dispersion for oils or emulsions in with viscosities in excess of about 5,000 cP.

Equations were developed for droplet size distribution as a function of oil film thickness, wave amplitude, oil viscosity, and oil-water interfacial tension. Combined with equations for wave height and period as a functions of wind speed (plus fetch, depth and duration if desired), and whitecap coverage, an algorithm for natural dispersion is presented. This algorithm differs substantially from earlier work in that it is built up from a dimensional analysis of the problem, incorporating both the Weber number and a non-dimensional viscosity group. The algorithm is also valid for viscosities an order of magnitude higher than those from previous work.

The plunging jet method used in the present study has made it possible to significantly extend the investigated range of viscosities, compared to the studies reported earlier by Delvigne and collaborators. With droplet size data successfully obtained up to viscosities of about 5000 cP, we observed a smaller sensitivity to increasing viscosity than in Delvigne's studies. The effect of viscosity on droplet size was found to be small or negligible up to viscosities in the order of 1000 – 3000 cP, followed by an apparent exponential rise in sensitivity for viscosities above this range. However, since we are on the energy limit of the experimental method, extrapolations based on these observations are uncertain.

The algorithm developed here can be implemented in oil spill simulation models with applicability to spill response preparedness and decision-support for achieving more optimum spill response strategies. The results of this study will allow for improved trajectory analysis, since oil which is primarily subsurface (e.g. weathered oil in breaking wave fields) will be driven by currents more than directly by wind.

Acknowledgements

This project was funded by a grant from NOAA/UNH Coastal Response Research Center under NOAA Grant Number: NA04NOS4190063. Project Number: 07-060.

Additional data on natural dispersion of oil were supplied by a parallel project funded by StatoilHydro AS, Norske Shell A/S and Eni Norge AS.

SINTEF

Table of Contents

1.0 Introduction 1
2.0 Objectives 2
3.0 Methods 2
3.1 Measurements of droplet size distributions 2
3.2 Wave tank calibration experiments 12
3.3 Weathering flume experiments 14
3.3.1 Oils tested 14
3.3.2 Meso-scale laboratory testing 15
3.3.3 Solar simulation in the meso-scale flume 15
3.3.4 Sampling and analysis of surface oil 17
3.3.5 Collection of water samples 19
3.4 Plunging jet experiments 19
4.0 Results 21
4.1 Wave tank calibration experiments 21
4.2 Weathering flume experiments 24
4.2.1 Evaporative loss 25
4.2.2 Emulsion properties 28
4.2.3 Photo-oxidation 33
4.2.4 Submerging 34
4.2.5 Droplet size distributions over time 37
4.3 Plunging jet experiments 39
4.4 Algorithm for oil droplet size distribution 43
4.4.1 Delvigne's Studies 43
4.4.2 Theory of Droplet Formation 46
4.4.3 Size distribution functions 48
4.4.4 Empirical correlation for droplet size 52
4.4.5 Natural dispersion 56
5.0 Conclusions 60
5.1 Long term experiments 60
5.2 Natural dispersion experiments 61
5.3 Algorithm development 61
5.4 Limitations of the study 62
6.0 Discussion and Importance to Oil Spill Response/Restoration 63
7.0 Technology Transfer 63
8.0 Achievement and Dissemination 63
9.0 References 64
10.0 Appendix A: Laboratory Results from the meso scale flume experiments A1
10.1 Results from the meso scale flume experiments - figures A12
10.2 Results compared to predictions from the SINTEF OWM A17
10.3 Chemical analysis – SARA, FT-IR and chromatograms A23
10.4 Images from the flume experiments A30
11.0 Appendix B: Numerical Modeling of Floating Lumps B1
11.1 Background B1
11.2 Numerical model and setup B1
11.3 Simulations B1
11.4 Lumps in waves B2
11.5 Free-falling lumps B4

11.6 Free-falling water B8
11.7 Summary and conclusions B10

List of Figures

Figure 3.1. Sketch and photograph of the se- up for the breaking wave experiments. In the photograph, the semi-circular ends of the flume in its elliptical configuration can be seen to the right of the straight flume section in the foreground. 3
Figure 3.2 Meso-scale flume at SINTEF for long-term weathering studies of oils and petroleum products. 4
Figure 3.3 LISST-100x for measuring droplet sizes in the meso-scale flume. The instrument can be placed in situ or be used bench-top with a flow-through pump system. 4
Figure 3.4 Schematic of droplet size distribution measurement as planned with the LISST in situ. .. 5
Figure 3.5. Picture of the still photo rig used in the experiments. In some tests, two cameras were used, one for capturing the full size of the screen, and one for close ups (macro lens). Lamps were mounted on the rig to give sufficient light conditions. 6
Figure 3.6. Close up of inspection window with the white painted background screen mounted inside. 7
Figure 3.7. Close up of plunging jet arrangement. The water filled Plexiglas tray produces a plunging water jet when tilted to a horizontal position. The free fall height is adjusted by moving the container up or down in slides cut into the fastening board. 7
Figure 3.8. Picture of droplet cloud with a magnified excerpt of the analyzed picture showing identified droplets in white on a black background. 9
Figure 3.9 Feret's diameters, or maximum and minimum calipers, are the longest and shortest distances between any two points on the boundary of the object, measured in a straight line through the geometric center. The ratio of the Feret diameters is then a measure of roundness of the object, where a ratio of unity is a circle or sphere. 9
Figure 3.10 Identification of overlapping droplets in the image (red circles), versus single droplets included in the quantification (green circles). The objects encircled in red are filtered out, such that only the green encircled objects are carried further in the analysis. 10
Figure 3.11 Example identification of non-spherical droplets in the size range less than 0.4 mm. Those marked with red are eliminated from the analysis, while single droplets marked with green circles are included. 10
Figure 3.12. Example of number distribution plot of droplet size data (derived from picture shown in Figure 3.8). Top: Plot of cumulative number fraction vs. equivalent droplet diameter. Bottom: Linearized plot with standard deviations on the y-axis. The thin line shows a log-normal number distribution with logarithmic mean and standard deviations determined from the observed droplet size data. 11
Figure 3.13. Droplet number distribution from image analysis of picture # 6758 (markers) together with best fits of the log-normal (black line) and Rosin-Rammler (red line) distribution functions. The latter does not do well at the lower end, since it is weighted by volume rather than number. 12
Figure 3.14. Sketch of the set up of the breaking wave experiments. 13
Figure 3.15. Picture of modified flume. Inserted: picture of wave generator. 13
Figure 3.16 Schematic drawing of the meso-scale flume. 15
Figure 3.17 Measured wavelength spectrum compared to standard spectrum suggested in CIE publication 85 16
Figure 3.18 Daily Irradiation for some Norwegian cities through the year compared with the estimated daily irradiation in the meso scale flume. 16
Figure 3.19 Sampling schedule for weathering and droplet size distributions 17
Figure 3.20. Schematic drawing of experimental setup for the droplet break-up experiments in the weathering flume. The wave machine was stopped prior to the experiments and the oil

was confined against a barrier to form a homogeneous layer beneath the plunging water jet. 20
Figure 4.1. Time series of currents measured during a breaking wave experiment. The currents are measured 20 cm below water level 1 m downstream of the point of breaking. U_x is the axial component of the current, while U_z is the vertical. 21
Figure 4.2. Plot of droplet size distributions obtained in the Troll 150°C+ experiments. 22
Figure 4.3. Log-normal plot of the droplet size distributions obtained in the experiments with 50% water-in-oil emulsion of Troll 150°C+ oil. 23
Figure 4.4. Comparison of median droplet sizes observed in the calibration experiments. Results from the water-free oil (lighter colors) are shown behind the results from the 50 % water in oil emulsion (darker colors) 24
Figure 4.5 Relative importance of weathering processes with time. 25
Figure 4.6 Evaporative loss in the experiments with Troll with and without sunlight. Experimental results are compared with predictions from the SINTEF OWM. 26
Figure 4.7 Measured evaporative loss for all experiments (5°C above, 13°C below) 27
Figure 4.8 Maximum water content in the experiments plotted against maximum viscosity for the emulsions formed. 28
Figure 4.9 Water content in the experiments with Troll with and without sunlight. Experimental results are compared with predictions from the SINTEF OWM. 29
Figure 4.10 Measured emulsion viscosity for all experiments (5°C above, 13°C below). Viscosity is reported at shear rate $10s^{-1}$. 30
Figure 4.11 Predicted emulsion viscosity for the Troll crude from the SINTEF OWM compared with flume experiments at 5° with and without sunlight. 31
Figure 4.12 Measured emulsion viscosity for the Norne experiments compared to predictions from the SINTEF OWM. Viscosities are reported at shear rate $10s^{-1}$. The observed behavior of the viscosity is typical for waxy crude oils. The prediction curves are based on a sample of the Norne oil from 1998, with 13% wax content, as compared to 4.3% for the Norne oil sample from 2008, explaining the lack of agreement between the two. 32
Figure 4.13 Emulsion viscosity for the experiments with Troll at 5°C with and without solar simulation. Viscosity is reported at a shear rate of $10s^{-1}$ 33
Figure 4.14 Rise of a lump of emulsion formed in the experiment with IF380 at 13°C. 36
Figure 4.15 Position of the LISST during 20-hour recording of droplet size distributions during a weathering experiment 37
Figure 4.16 Changes in droplet size distributions over time during a 24-hour recording session with the LISST in situ. Maximum concentrations are recorded after 4 hours, after which time concentrations associated with droplets in the range 50 – 250 um are reduced. At about 4 hours the resurfacing of droplets starts to occur more rapidly than the introduction of new droplets through entrainment. The entrainment rate is reduced due to the increase in viscosity through evaporation and emulsification. 38
Figure 4.17 As in Figure 4.16, 3-dimensional view showing more clearly the rise and fall of the concentration of small droplets over the first 24 hours of the experiment. 38
Figure 4.18. Examples of pictures from plunging jet experiments with Troll crude at 13°C. Pictures of droplet clouds obtained in three subsequent pictures 1 hour after start of the flume test. Picture numbers are given to the right of each picture. Note that the picture sequence is obtained within a time period of about 5 seconds. 41
Figure 4.19. Droplet number distribution obtained from the three subsequent picture frames shown in Figure 4.18. The thick black line shows the distribution obtained from a combination of the three data sets. 42

Figure 4.20. Droplet number distribution in bins (d = 0.1 – 0.2 mm, 0.2 – 0.3 mm etc.) obtained from digital analysis of picture # 6758 from Figure 4.18. Bars in light colors are based on counts of all objects, while a roundness criterion R > 0.8 is applied to the bars shown in dark colors. Note that in both cases, the number fractions in each bin are relative to the total number of identified objects before application of the roundness criterion. The large number of rejects in the smallest bin reflects the rejection of background particles in the seawater. 42
Figure 4.21. Variation of dispersion coefficient with oil viscosity. Data from plunging jet experiments (Delvigne and Hulsen, 1994). The attached drawing describes the experimental setup. 45
Figure 4.22. Cumulative droplet number distributions obtained from plunging jet experiments with Troll crude at 5 ^{o}C. Markers show droplet diameters from image analysis scaled by the logarithmic mean diameter (D_{50}).The data points are from one of the plunging jet experiments conducted 6 hours after start of the flume test. The red line is a lognormal distribution with logarithmic standard deviation s = 0.42, while the blue line is a Double Pareto distribution with α = 1.2. 49
Figure 4.23. Example of application of upper log-normal distribution to droplet size data. See text for details. 51
Figure 4.24. Computed change in a droplet size distribution due to settling. Thick lines refer to number distributions, while thin lines are used for volume distributions. The initial distributions are shown in black, while the distributions obtained after a certain settling period are shown in red. Although there are relatively few large droplets, they represent a larger fraction of the total volume, and settle out most rapidly. 51
Figure 4.25. Regression plot of computed vs. observed median droplet size. The dashed lines represent +/- 20% deviations. The fit is based on a value of exponent p = 0.5. Data used in the correlation are shown with filled markers. 54
Figure 4.26. Plot of the coefficient $F = D_{50}/D^*$ versus the viscosity group Vi. The line represents an exponential function with parameters as defined in the text. 54
Figure 4.27. Plot of the viscosity factor as a function of viscosity number. The data points are computed from the dispersion coefficient data reported by Delvigne and Hulsen (1994) (see text for details). The red line shows an exponential curve fit to the data, while the black line shows the viscosity factor obtained from the experiments reported here. 55
Figure 4.28. Remaining mass of oil and emulsion predicted by SINTEF OWM (lines with markers), compared with computations based on the new droplet size distribution model (unmarked lines). The different curves are computed with different coefficients in the exponential viscosity function (see text for more details). 58
Figure 10.1 Measured evaporative loss for all experiments (5°C above, 13°C below) A12
Figure 10.2 Measured water content for all experiments (5°C above, 13°C below) A13
Figure 10.3 Measured emulsion viscosity for all experiments (5°C above, 13°C below). Viscosity is reported at shear rate $10s^{-1}$. A14
Figure 10.4 Measured yield stress for all experiments (5°C above, 13°C below) A15
Figure 10.5 Measured emulsion density for all experiments (5°C above, 13°C below) A16
Figure 10.6 Measured evaporative loss for the Norne experiments compared to predictions from the SINTEF OWM. A17
Figure 10.7 Measured evaporative loss for the Troll experiments compared to predictions from the SINTEF OWM. A18
Figure 10.8 Measured water content for the Norne experiments compared to predictions from the SINTEF OWM. A19
Figure 10.9 Measured water content for the Troll experiments compared to predictions from the SINTEF OWM. A20

Figure 10.10 Measured emulsion viscosity for the Norne experiments compared to predictions from the SINTEF OWM. Viscosities are reported at shear rate $10s^{-1}$. A21
Figure 10.11 Measured emulsion viscosity for the Troll experiments compared to predictions from the SINTEF OWM. Viscosities are reported at shear rate $10s^{-1}$. A22
Figure 10.12 Chromatograms from the flume experiment with Norne at 13°C and artificial sunlight A25
Figure 10.13 Chromatograms from the flume experiment with Norne at 5°C and artificial sunlight A26
Figure 10.14 Chromatograms from the flume experiment with Norne at 5°C and no sun A27
Figure 10.15 Chromatograms from the flume experiment with Troll at 5°C and artificial sunlight A28
Figure 10.16 Chromatograms from the flume experiment with Troll at 5°C and no sun A29
Figure 10.17 Images at various times in the flume experiment with Troll at 5°C and artificial sunlight. A30
Figure 10.18 Images at various times in the flume experiment with Troll at 5°C and no sunlight. . A31
Figure 10.19 Images at various times in the flume experiment with Troll at 13°C and artificial sunlight. A32
Figure 10.20 Images at various times in the flume experiment with Norne at 5°C and artificial sunlight. A33
Figure 10.21 Images at various times in the flume experiment with Norne at 5°C and no sunlight. A34
Figure 10.22 Images at various times in the flume experiment with Norne at 13°C and artificial sunlight. A35
Figure 10.23 Images at various times in the flume experiment with Kobbe at 5°C and artificial sunlight. A36
Figure 10.24 Images at various times in the flume experiment with IF 380 at 13°C and artificial sunlight. A37
Figure 10.25 Images at various times in the flume experiment with Grane at 13°C and artificial sunlight. A38
Figure 10.26 Images at various times in the flume experiment with IF180 at 13°C and artificial sunlight. A39
Figure 10.27 Images at various times in the flume experiment with North Slope at 13°C and artificial sunlight. A40
Figure 11.1 Snapshot from single lump simulation. The colour shows x-component of velocity. B1
Figure 11.2 Initial position of oil lumps in wave simulation. Colour denotes x-component of velocity. Double-click figure for animation. B3
Figure 11.3 Initial position and animation of free-falling oil lump simulation. Colour denotes z-component of velocity. Case: D = 0.2 m, h = 0.4 m, ρ = 984 kg/m^3, ρ_w =1025 kg/m^3 (density of lump 4 % less than water). Double-click figure for animation. B4
Figure 11.4 Snapshots from simulation with free-falling oil lump. Colours represent the vertical component of the fluid velocity. Case with D = 0.2 m, h = 0.4 m, ρ = 984 kg/m^3, ρ_w = 1025 kg/m^3. .....B5
Figure 11.5 Vertical position and velocity of free-falling lump. Comparison of Flow-3D result (full line) with result from (1). Scaling with lump diameter D and max free-fall velocity $u_0 = (2gh)^{½}$. Two different cases with parameters as indicated. B6
Figure 11.6 . Maximum submergence depth (upper plot) and time (lower plot) of a falling lump as a function of density difference and height. Computed from (1) with D = 0.2 m and ρ_w = 1025 kg/m^3. .....B7
Figure 11.7. Snapshots from simulation with water free-falling on oil lump. Colours represent the vertical component of the fluid velocity. Case with D = 0.2 m, h = 0.4 m, ρ = 984 kg/m^3, ρ_w = 1025 kg/m^3. .....B8

Figure 11.8 Vertical position and velocity of oil lump being hit by free-falling water. Scaling with lump diameter D = 0.2 m and max free-fall velocity $u_0 = (2gh)^{1/2}$ = 2.8 m/s. Case as Figure 11.7. .....B9
Figure 11.9 Initial position and animation of free-falling water hitting oil lump simulation. Colour denotes z-component of velocity. D = 0.2 m, h = 0.4 m, ρ = 984 kg/m^3, ρ_w =1025 kg/m^3 (density of lump 4 % less than water). Double-click figure for animation. B10

List of Tables

Table 3.1 Oils used in the flume experiments.....14
Table 3.2. Overview of experimental variables.....20
Table 4.1. Results for Troll 150°C+, water free 22
Table 4.2. Troll 150°C+, 50 % water content 23
Table 4.3Physical properties for two samples from each of the Troll experiments at 5°C (including viscosity of the wate- free residue). 34
Table 4.4 Calculated rising velocity for lumps of emulsion.....35
Table 4.5. Overview of experimental and analytic results 40
Table 4.6. Median droplet size data from flume experiments 53
Table 4.7. Predictions from SINTEF Oil Weathering Model.....58
Table 10.1 Results from flume experiment with the Troll crude at 5°C with artificial sunlight A1
Table 10.2 Results from flume experiment with the Troll crude at 5°C -no light A2
Table 10.3 Results from flume experiment with the Troll crude at 13°C with artificial sunlight ..A3
Table 10.4 Results from flume experiment with the Norne crude at 5°C with artificial sunlight ..A4
Table 10.5 Results from flume experiment with the Norne crude at 5°C -no sun. A5
Table 10.6 Results from flume experiment with the Norne crude at 13°C with artificial sunlight A6
Table 10.7 Results from flume experiment with the Grane crude at 13°C with artificial sunlight A7
Table 10.8 Results from flume experiment with the North Slope crude at 13°C with artificial sunlight A8
Table 10.9 Results from flume experiment with the IF180 at 13°C with artificial sunlight.....A9
Table 10.10 Results from flume experiment with the IF380 at 5°C with artificial sunlight.....A10
Table 10.11 Results from flume experiment with the IF380 at 13°C with artificial sunlight.....A11
Table 10.12 Results from the SARA analysis performed on a selection of samples from the meso scale flume experiments A23
Table 10.13 Results from FT-IR analysis - Ration of carbonyl and aromatic bands to aliphatic C-H bands.....A24

1.0 Introduction

Natural dispersion of oil spilled at sea is a key process in determining the expected lifetime on the sea surface of a specific crude oil or petroleum product under specific environmental conditions. How long the oil will remain on the sea surface is a key issue in evaluating alternative oil spill response strategies, determining the probability of impacting coastlines, and in estimating potential effects on sea birds and marine mammals in the path of the slick.

Existing algorithms used to compute the rate of natural dispersion, and the associated droplet size distribution, are weak, especially for higher viscosities. Early work in this area resulted in theoretical algorithms based on conceptual understanding of the problem (e.g. Mackay et al 1986, 1993; Buist and Potter, 1987; Lee et al, 1989, 1990), but equations were highly empirical and based on limited data. The first set of algorithms to include a prediction of the droplet size distribution based on oil properties was produced by Delvigne and Sweeney (1988, 1993, 1994). This work was limited to viscosities under 1000 cP, a value reached by most oils within a few hours on the sea surface.

For low-viscosity fresh oils, breaking waves tend to produce oil droplets in the water column, with increased energy, lower viscosity, and lower interfacial tension being associated with smaller droplet sizes. High energy input at this stage, as with a passing storm, may disperse the entire slick into the water column, such that only very thin oil sheens are seen after the storm passes.

For oil remaining on the sea surface and weathering, the viscosity increases due to evaporation and emulsification, and changes in the rheology become more important in determining the eventual fate of the oil. To the extent that the oil forms a plastic-elastic non-Newtonian emulsion, natural (or chemical) dispersion in the usual sense may not occur. In quiet weather such oils may be very nearly neutrally buoyant, and float at the water surface, and may be as much as 50 cm thick (ref. experience with Erika and Prestige fuel oil spills in Europe). In heavier weather, such oils will be more or less constantly over-washed, and driven subsurface in large patches or "carpets". These will eventually be torn apart into smaller and smaller pieces if enough energy is present, or may sink due to incorporation of organic or inorganic particles in the water column, or through interactions with bottom sediments in shallower waters.

As a starting point for the studies carried out here, the processes of natural dispersion and submergence are considered as two extremes, or realizations, of the interaction between a surface oil slick whose characteristics are constantly changing as weathering proceeds, and a turbulent hydrodynamic environment. To extend the previous work into higher viscosity regimes, including if possible actual sinking if oil, has been a primary challenge of this project.

2.0 Objectives

The purpose of this project has been to carry the experimental work on entrainment of oil started by Delvigne and Sweeney (1988, 1993, 1994) into higher viscosity, non-Newtonian regions.

The key deliverable is an algorithm or set of algorithms for modeling natural entrainment or dispersion of spilled oil at sea, if possible identifying the transition from real dispersion (i.e. clouds of droplets being driven into the water column by breaking waves) to breakup and potential submergence of high-viscosity emulsions in the form of globules, lumps, or mats.

The model algorithms developed here can be implemented in oil spill simulation models with applicability to spill response preparedness and decision-support for achieving more optimum spill response strategies. The results of this study will allow for improved trajectory analysis, since oil which is primarily subsurface will be driven by currents more than directly by wind.

3.0 Methods

In overview, the project has been based on three sets of activities and associated methodologies:

(1) Discrete single-event breaking wave tests using selected oils, and recording of droplet size distributions as a function of weathered state. These tests were carried out in a straight 5-meter long channel (*Figure 3.1*). Single breaking waves were created by a wave-maker recessed at one end of the channel. The location and size of the breaking wave was controlled by altering the frequency and amplitude of the wave-maker to provide a series of wave trains that converged at the desired location with the desired energy. This reproduced the basic strategy of Delvigne and Sweeney (1988), and supplied a basis for calibrating the "plunging jet" methodology to be used during the long-term weathering studies.

(2) Long-term weathering experiments were carried out in an elliptical oil weathering flume, actually a reconfiguration of the straight flume used in the first set of single wave breaking experiments (*Figure 3.2*). Using the flume in its elliptical configuration, with a plunging jet of water instead of the single breaking wave, allowed for repeated dispersion/over-washing experiment as the oil weathered over days and weeks.

(3) Statistical analysis of the resulting datasets, combined with an engineering dimensional analysis of the problem, produced a functional relationship among the measured parameters characterizing the weathered oils and the observed droplet/particle size distributions.

3.1 Measurements of droplet size distributions

Two methodologies for measurement of oil droplet size distributions in the water column were planned. The first was based on a laser-diffraction instrument (Sequoia LISST-100X, *Figure 3.3*), providing droplet concentration measurements in the 2.5 – 500 μm size range, and concentrations from 5 – 750 μl/l, either *in-situ* or *ex-situ*. The second methodology was based on high resolution, high speed photographic recording of droplet size distributions.

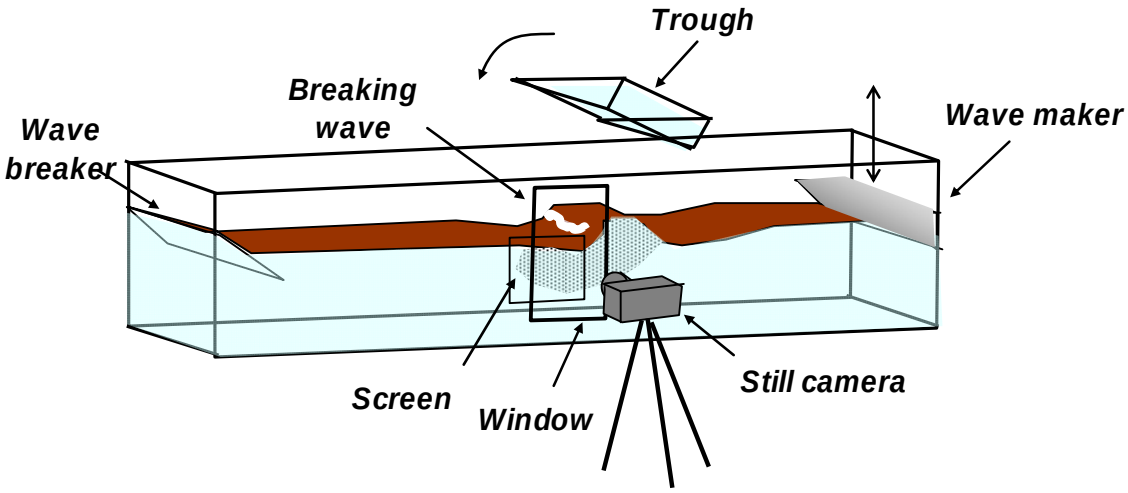

Figure 3.1. Sketch and photograph of the set-up for the breaking wave experiments. In the photograph, the semi-circular ends of the flume in its elliptical configuration can be seen to the right of the straight flume section in the foreground.

Here we used a Canon EOS 20D camera recording at 5 frames per second, with an image size of 3504x2336 pixels, a shutter speed of 1/1000 second at an aperture of F/18 and an ISO 1600. This second methodology covers droplet sizes down to about 100 µm . The two approaches together were therefore seen as complimentary, covering the entire range of droplet sizes of interest.

It was debated whether to place the LISST inside or outside the test tank. Placing the instrument *in-situ* (*Figure 3.4*) avoids the possibility of disturbing the sample when pumping the oil dispersion through tubing, with the possibility for adsorption of oil droplets on available surfaces, and coalescence of droplets during transport necessary for *ex-situ* measurements. The disadvantage of using the LISST-100X *in-situ* is the possibility of disturbing the structure of the breaking wave turbulence due to size of the instrument in relation to the flume.

Another potential disadvantage of *in-situ* measurements is the possible analytical interference from air bubbles generated together with oil droplets. The air bubbles will rise rapidly from the water column, leaving most of the oil droplets behind, and the experimental setup must reflect this, when planning the depth and timing (relative to the timing of the breaking wave event) of the measurements. The advantage of keeping the instrument outside the tank is the removal of possible disturbance of the turbulence process. Another advantage is establishment of more precise sampling points for measurements at different depths. It was eventually decided to place the LISST in the tank, but sufficiently downstream of the breaking wave such that the turbulence regime would not be affected.

Figure 3.2 Meso-scale flume at SINTEF for long-term weathering studies of oils and petroleum products.

Figure 3.3 LISST-100x for measuring droplet sizes in the meso-scale flume. The instrument can be placed in situ or be used bench-top with a flow-through pump system.

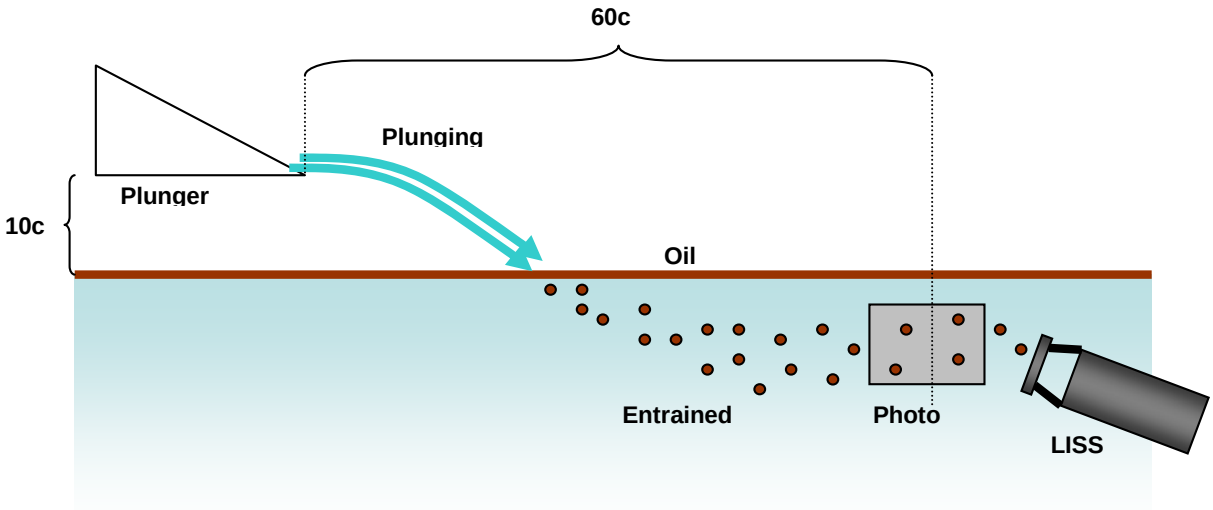

Figure 3.4 Schematic of droplet size distribution measurement as planned with the LISST in situ.

A major disadvantage of the LISST for this particular set of experiments proved to be the volume sampling rate. The processes of interest (wave breaking, droplet formation, droplet transport with turbulence) occur over a few seconds' time. The LISST can therefore sample only a small volume during this time interval, the droplet content of which will be very sensitive to the placement of the LISST in relation to the actual breaking wave. There is no way to get a synoptic measurement of the droplet size distribution with this instrument. In addition, the LISST became very rapidly fouled by the oil, requiring constant cleaning and re-positioning, and interfering further with the possibility to interpret the data. On the other hand, the instrument has been used to record the longer term buildup of smaller droplets in the flume during one weathering experiment, as discussed further in Section 4.2.5.

The photographic measurement of droplet size distributions was carried out with a still camera mounted in front of the observation window. This allowed for recording of a series of still pictures of the evolving cloud of droplets formed by the breaking wave or the plunging jet (Figure 3.5). A white painted screen was mounted 10 cm behind the observation window to serve as a background for the images of the droplets (Figure 3.6).

The plunging jet was generated by a water-filled Plexiglas tray that could be mounted at selected heights above the water surface of the tank. The tray contained 9 L of water when filled to the brim. The plunging jet was produced by tilting the tray to a horizontal position (Figure 3.7).

The pictures of the droplet clouds were analyzed with an automated picture analyzer (KS300, produced by Carl Zeiss Vision GmbH) to determine the droplet size distribution. A digital picture of a droplet cloud with a 3504 × 2336 pixel resolution was imported into the program. The whole picture, or just a section, was converted into a black and white image by manual adjustment of a threshold grey tone with the aim of eliminating disturbing features like shadows and air bubbles (Figure 3.8). The program then identified individual droplets as coherent white objects on a black background, and provided a data table with three basic parameters for each identified object: the length and width of the object measured in pixels in the x- and y-directions (Feret's diameters F_x and F_y (*Figure 3.9*), and the area A of the object measured in square pixels.

Figure 3.5. Picture of the still photo rig used in the experiments. In some tests, two cameras were used, one for capturing the full size of the screen, and one for close ups (macro lens). Lamps were mounted on the rig to give sufficient light conditions.

The maximum diameter of the droplet is found automatically by the program, and the length of the particle in the axis perpendicular to major axis is also reported. The ratio between the two is used as a measure for the roundness of the particle. An equivalent diameter D_e is derived from the reported area, presuming a circular shape. Most observed droplets formed from low viscosity oils are close to circular, but in some cases, two or more droplets may overlap in the picture, forming a clearly non-circular shape. Such "false" objects are eliminated by imposing a roundness criterion based on the ratio between the two's diameters (i.e. $0.8 < F_x/F_y < 1.2$). Moreover, in order to remove picture noise from the results, objects represented by less than a certain number of pixels can also be eliminated. Thus, in the present study, objects with $A \leq 2 \times 2$ pixels were excluded from the analyses.

Figure 3.10 and *Figure 3.11* demonstrate the filtering process, with the accepted droplets being outlines in green, and the rejected shapes outlined in red. In *Figure 3.10* it can be seen that overlapping droplets are in general successfully removed from the analysis. *Figure 3.11* focuses on droplets in the size range less than 40 μm, and shows that small air bubbles and irregular background shapes are excluded.

A scaling factor (true length of a pixel) was determined for each analyzed picture. The factor varied between 0.034 to 0.037 mm/pixel with a mean value of 0.035 mm/pixel. The equivalent diameter of the smallest accepted object based on the pixel number criterion given above will thus be about 0.1 mm. Objects fulfilling the chosen roundness and pixel number criteria are sorted in ascending order of the equivalent diameter to determine parameters defining the statistical distribution of the droplet diameters.

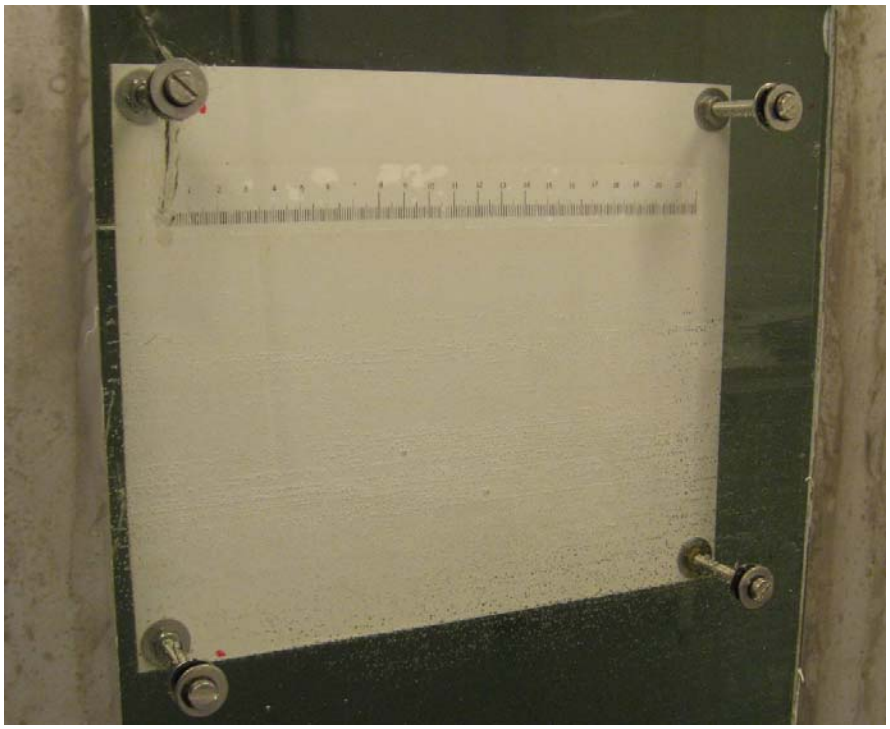

Figure 3.6. Close up of inspection window with the white painted background screen mounted inside.

Figure 3.7. Close up of plunging jet arrangement. The water filled Plexiglas tray produces a plunging water jet when tilted to a horizontal position. The free fall height is adjusted by moving the container up or down in slides cut into the fastening board.

Initial tests indicated that the droplet size data obtained in this way tends to follow a log-normal number distribution. A log-normal distribution can be depicted as a straight line in a graph where the logarithmic sizes are plotted on the x-axis and the values on the y-axis are given by the inverse normal distribution function NORMINV(P) where P is the cumulative number fraction corresponding to the given size (Figure 3.12). A fit of the data to a straight line can then be used to determine the parameters of the distribution (logarithmic mean value and standard deviation).

However, other distributions may also fit the data, as Lefebvre writes in his text book on Atomization and Sprays, p. 82 (Lefebvre, 1989):

> In the absence of any fundamental mechanism or model on which to build a theory of drop size distribution, a number of functions have been proposed, based on either probability or purely empirical considerations, to allow the mathematical representation of measured droplet size distributions. Those in general use include normal, log-normal, Nukiyama-Tanasawa, Rosin-Rammler, and upper limit distributions. As the basic mechanisms involved in atomization are not clearly understood and no single distribution function can represent all drop size data, it is usually necessary to test several distribution functions to find the best fit to any given set of experimental data.

Of the distribution functions mentioned above, the Rosin-Rammler is the one most widely used besides the log-normal distribution. Lefebvre refers to this function as a volume distribution function. However, we will assume that the function also can be used as a number distribution function by substituting volume fractions with number fractions. The function can be expressed by the equation $Q = 1 - \exp\left[-(d/X)^q\right]$, where Q is the volume fraction of droplets with diameter less than d, and X and q are constants. Actually, X is the diameter for which 63.2 % of the total volume is in droplets of smaller diameter.[1]

Figure 3.13 shows an attempt to fit the Rosin-Rammler distribution function to the number distributions obtained from the image analyses of one of the pictures. For comparison, a log-normal distribution based on the logarithmic mean diameter and standard deviation is shown at the same figure. As the figure indicates, the Rosin-Rammler function could be fitted to the upper 50% of the distribution, but this caused a significant overestimation of the number fractions in the smaller size range.

The Rosin-Rammler distribution function may be better suited for volume distributions, but in the present study, we have chosen to interpret the droplet size data from the image analyses directly in terms of number distributions. In this way we avoid the strong dependency on the few largest droplets that would result from a conversion to a volume distribution. The Rosin-Rammler distribution has therefore not been used in this analysis. A more detailed discussion of the log-normal distribution is presented in section 4.4.

[1] For $d = X$, $Q = 1 - \exp(-1) = 1 - 1/e = 0.632$

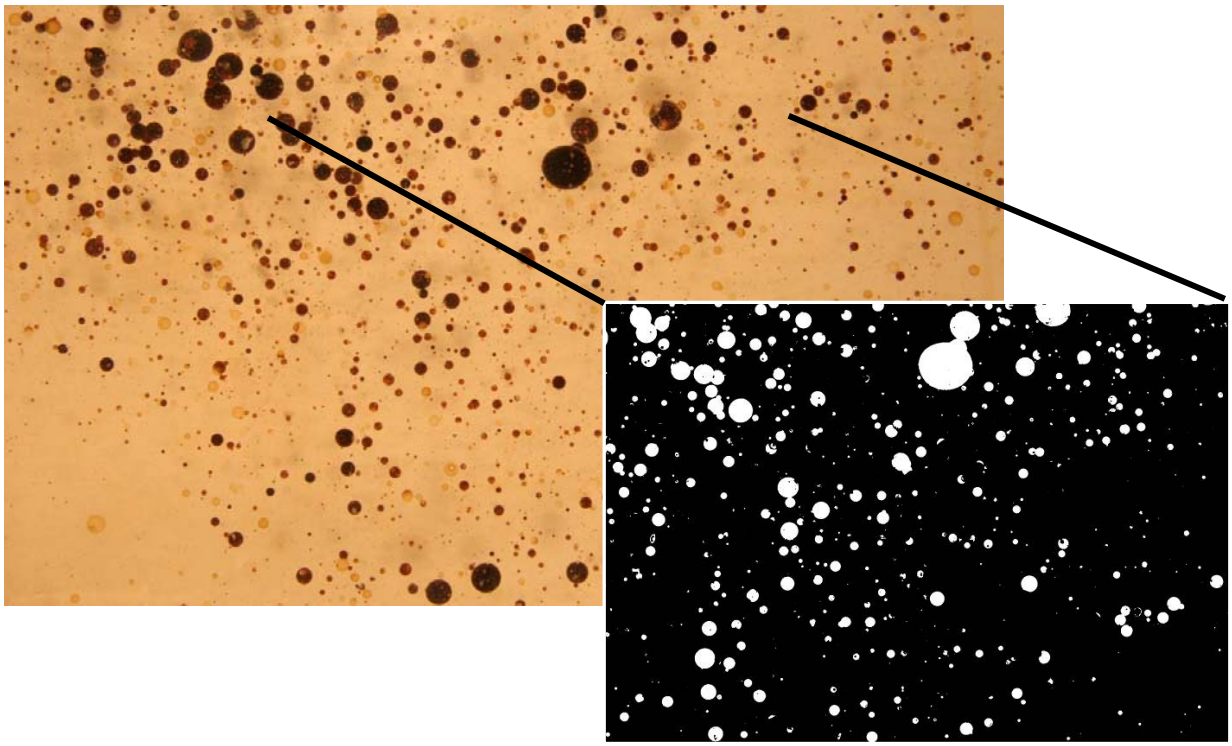

Figure 3.8. Picture of droplet cloud with a slightly magnified excerpt of the analyzed picture showing identified droplets in white on a black background.

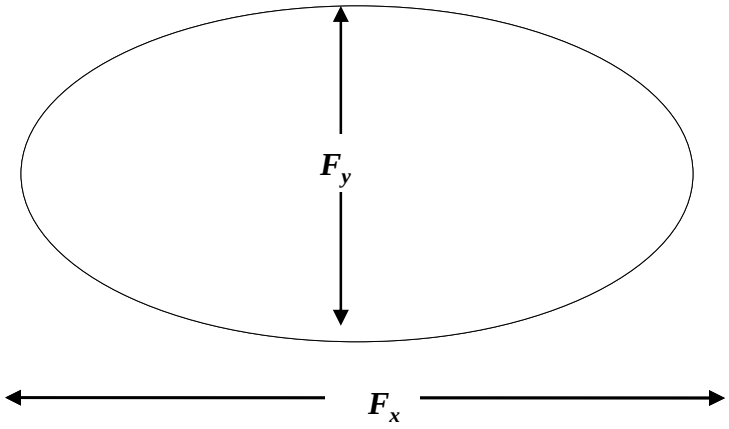

Figure 3.9 Feret's diameters, or maximum and minimum calipers, are the longest and shortest distances between any two points on the boundary of the object, measured in a straight line through the geometric center. The ratio of the Feret diameters is then a measure of roundness of the object, where a ratio of unity is a circle or sphere.

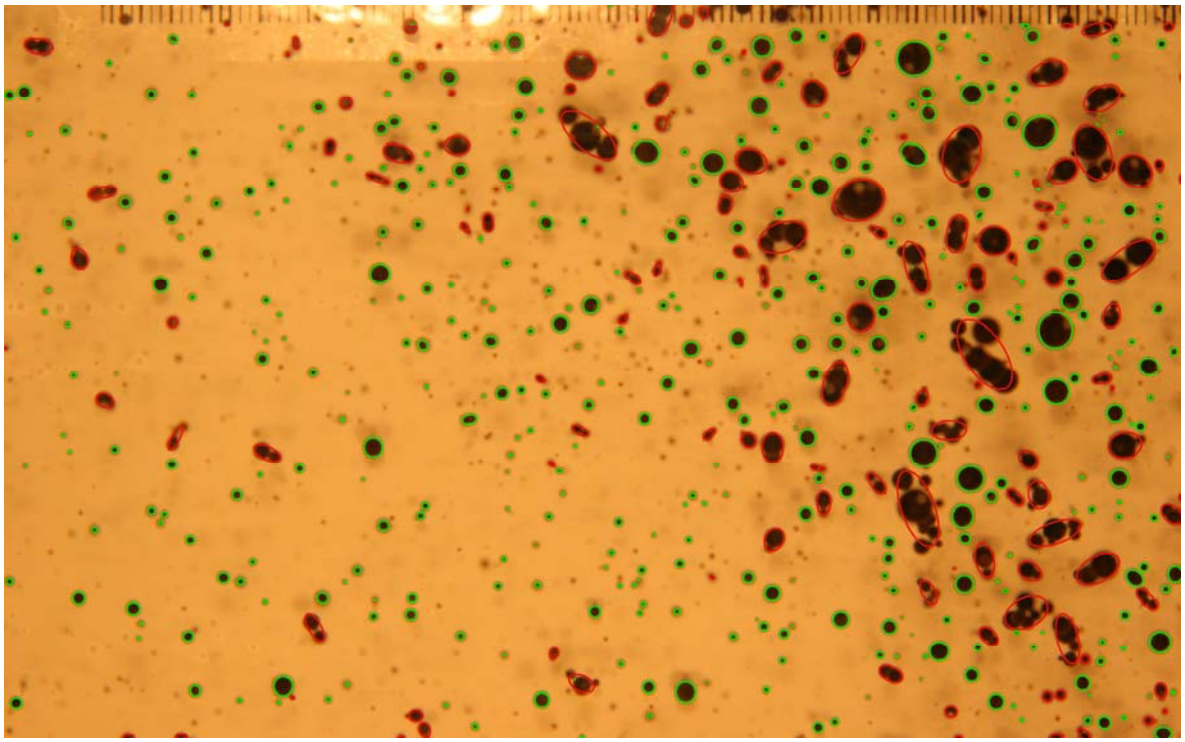

Figure 3.10 Identification of overlapping droplets in the image (red circles), versus single droplets included in the quantification (green circles). The objects encircled in red are filtered out, such that only the green encircled objects are carried further in the analysis.

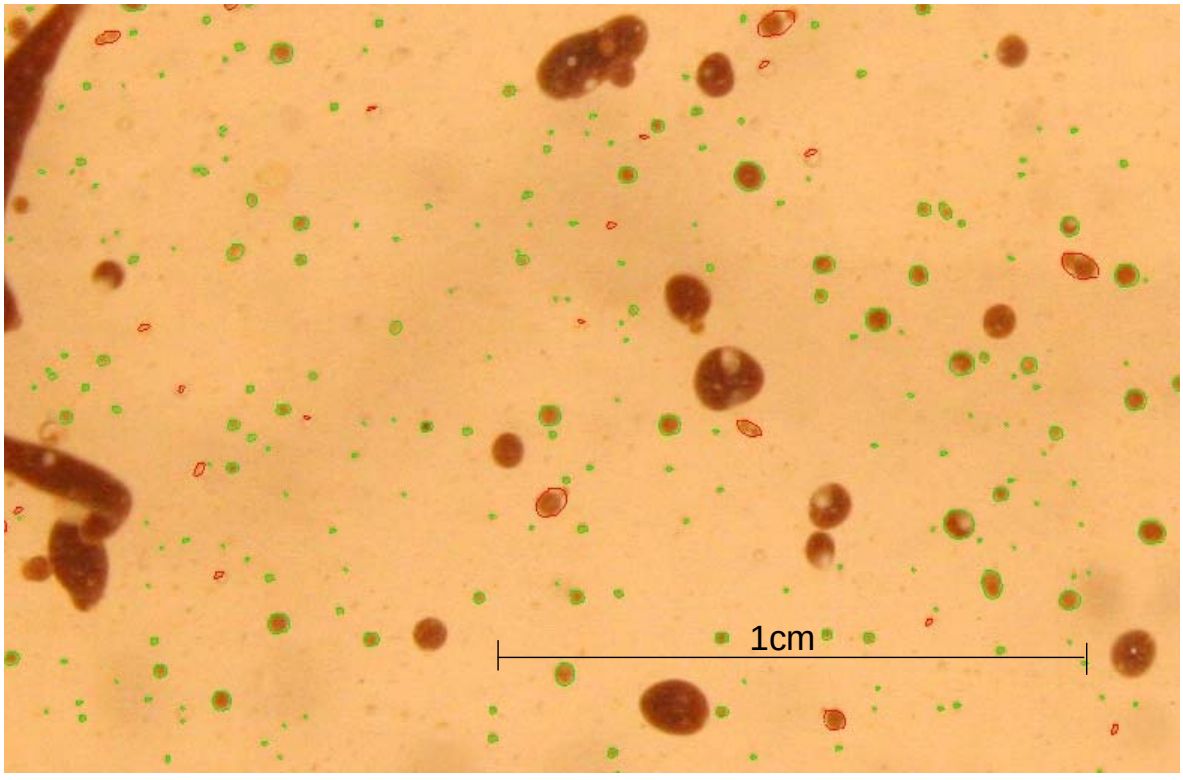

Figure 3.11 Example identification of non-spherical droplets in the size range less than 0.4 mm. Those marked with red are eliminated from the analysis, while single droplets marked with green circles are included.

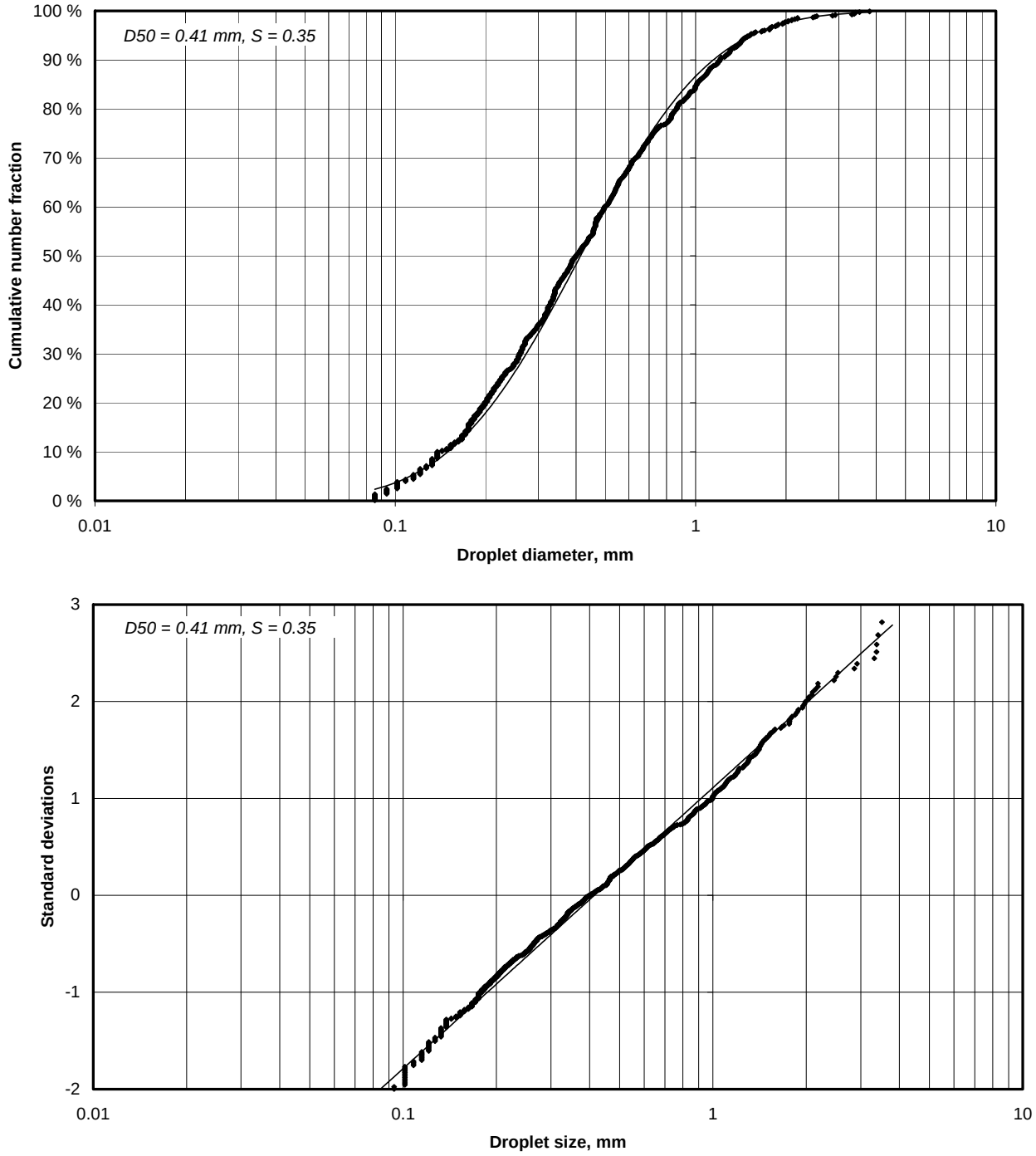

Figure 3.12. Example of number distribution plot of droplet size data (derived from picture shown in Figure 3.8). Top: Plot of cumulative number fraction vs. equivalent droplet diameter. Bottom: Linearized plot with standard deviations on the y-axis. The thin line shows a log-normal number distribution with logarithmic mean and standard deviations determined from the observed droplet size data.

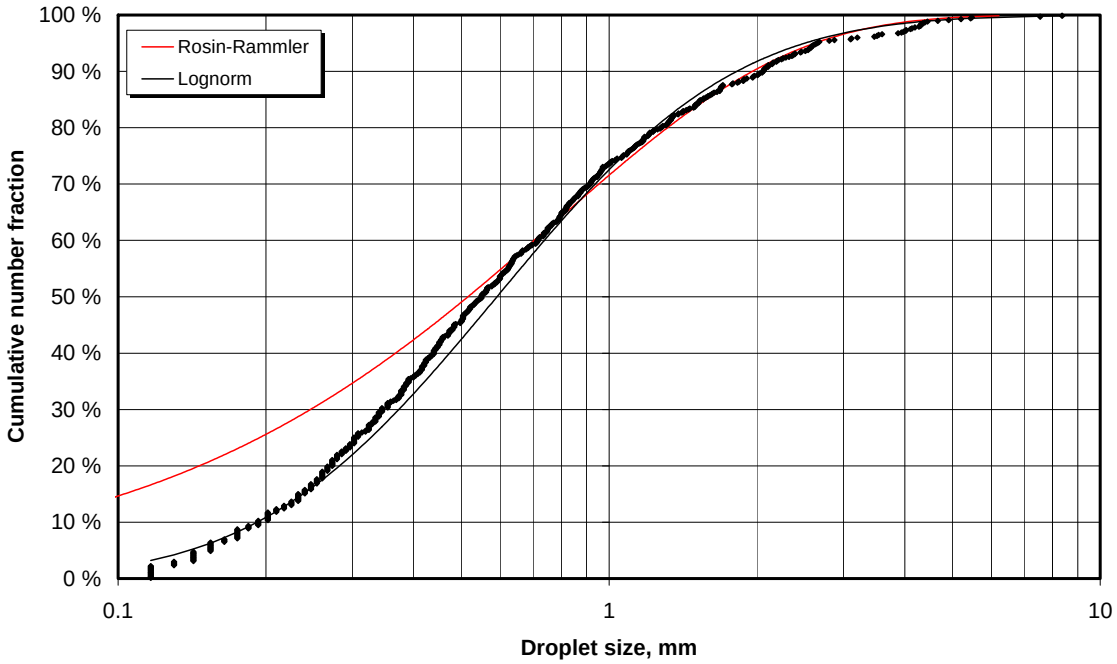

Figure 3.13. Droplet number distribution from image analysis of picture # 6758 (markers) together with best fits of the log-normal (black line) and Rosin-Rammler (red line) distribution functions. The latter does not do well at the lower end, since it is weighted by volume rather than number. The Rosin-Rammler distribution was therefore not used in this work.

3.2 Wave tank calibration experiments

This section presents results from a calibration study of oil droplet breakup experiments with plunging jets and breaking waves. The plunging jet test was developed for use in oil droplet breakup tests performed in situ during long term weathering studies in SINTEF's weathering flume. The object of the calibration experiments was to establish a relationship between oil droplet breakup in these tests and in breaking wave tests.

The objective of these experiments was to provide data for calibration of the plunging water jet tests to experiments with breaking waves. This was achieved by comparing droplet size distributions generated by breaking waves of a certain height with droplet size distributions generated by plunging jets with a certain free fall distance. The experiments were performed in a modified arrangement of SINTEF's meso-scale flume where the straight sections of the flume were mounted together to form a wave tank (canal) with a length of approximately 5 meters (Figure 3.14).

For this purpose, straight segments of the weathering flume were connected to form a straight wave flume with a length of 5 m. The flume was filled with water to a depth of 1 m, and covered with a 1 – 2 mm thick oil film. Oil droplet breakup was observed by close-up photography through an observation window mounted inside the flume. Breaking waves were obtained at the location of the observation window by adjusting the frequency and amplitude of a wave generator mounted at one end of the flume. Plunging water jets were obtained by tilting a water-filled tray mounted at different free fall heights above the oil-covered water surface of the flume.

The width of the tank was 0.5 m and the water level was adjusted to 1 m above the bottom. The programmable wave generator located in the right end of the tank was tuned to produce a single breaking wave at the location of the observation window. A wave breaking board was located at the

opposite end of the tank to eliminate/reduce wave reflection. The surface of the tank was covered with a thin layer of oil (1 - 2 mm). The breakup of the oil film into droplets was observed by a still camera mounted in front of the observation window. The pictures of the oil droplets were taken against a white screen mounted 10 cm inside the observation window.

The wave generator located at one end of the tank was programmed to produce a specific number of waves with a certain wave height and period (Figure 3.15). By adjusting these parameters, a spilling breaker of a certain height could be obtained at a suitable location in the flume.

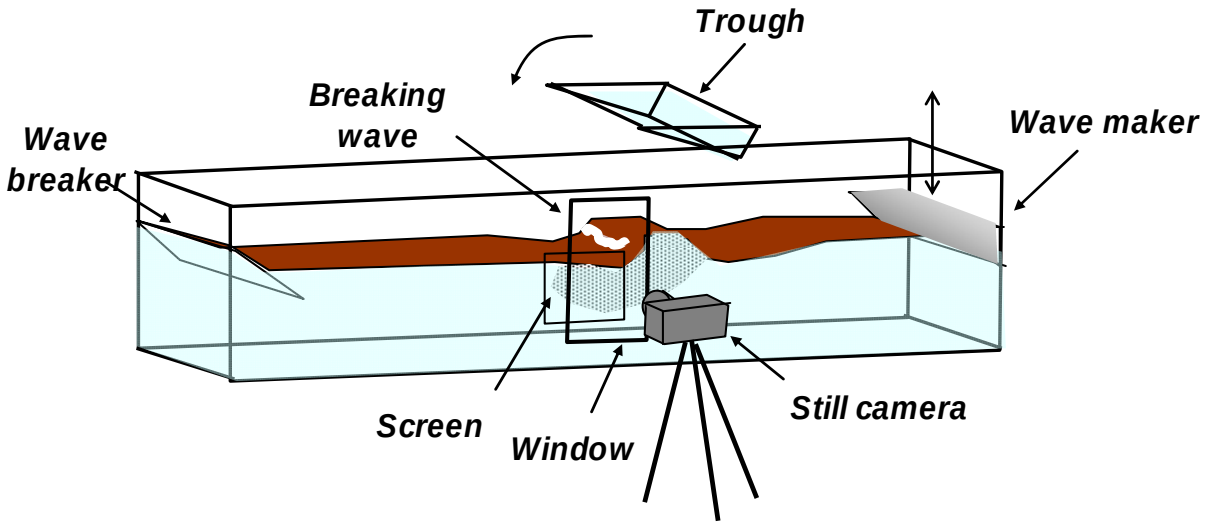

Figure 3.14. Sketch of the set-up of the breaking wave experiments.

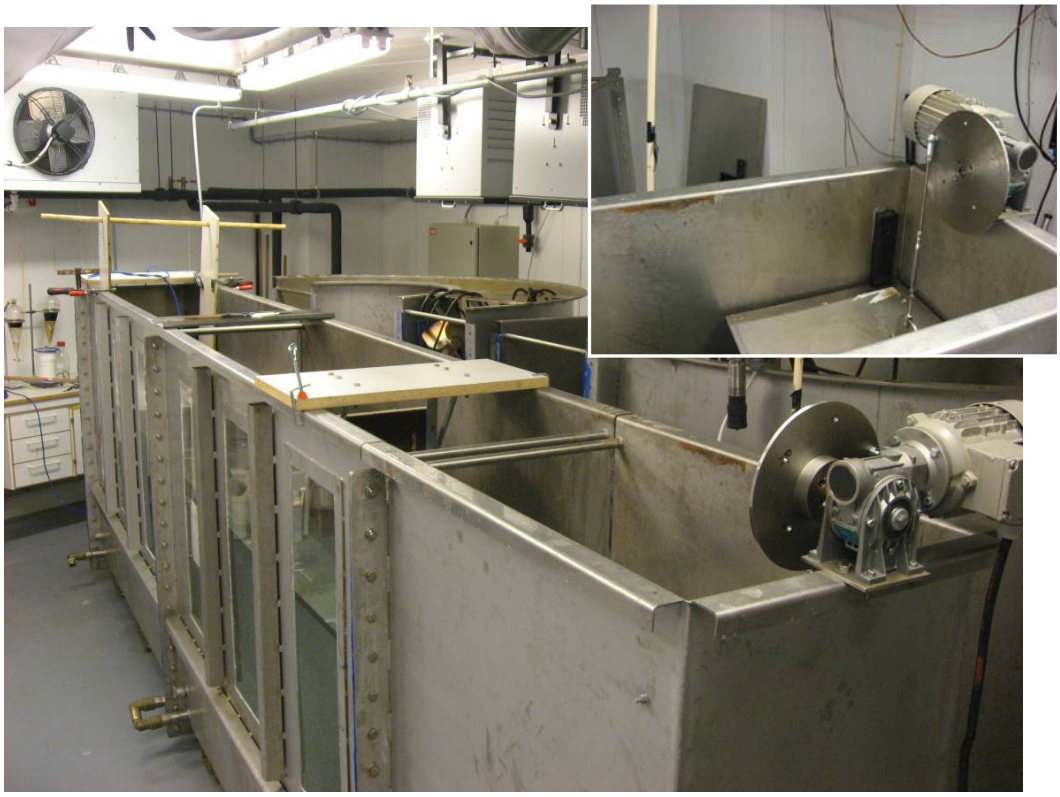

Figure 3.15. Picture of modified flume. Inserted: picture of wave generator.

3.3 Weathering flume experiments

This section describes:

- oils tested and the test conditions for the different experiments;
- experimental setup of the meso scale flume, and procedures for sampling;
- solar simulator, and
- analyses performed on the samples.

3.3.1 Oils tested

Crude oils can be characterized in four categories: asphaltenic, naphthenic, paraffinic and waxy. The oils tested were selected to represent different categories of oils. In addition to the crudes, two heavy fuel oils (IF180 and IF380) were also tested.

The oils tested in the flume experiments are listed in Table 3.1.

Table 3.1 Oils used in the flume experiments

SINTEF ID		Oil type	Wax (wt%)	Asphaltenes (wt%)	Pour point (°C)	Density (kg/m^3)
2007-0287	Troll	Naphthenic	0.9	0.04	-36	0.900
2007-0260	Norne	Waxy	4.3	0.30	21	0.860
2006-1125	IFO 380	Heavy fuel oil	5.0	3.4	15	0.963
2006-1060	Grane	Asphaltenic	-	-	-	0.941
2000-0594	IF180	Heavy fuel oil	-	-	-	0.956
2007-0361	North Slope	Paraffinic	-	-	-	0.852

11 flume experiments were performed:

- Troll 5°C with artificial sunlight (14 days)
- Troll 5°C no sun (10 days)
- Troll 13°C with artificial sunlight (14 days)
- Norne 5°C with artificial sunlight (14 days)
- Norne 5°C no sun (8 days)
- Norne 13°C with artificial sunlight (10 days)
- IFO380 at 5°C with artificial sunlight (10 days)
- IFO380 at 13°C with artificial sunlight (12 days)
- Grane 13°C with artificial sunlight (11 days)
- IFO 180 13°C with artificial sunlight (14 days)
- North Slope 13°C with artificial sunlight (14 days)

A 12th experiment was carried out with Kobbe, a light paraffinic crude oil, but this was a dispersibility test, with chemical dispersant applied after 2 days. The limited data from this oil is

therefore not included here. The Kobbe data may be of interest in the future, since Kobbe is a relatively wax-rich oil (3.5%), but much lighter than Norne, with 30% of the mass being lost to evaporation over the first hour. This would increase the wax content to about 5%, making it a candidate for development of a "waxy" variant of the entrainment algorithm developed here.

3.3.2 Meso-scale laboratory testing

The meso-scale flume basin (Singsaas *et al.*, 1993, Figure 3.16) located at SINTEF is routinely used to study the weathering processes simultaneously. This methodology allows for the interactions among weathering processes to take place in a relatively realistic fashion, but under controlled conditions. Approximately 4.8 m^3 seawater circulates in the 10 meter long flume. The flume is located in a climate-controlled room (0°C – 20°C). Two fans placed in a covered wind-tunnel allow various wind speeds. The evaporation rate can be calibrated to simulate a wind speed of 5-10 m/s.

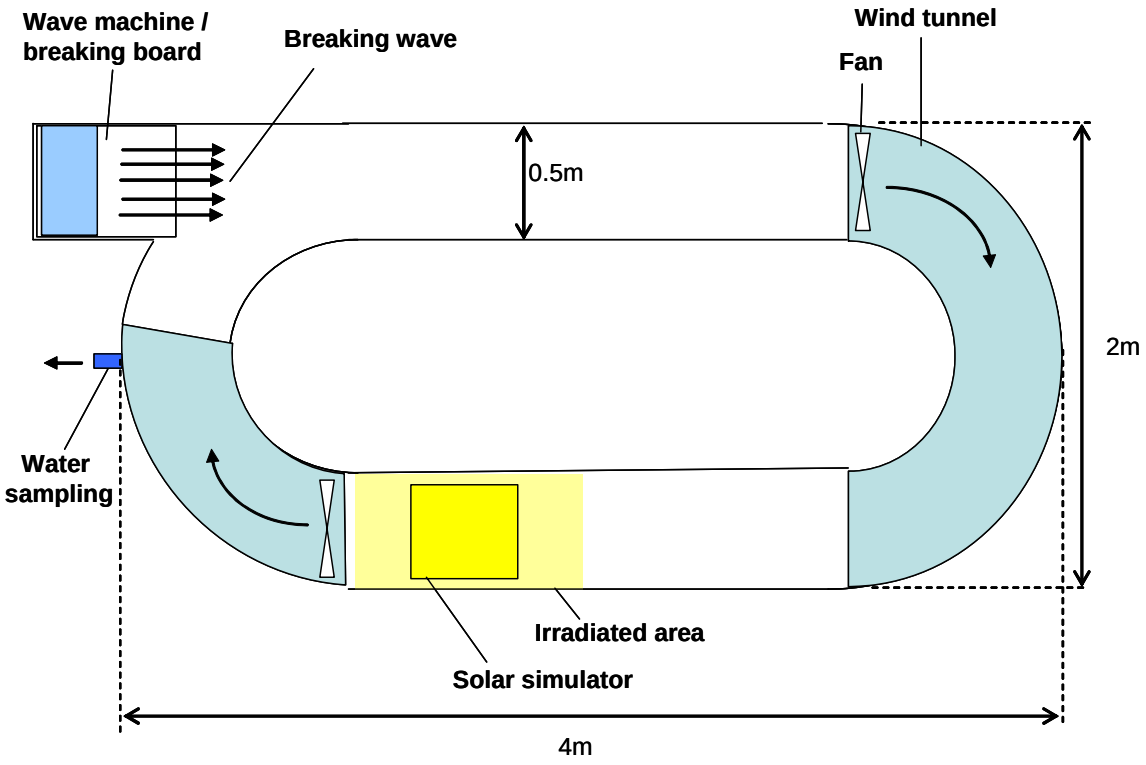

Figure 3.16 Schematic drawing of the meso-scale flume.

3.3.3 Solar simulation in the meso-scale flume

Natural sunlight was simulated with a solar simulator from Gmbh Steuernagel. The 4KW lamp emits a wavelength spectrum calibrated to fit natural sunlight at high noon and in the absence of skies. Figure 3.17 shows the measured spectrum from the solar simulator compared to one of the most widely used standard spectra for solar irradiance (CIE publication 85, 1989).

The exact exposure of the oil in the meso scale flume is uncertain, as the oil is moving it will only be within the irradiated area periodically. The exposure will be highly dependent on the distribution of the oil in the meso scale flume and the thickness of the emulsion on the surface. An estimated

irradiation pr day is compared with the average irradiation pr day for some Norwegian cities in Figure 3.18.

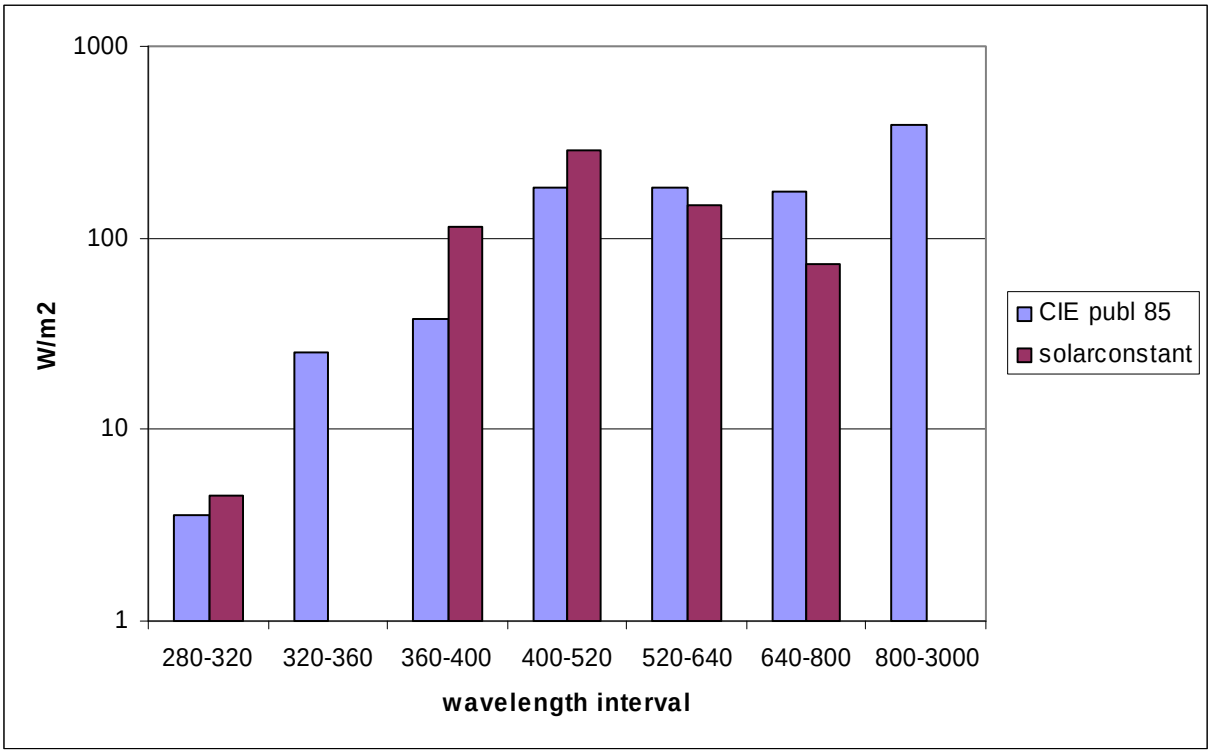

Figure 3.17Measured wavelength spectrum compared to standard spectrum suggested in CIE publication 85

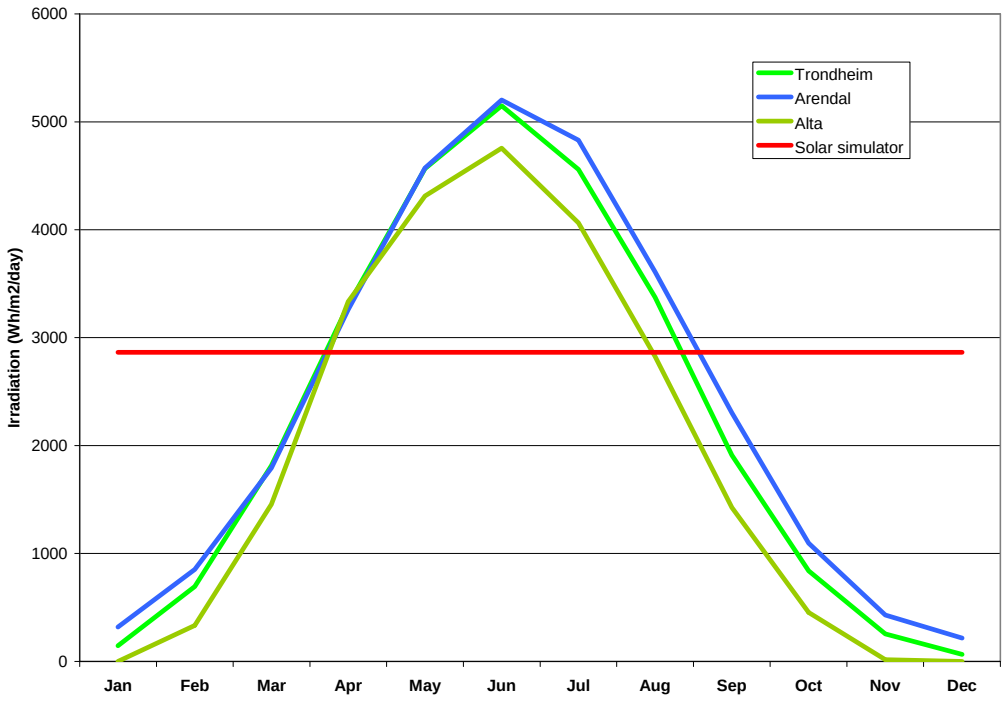

Figure 3.18Daily Irradiation for some Norwegian cities through the year compared with the estimated daily irradiation in the meso scale flume.

The simulated irradiance seems to be approximately average for the daily irradiance throughout the year.

3.3.4 Sampling and analysis of surface oil

An oil sample (typically 9 L) was carefully released on the water surface. Surface oil/emulsion and water samples were taken frequently in the first hours of the experiment and at increasing intervals as changes in oil properties slowed down at long weathering times. Sampling and analyses performed are described below.

Samples of the surface oil/emulsion were taken with an aluminum tray and transferred to a 0.5 L separating funnel. After settling for 10 minutes in the climate room, free water was drained off.

Physical properties determined for all emulsion samples during the experiment were:
- viscosity
- water content
- evaporative loss
- density

Analyses performed for a limited number of samples were
- Oil concentration in the water column
- Yield stress determination
- Chemical characterisation (SARA analysis)
- FT-IR (Fourier Transform IR-spectroscopy)
- GC-FID (Gas chromatography coupled with Flame Ionisation Detector)

The planned sampling schedule is given in Figure 3.19. The plan was followed in the early stages of the experiments. As sampling intervals increased to several days, sampling have been adjusted to fit working hours. Some experiments have also been ended earlier than 14 days.

Sample number	Sampling time	Fraction evaporated	Density (oil/emulsion)	Water content	Viscosity	Yield stress	Over-washing experiments
1	1 h	*v*	*v*	*v*	*v*	*v*	*v*
2	3 h	*v*	*v*	*v*	*v*		
3	6 h	*v*	*v*	*v*	*v*	*v*	*v*
4	12 h	*v*	*v*	*v*	*v*		
5	24 h	*v*	*v*	*v*	*v*	*v*	*v*
6	2 days	*v*	*v*	*v*	*v*		
7	3 days	*v*	*v*	*v*	*v*	*v*	*v*
8	4 days	*v*	*v*	*v*	*v*		
9	6 days	*v*	*v*	*v*	*v*	*v*	*v*
10	8 days	*v*	*v*	*v*	*v*		
11	10 days	*v*	*v*	*v*	*v*	*v*	*v*
12	12 days	*v*	*v*	*v*	*v*		
13	14 days	*v*	*v*	*v*	*v*	*v*	*v*

Figure 3.19 Sampling schedule for weathering and droplet size distributions

Methods for each analysis are described below.

Rheological measurements (Viscosity and Yield stress determination)

Viscosity and yield stress were measured as soon after sampling as possible, to avoid effects of instability of the emulsions. Rheological measurements were performed with a Physica MCR300 rheometer. Stress-sweeps and viscosity measurements were perfomred. Viscosity was measured according to the standard methodology described in McDonagh *et.al*, 1995.

Experimental setup for viscosity measurements:

Measurement system	:	PP50
Gap	:	1mm
Shear rate	:	$1s^{-1}$, $5s^{-1}$, $10s^{-1}$, $50s^{-1}$,$100s^{-1}$,$200s^{-1}$,$500s^{-1}$, and $1000s^{-1}$

All viscosities are reported at $10s^{-1}$.

Experimental setup for stress-sweeps.:

Measurement system	:	PP50
Gap	:	1mm
Angular velocity	:	10 rad/s
Stress interval	:	0.05-1000 Pa (logarithmic increase)

Yield stress is calculated automatically by the analysis module of the US200 Software based on the stress sweep measurement.

Water Content and stability

The amount of water within the emulsion is determined by adding approximately 2000ppm emulsion breaker to the sample and heating in a vial. As the emulsion is broken the height of the water-oil interface and height of the total sample are measured in the vial. The relative amount of water compared to the total sample volume is calculated.

Density

Density was measured according to ASTM method D 4052-91 at an Anton Paar DMA 4500 densitometer. The density was measured on the water free sample. The water was removed as described above under the methodology for determination of water content.

Evaporative loss

As the light end components of the oil evaporate the density increases. The density of the oil was linearly dependent on the wt% evaporative loss. As the density of the water free residue was known (method described above) the evaporative loss could be calculated.

SARA Analysis

Samples were analyzed on Iatroscan thin layer chromatograph. The method separates the oil into four component groups and gives a semi quantitative measure of the relative content of: Saturates Aromatics, Resins and Asphaltenes (SARA).

FT-IR

The FT-IR measures the oils absorption of wavelengths in the IR spectrum. The analysis yields information about the relative amount of functional groups of the components of the sample.

GC-FID

The method is a gas chromatographic method separating chemical components in the sample by boiling point and polarity.

3.3.5 Collection of water samples

Water samples were taken at 80 cm depth through a tap in the basin wall, into a Pyrex glass bottle (1 L). The water sampled was acidified with some droplets of 10% HCl (pH lower than 2). The sampling position is shown in Figure 3.16. Samples were extracted by liquid-liquid extraction with dichloromethane and quantified by spectro-photometry.

3.4 Plunging jet experiments

Plunging jet experiments were conducted at specific time intervals during the regular oil weathering tests, the first about one hour after test initiation. The wave generator in the weathering flume was shut down some minutes prior to the experiments to allow resurfacing of dispersed oil droplets, and the oil was confined behind a barrier inserted downstream of the test section to obtain a homogeneous oil slick below the plunging water jet (Figure 3.20).

All experiments were conducted with the plunging jet apparatus described previously in conjunction with the initial calibration experiments (Section 3.2). The experimental conditions were varied from one test to the next, partly with the aim of obtaining a picture of the droplet cloud with sufficient quality for the subsequent digital image processing. The experimental variables are described in Table 3.2. The flume tests were conducted at two different water temperatures (5 and 13 ^{o}C). Most tests were conducted with artificial sunlight, but a few tests were made without solar exposure. Tests without solar exposure are marked “no sun”, while tests exposed to sun are marked “w/ sun”.

The film thickness of the confined oil layer differed from one experiment to the next since water-in-oil emulsions with densities approaching the density of sea water tend to form thicker oil layers than more buoyant water-free oil. The free fall height had to be increased from time to time to compensate for the increasing resistance to break-up of the oil film caused by increased viscosity and film thickness.

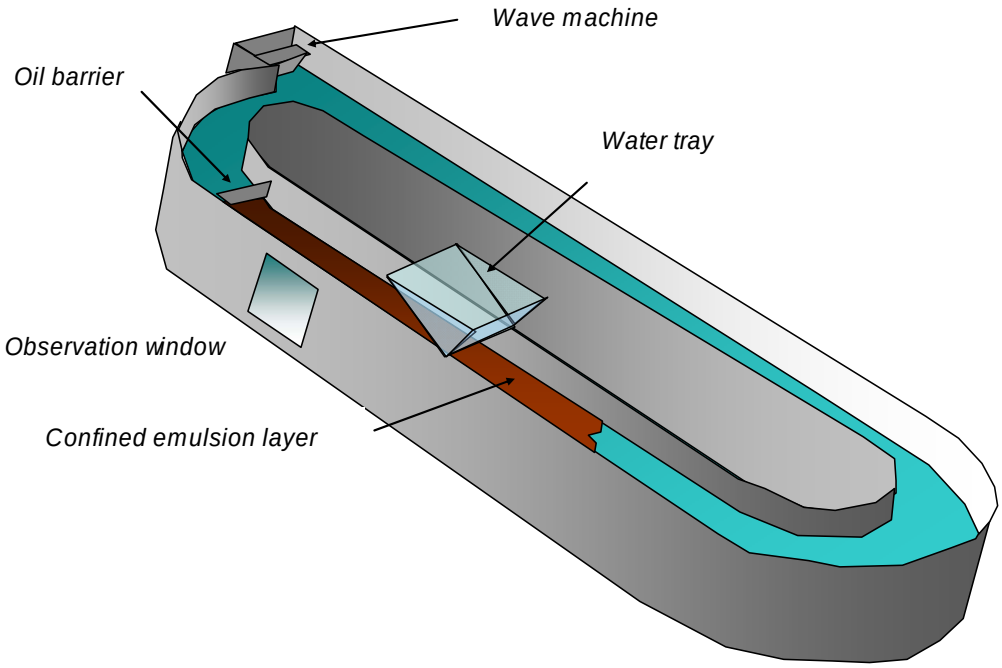

Figure 3.20. Schematic drawing of experimental setup for the droplet break-up experiments in the weathering flume. The wave machine was stopped prior to the experiments and the oil was confined against a barrier to form a homogeneous layer beneath the plunging water jet.

Table 3.2. Overview of experimental variables

Variable	unit	Comment
Time from start of flume test	hours	
Free fall height	cm	Adjusted from one experiment to the next
Emulsion film thickness	mm	Caused by confinement against a barrier
Emulsion viscosity	mPas	Measured just prior to the experiment
Emulsion density	g/cm^3	Measured just prior to the experiment
Surface tension	mN/m	Measured on water free oil

4.0 Results

4.1 Wave tank calibration experiments

This section presents a calibration study of oil droplet breakup experiments with plunging jets and breaking waves. The plunging jet test has been developed for use in oil droplet breakup tests to be performed in situ during long term weathering studies in SINTEF's weathering flume. The object of the present study has been to establish a relationship between oil droplet breakup in these tests and in breaking wave tests.

Calibration of the plunging jet to the breaking wave was carried out with moderately weathered Troll crude oil (150^{o}C+) to avoid unwanted changes in the oil properties due to evaporation during the experiments. One set of experiments was made with water-free oil, while another set was made with a 50 % water-in-oil emulsion made up of the same oil. In all experiments, the water surface of the straight flume was covered with a 2 mm thick layer of oil or emulsion.

The wave generator was adjusted to produce two subsequent waves with a frequency of 65 cycles per second and 10 cm amplitude. With this setup, the first wave passed without breaking, while the second wave formed a spilling breaker in front of the observation window. Data from a Nortek Vectrino acoustic current meter with a sampling frequency of 25Hz mounted downstream of the point of breaking reflected an orbital motion with a characteristic spin up and decay period (Figure 4.1).

In order to determine the correspondence between the given wave amplitude and the free fall height in the plunging jet experiments, the water tray was mounted at different heights above the surface of the flume. In the experiments with water free Troll crude, two free fall heights were tested, 5 cm and 15 cm, while in the experiments with a 50 % water-in-oil emulsion, three heights were tested: 5 cm, 15 cm and 23 cm.

The droplet size distribution parameters determined in the various experiments are summarized in Table 4.1 and Table 4.2, while the observed distributions are shown in Figure 4.2 and Figure 4.3.

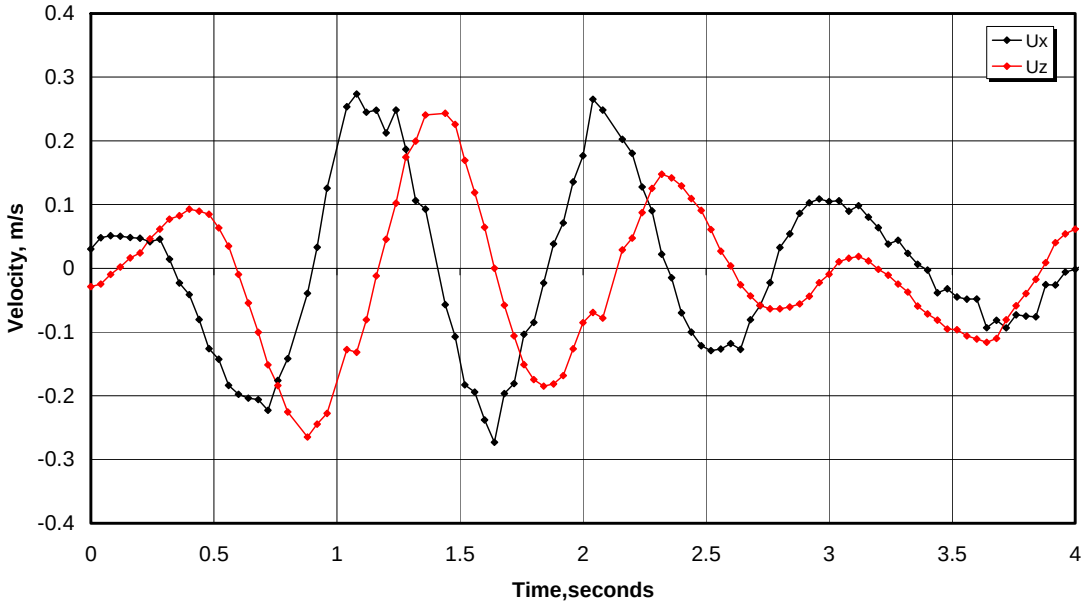

Figure 4.1. Time series of currents measured during a breaking wave experiment. The currents are measured 20 cm below water level 1 m downstream of the point of breaking. U_x is the axial component of the current, while U_z is the vertical.

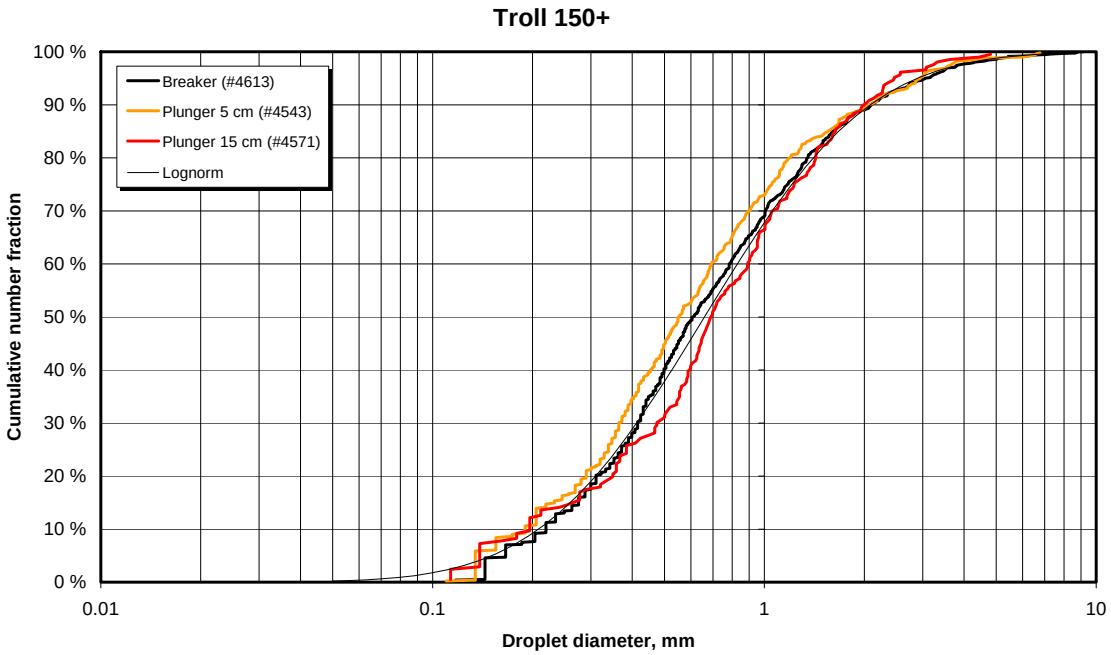

Figure 4.2. Plot of droplet size distributions obtained in the Troll 150°C+ experiments.

Table 4.1. Results for Troll 150°C+, water free

	Median diameter, mm	Standard deviation, log
Breaking wave 10 cm amplitude	0.66	0.37
Plunger 5 cm	0.60	0.38
Plunger 15 cm	0.68	0.37

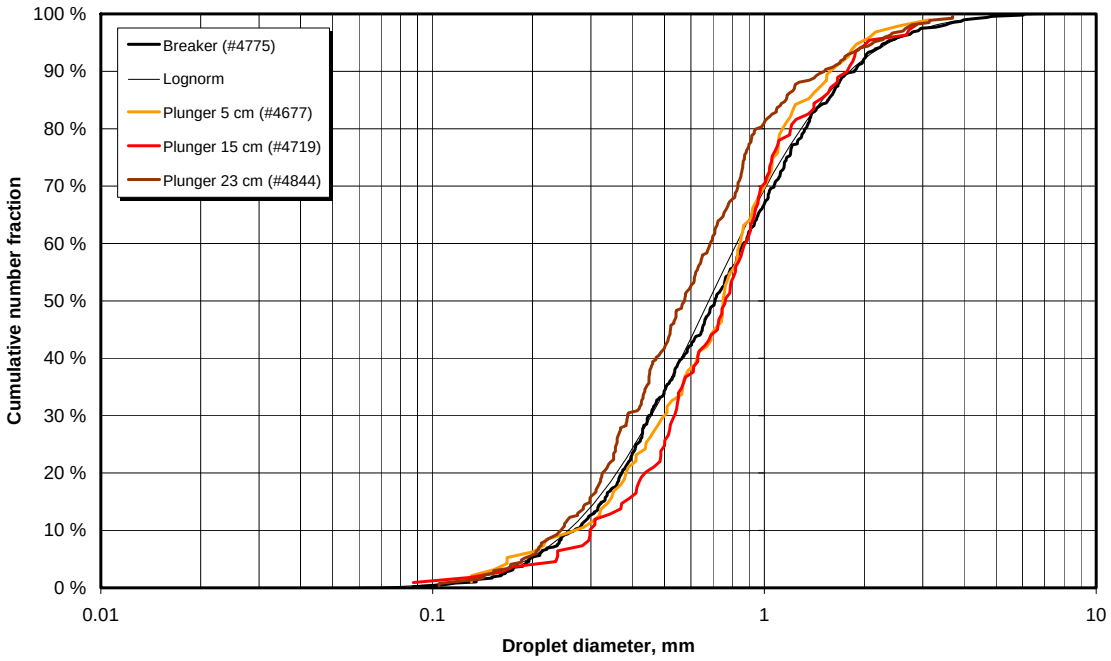

Figure 4.3. Log-normal plot of the droplet size distributions obtained in the experiments with 50% water-in-oil emulsion of Troll 150°C+ oil.

Table 4.2. Troll 150°C+, 50 % water content

	Median diameter, mm	Standard deviation, log
Breaking wave 10 cm amplitude	0.70	0.33
Plunger 5 cm	0.68	0.29
Plunger 15 cm	0.73	0.29
Plunger 23 cm	0.58	0.31

The resulting median droplet sizes are compared in Figure 4.4. In general, the experiments demonstrated that the plunging jet tests will generate droplet size distributions with the same character as obtained in the breaking wave tests – i.e. in both types of test, the droplet size distributions resembled log-normal distributions. In the experiments with water-free Troll crude, the droplet size distributions from both plunging jet tests (5 and 15 cm free fall heights) showed close agreement with the droplet size distributions obtained from the breaking wave test – both in terms of logarithmic mean values and standard deviations (Table 4.1). This was also the case for 5 and 15 cm free fall heights in the experiments with 50 % water-in-oil emulsion. However, the results from the test with 23 cm free fall height indicated a shift towards smaller droplets, with a logarithmic mean diameter of 0.58 mm compared with 0.70 mm in the breaking wave test (Table 4.2).

Taking into account the experimental uncertainties, we conclude that droplet breakup experiments with plunging jets with 10 cm free fall height will produce droplet size distributions corresponding closely to those produced by breaking waves with about 10 cm amplitude.

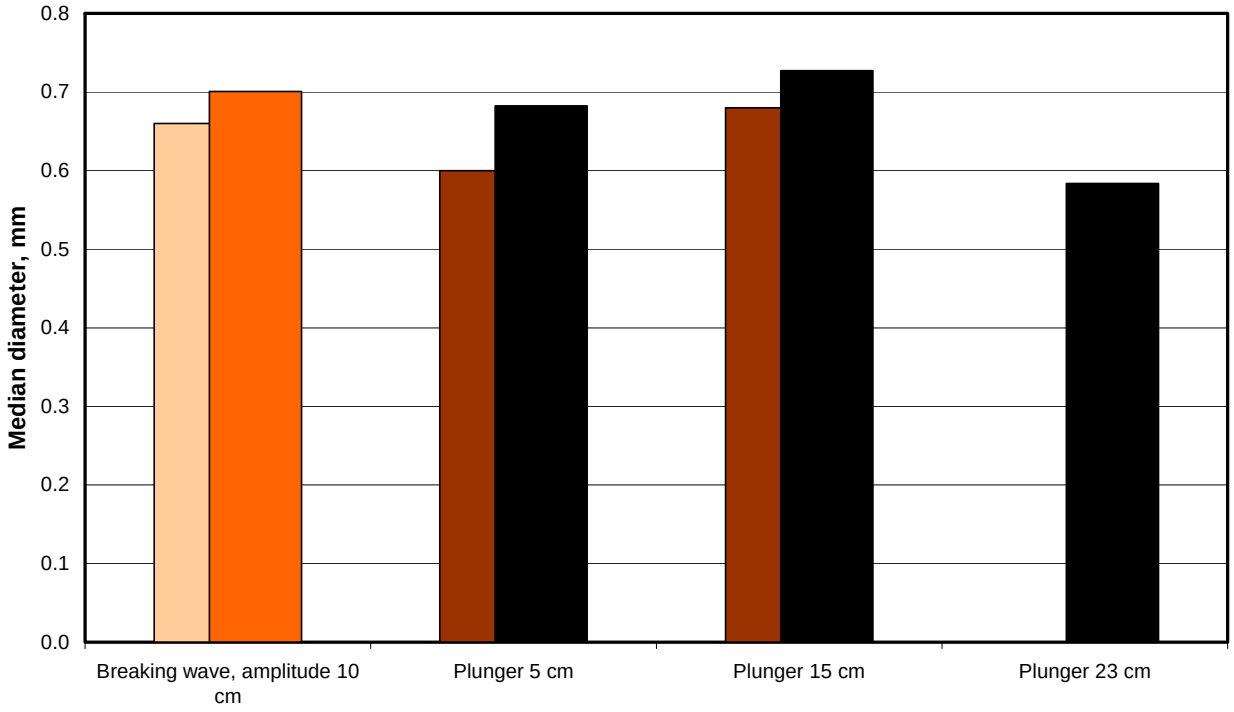

Figure 4.4. Comparison of median droplet sizes observed in the calibration experiments. Results from the water-free oil (lighter colors) are shown behind the results from the 50 % water in oil emulsion (darker colors)

In summary, two series of tests were made with moderately weathered Troll crude (150°C+), one series with water-free oil, and one with a 50 % water-in-oil emulsion. The results were evaluated by comparing the oil droplet distributions obtained in the two tests.

These distributions were found to fit closely to a log-normal number distribution, characterized by the median diameter d_{50} and a logarithmic standard deviation s. The former parameter is estimated by averaging the logarithm of the measured droplet diameters;

$$\log d_{50} = \frac{1}{n} \sum_{i=1,n} \log d_i \ ,$$

while the latter is determined as the standard deviation of the same set of logarithmic values.

The tests indicated that a plunging jet test with 10 cm free fall height will produce distribution parameters close to the one obtained from tests with a 10 cm amplitude breaking wave. A greater free fall height tended to produce a reduction in the logarithmic mean droplet size with the same standard deviation.

4.2 Weathering flume experiments

When a crude oil is spilt at sea a number of natural processes occur, changing the volume and the chemical properties of the oil. The relative contribution of each process varies during the duration of the spill, as illustrated schematically in Figure 4.5.

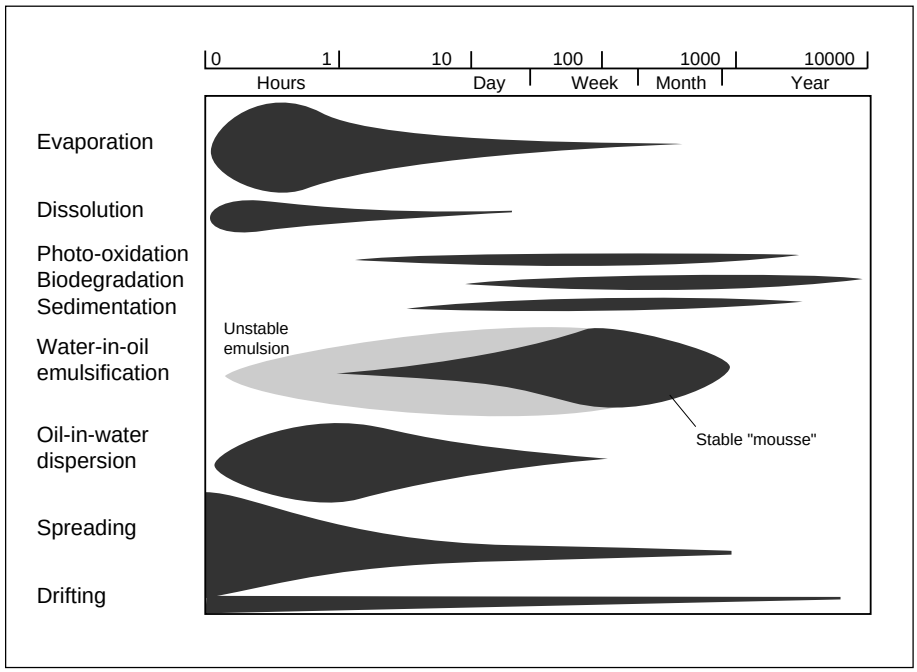

Figure 4.5 Relative importance of weathering processes with time.

Artificial weathering in the meso-scale flume enables studies of some of these processes:

- Evaporation
- Emulsion properties (water content, emulsion viscosity)
- Photo oxidation
- Entrainment, submerging

Evaporation and emulsification are processes that have been thoroughly studied earlier both in the field and in the laboratory. Based on such studies, numerical models have been developed for prediction of oil properties on the sea surface (e.g the SINTEF Oil Weathering Model, OWM, Johansen *et.al.* 1991). Existing algorithms have been validated against field data, but only for a limited weathering time.

In this section the measured evaporation and emulsification is studied to see whether the observed development in properties deviate from observations in shorter term studies. The Troll and Norne crudes are currently in the SINTEF OWM database, and weathering properties can be predicted. For these oils measured data is compared with predicted values.

Limited tests are performed on settling velocity of lumps formed in the flume to investigate the potential for submerging of a slick broken into lumps.

4.2.1 Evaporative loss

The evaporative loss is calculated for all samples based on the density of the water-free residues. Evaporative loss needs to be accounted for as part of the mass balance. Along with emulsification, evaporative loss is also one of the major contributors to change in physical properties of the oil on the sea surface.

Evaporative loss in the Norne and Troll experiments are compared with predicted data from the SINTEF OWM in Appendix A: Laboratory Results (Figure 10.6 and Figure 10.7 respectively). As an

example measured evaporative loss for the experiments with Troll at 5°C are compared with predictions from the SINTEF OWM in Figure 4.6. Predicted values for wind speeds at 10-15 m/s coincide with measured evaporative loss from the flume experiments.

The evaporative loss is dependent on the amount of light end components in the oil, and will vary among the oils in the flume experiments. Weathering data for all experiments are shown in Figure 4.7. As an example the light North Slope crude lost 50% of the initial volume while the IFO380 only lost 2.5% to evaporation after two weeks of weathering.

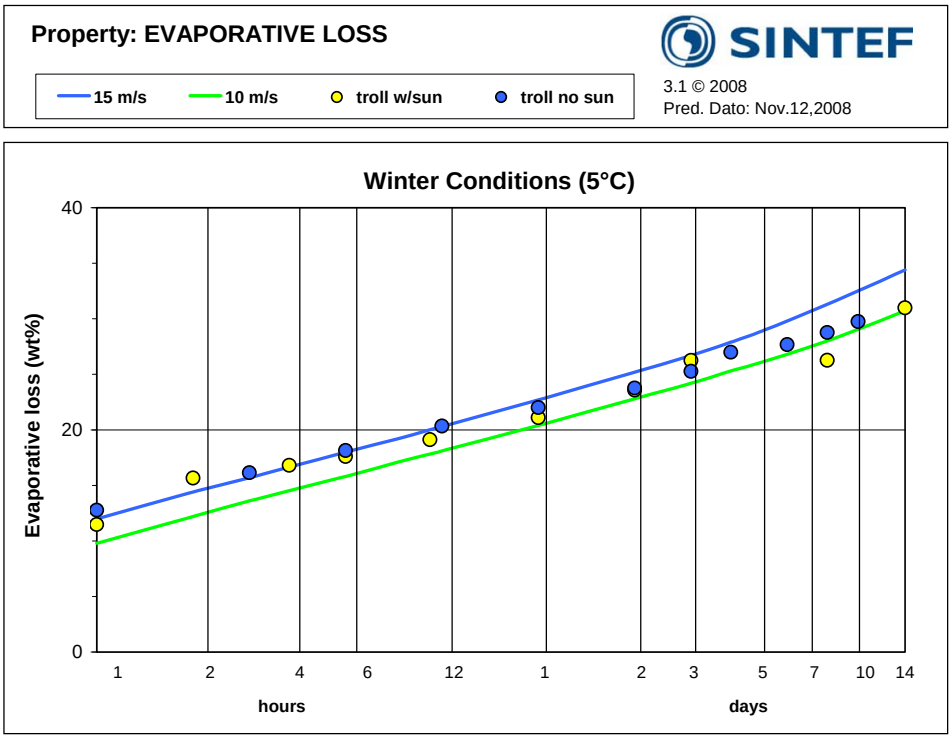

Figure 4.6 Evaporative loss in the experiments with Troll with and without sunlight. Experimental results are compared with predictions from the SINTEF OWM.

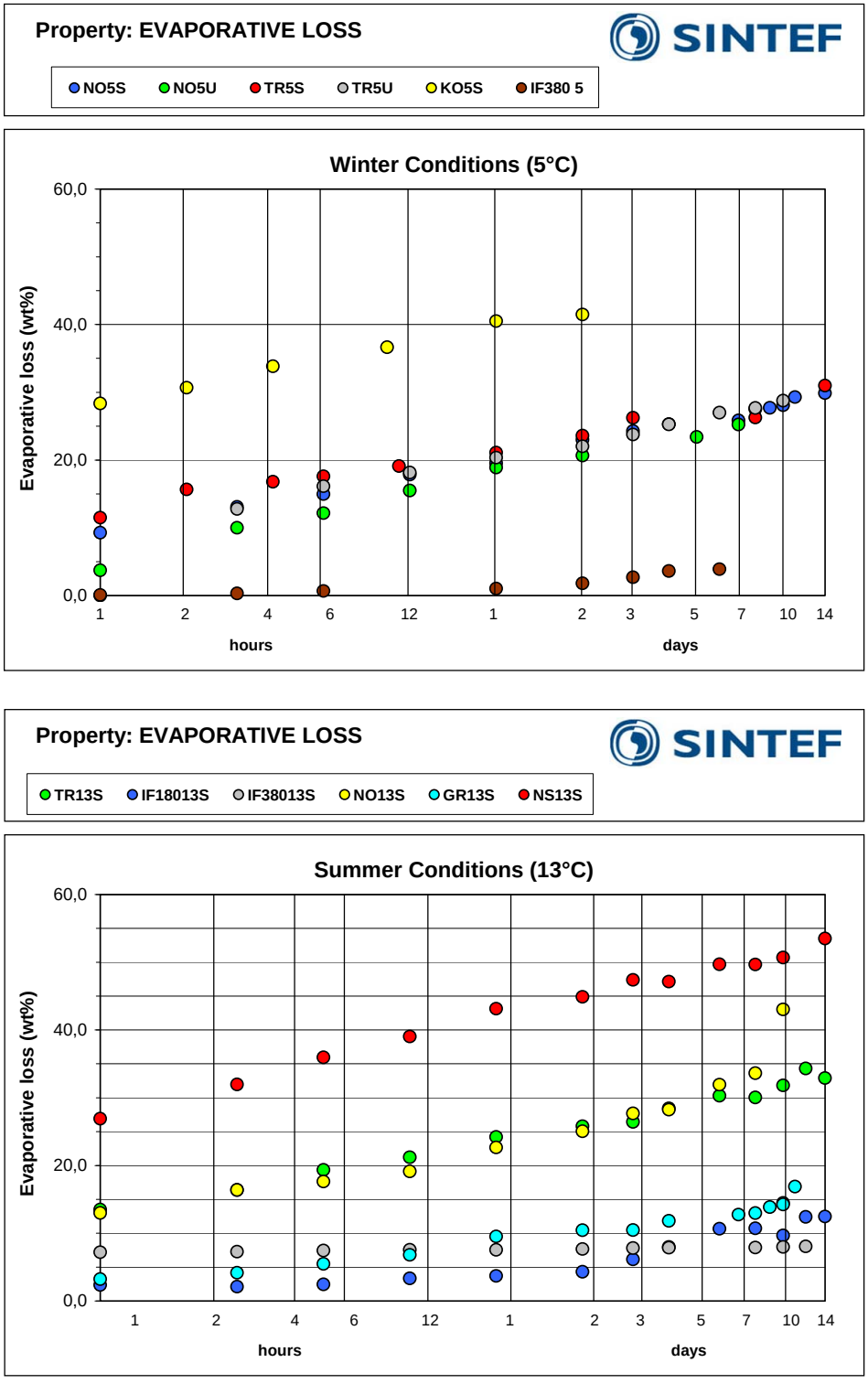

Figure 4.7 Measured evaporative loss for all experiments (5°C above, 13°C below)

NO-Norne, TR-Troll, KO-Kobbe, GR-Grane, NS-North Slope
Numbers indicate temperature, S-Solar simulator, U-No Sunlight

4.2.2 Emulsion properties

4.2.2.1 Water content

When oil emulsifies, the viscosity generally increases. Increased water content also increases the volume of the emulsion on the sea surface. As an example an emulsion with 80% water content has a volume 5 times greater than the oil alone. Water contents for all experiments are shown in Appendix A: Laboratory Results (Figure 10.2). The maximum water content of the emulsions varies from 53% for the IF380 at 5°C to in excess of 80% for emulsions of the Norne crude. The maximum water content of the emulsions correlates negatively with the viscosity of the emulsion (i.e. higher viscosity oils take up less water, Figure 4.8). This is consistent with observations from earlier field and laboratory studies.

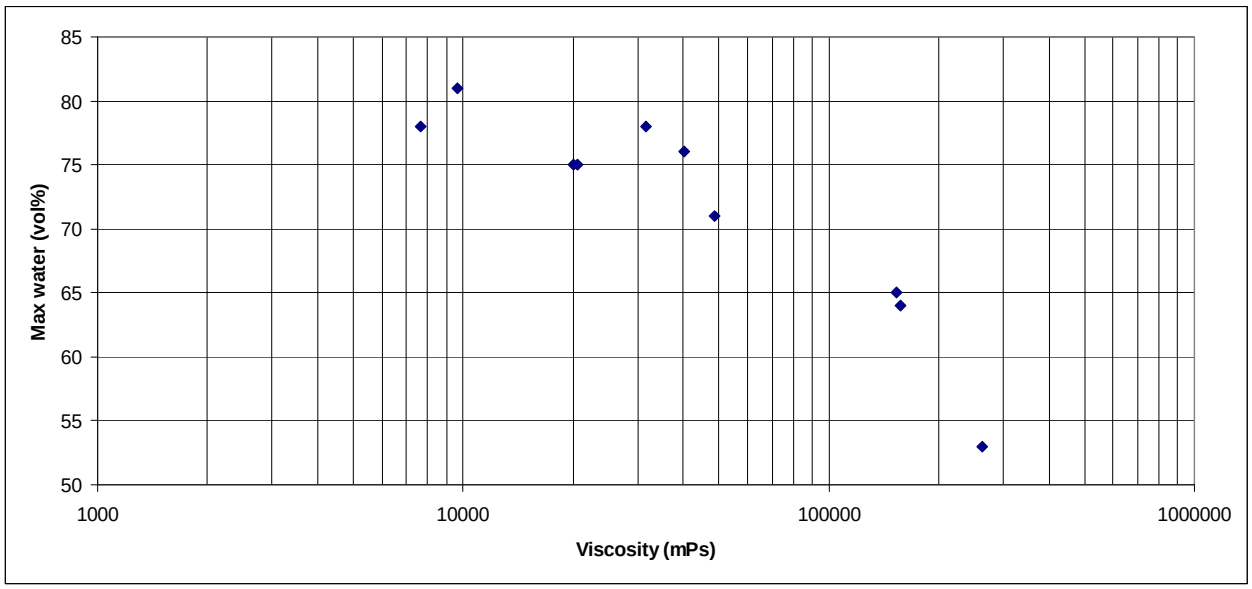

Figure 4.8 Maximum water content in the experiments plotted against maximum viscosity for the emulsions formed.

The trends in the emulsification kinetics for these longer term weathering experiments were consistent with earlier shorter-term studies.

Predicted water uptake from the SINTEF OWM is compared with water uptake in the experiments with Troll at 5°C in Figure 4.9. Both the maximum water uptake and the emulsification rate are comparable with the predicted values. Predicted water uptake for the Norne experiments followed the observed kinetics reasonably well, but the predicted water uptake was somewhat less than the experimental data.

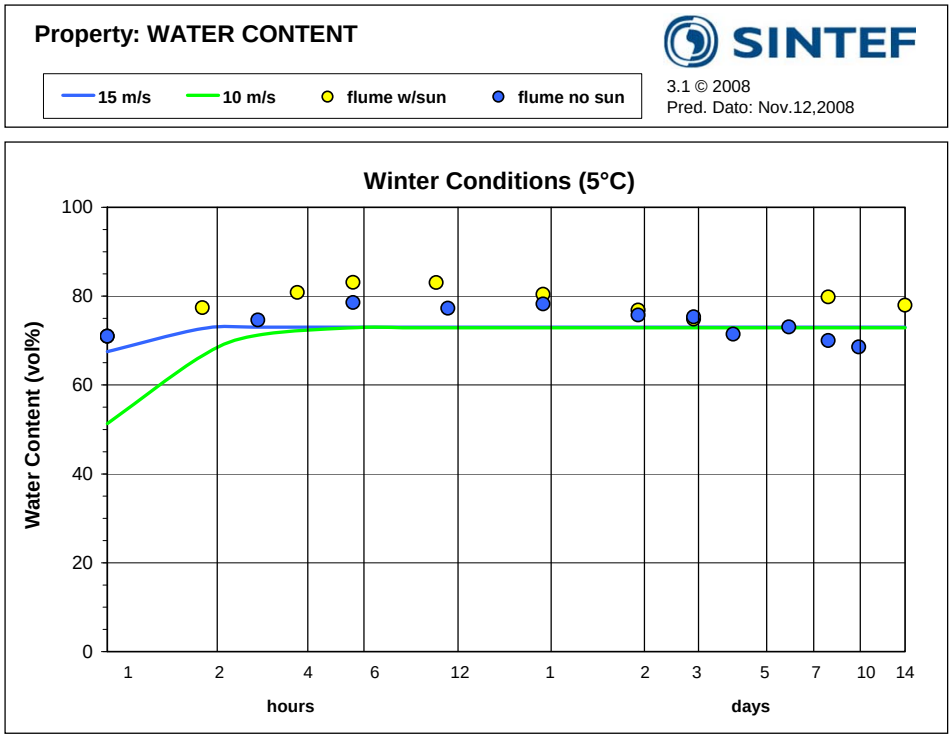

Figure 4.9 Water content in the experiments with Troll with and without sunlight. Experimental results are compared with predictions from the SINTEF OWM.

4.2.2.2 Emulsion viscosity

Emulsion viscosity is important to the expected lifetime of weathered oil on the sea surface. A high viscosity limits the spreading and natural dispersion of a drifting slick, thus extending the lifetime of the slick. The viscosity is also a critical parameter for oil spill response planning and execution, affecting both dispersibility and effectiveness of alternative mechanical recovery equipment options.

Measured emulsion viscosities for all the experiments are shown in Figure 4.10. The tested oils have a large variation in viscosity in the early stages of weathering. Towards the end of the experiments the crude oil viscosities seem to converge between 20,000 mPas and 50,000 mPas. The bunker fuel oils tend to achieve a higher viscosity over the two-week experimental period.

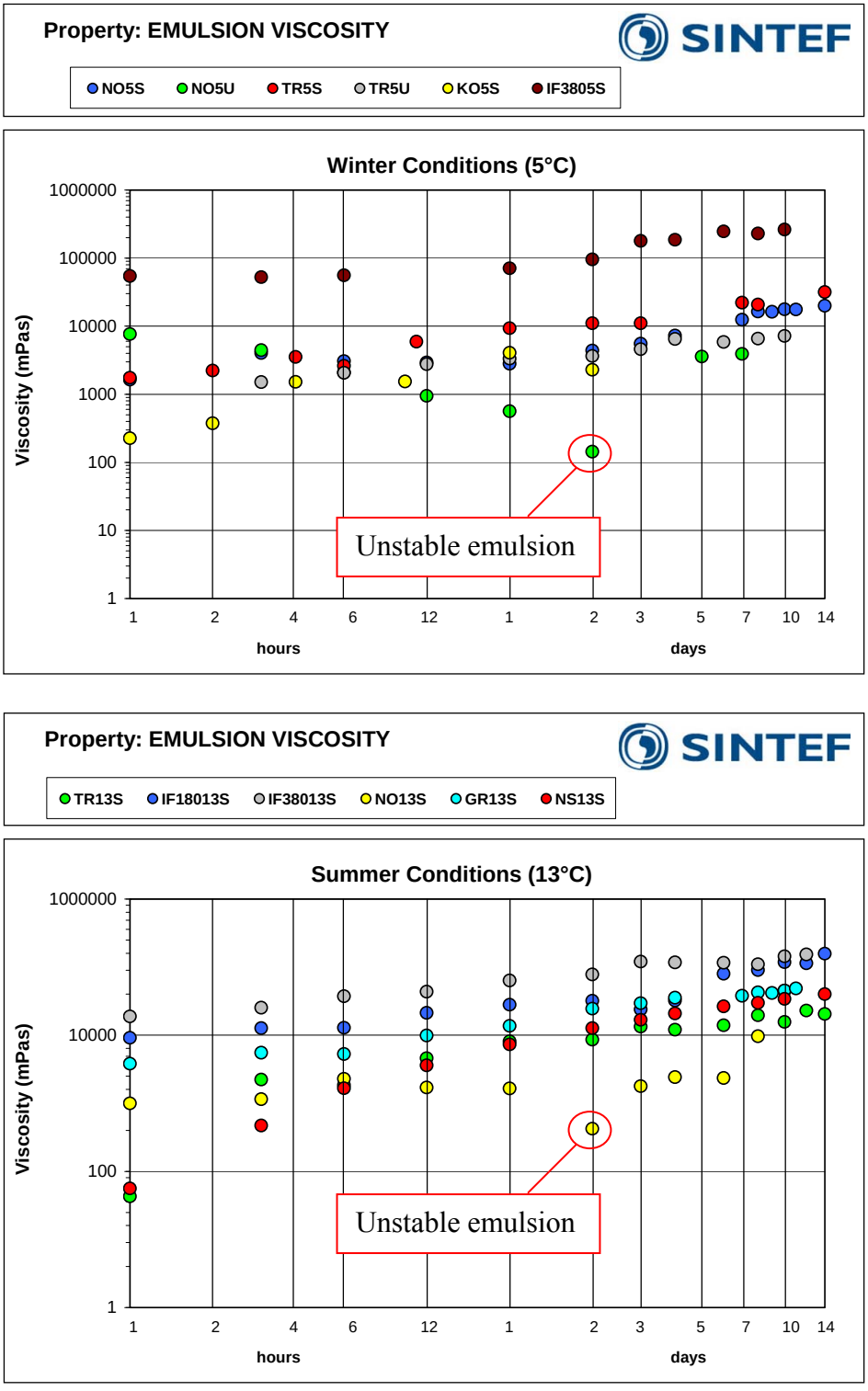

Figure 4.10 Measured emulsion viscosity for all experiments (5°C above, 13°C below). Viscosity is reported at shear rate $10s^{-1}$.

NO-Norne, TR-Troll, KO-Kobbe, GR-Grane, NS-North Slope
Numbers indicate temperature, S-Solar simulator, U-No Sunlight

The evolution of the emulsion viscosity compared to predicted viscosity from the SINTEF OWM is shown in *Figure 4.11* for the Troll oil (winter conditions), and in *Figure 4.12* for the waxy Norne oil.

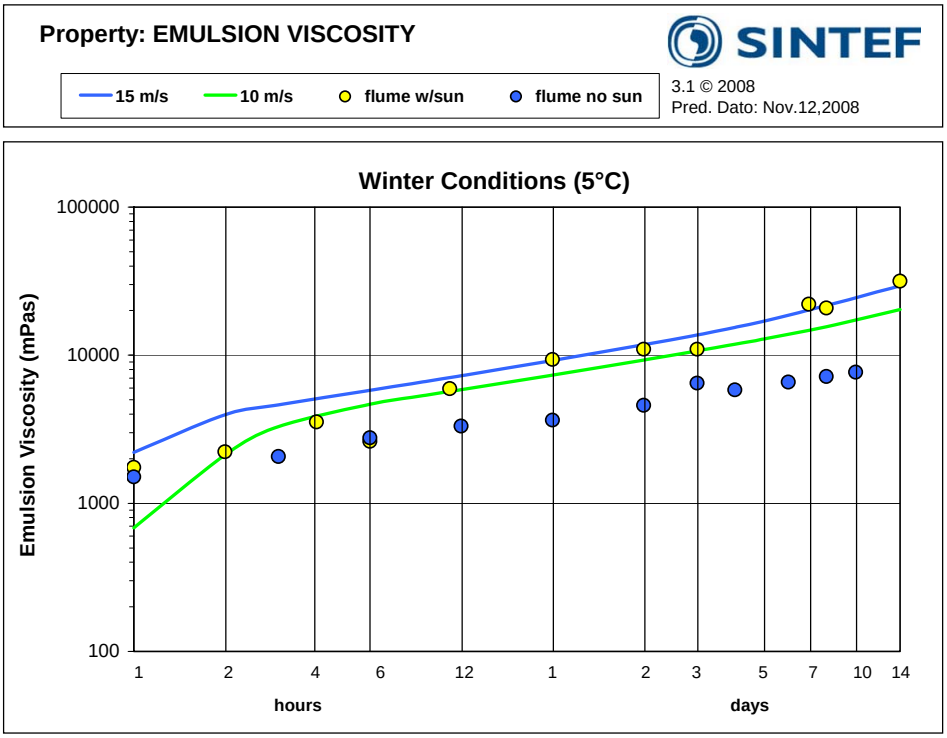

Figure 4.11 Predicted emulsion viscosity for the Troll crude from the SINTEF OWM compared with flume experiments at 5° with and without sunlight.

Emulsion viscosity for the Troll experiment with sunlight is comparable to predicted values at 10-15 m/s wind speed. The experiment without sunlight does not correspond as well to predicted data.

Overall, the emulsion viscosities of the oils tested follow trends consistent with experience in field and laboratory studies on shorter time intervals. The Norne oil exhibits the known tendency of waxy crudes to transition through a low-viscosity phase during the first 24 – 48 hours at sea (Figure 4.12). This behavior can be understood by considering that the viscosity of a waxy oil is in part dependent on the cohesive forces within the wax matrix. As more and more water is emulsified into the oil, the separation between adjacent wax particles increases, and resistance to flow (viscosity) decreases. Under photo-oxidation the emulsion becomes more stable after about 48 hours, and begins to increase in viscosity. This aberrant behavior of waxy crudes makes them potential exceptions to a “normal” oil entrainment algorithm. The prediction curves in Figure 4.12 are based on a sample of the Norne oil from 1998, with 13% wax content, as compared to 4.3% for the Norne oil sample from 200, explaining the lack of agreement between the two.

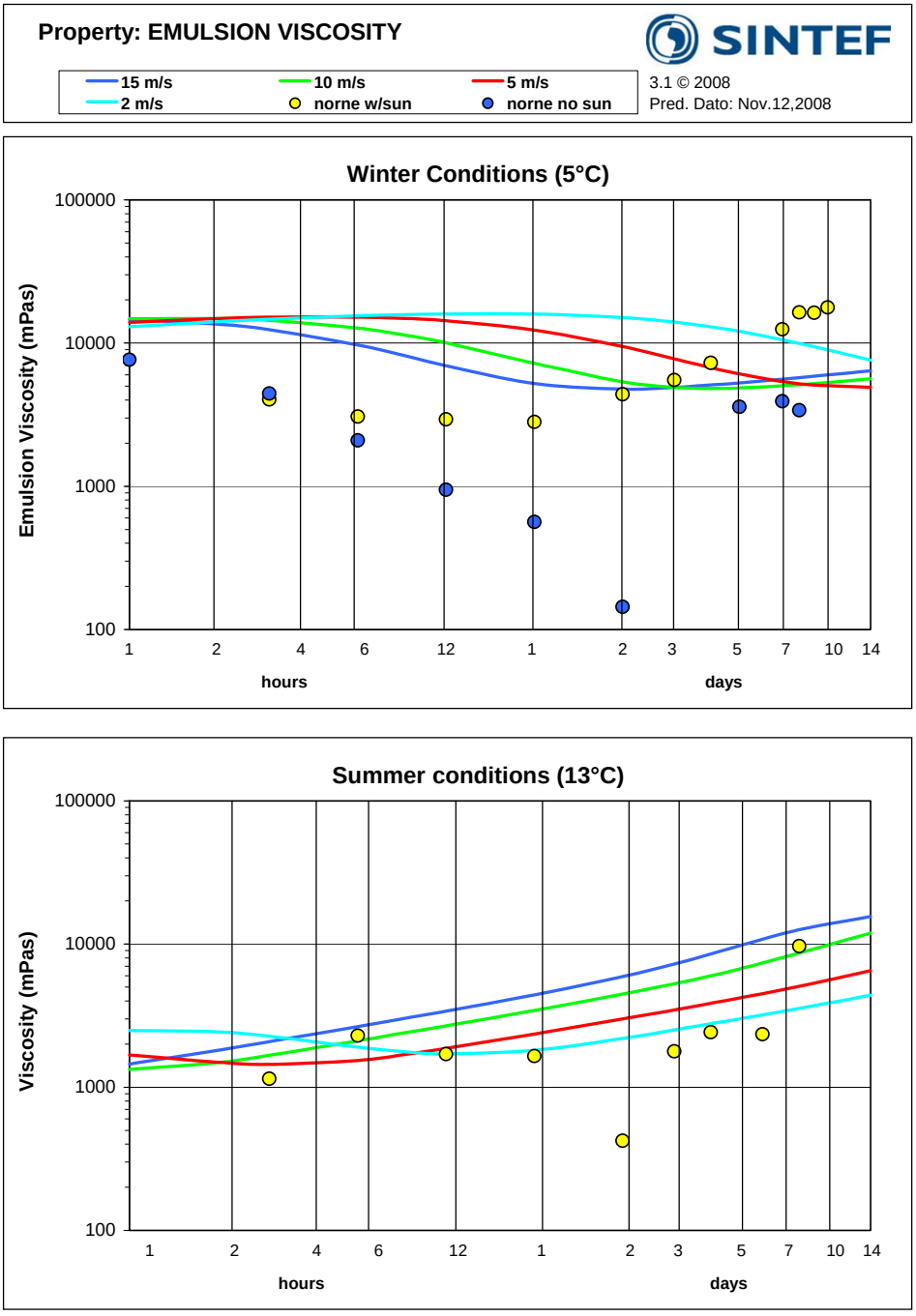

Figure 4.12 Measured emulsion viscosity for the Norne experiments compared to predictions from the SINTEF OWM. Viscosities are reported at shear rate $10s^{-1}$. The observed behavior of the viscosity is typical for waxy crude oils. The prediction curves are based on a sample of the Norne oil from 1998, with 13% wax content, as compared to 4.3% for the Norne oil sample from 2008, explaining the lack of agreement between the two.

4.2.3 Photo-oxidation

To study the effects of photo-oxidation, experiments with Troll and Norne were performed with and without artificial sunlight. The solar simulator is described in Section 3.3.3.

In the experiments with Norne, significant amounts of wax were deposited on the walls of the test tank. The removal of wax from the oil changed the physical properties of the oil. It is impossible to distinguish changes in physical properties due to wax depletion versus effects of photo oxidation. The Norne experiments are therefore not discussed further here.

In the experiments with Troll crude with and without solar simulation there is a significant difference in the viscosity of the emulsions formed (Figure 4.13.). The difference in viscosity is apparent after a few hours of weathering. After 12 hours and throughout the remainder of the experiment the viscosity is 2-3 times higher with solar simulation, compared to the experiment without sunlight.

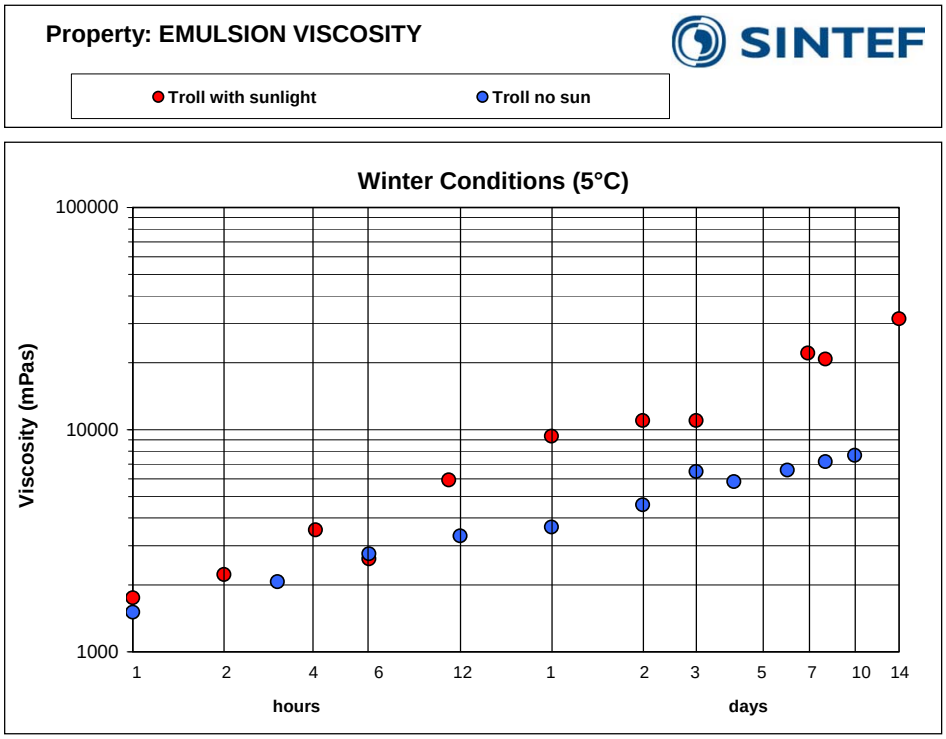

Figure 4.13 Emulsion viscosity for the experiments with Troll at 5°C with and without solar simulation. Viscosity is reported at a shear rate of $10s^{-1}$

If there is no change in the chemical characterization of the oil, or presence of surface active chemicals, the emulsion viscosity is usually governed by water content and evaporative loss. To conclude that the difference in emulsion viscosity is due to photo-oxidation, any contribution from differences in evaporative loss and water content need to be ruled out. Figure 4.6 shows that the evaporative loss with time for the two Troll experiments is comparable, and differences in the viscosity are not likely to arise from differences in evaporative loss. (Similarities in evaporation in the two experiments are also confirmed by comparison of the gas chromatograph- flame ionization detector (GC-FID) figures shown in Section 10.3)

The water content is generally higher for the samples from the experiments with sunlight. This may contribute to the higher viscosity. The samples taken after 2 and 3 days, however, have identical water content and still significantly differing viscosities. This means the increase in viscosity with sunlight exposure is not solely because of the higher water content. It should also be noted that the higher water content may be due to changes in the oil chemistry caused by the sunlight.

To investigate any changes in the bulk properties of the parent oil, viscosity was measured for some of the water-free residues of the samples. Results are given in the table below.

Table 4.3Physical properties for two samples from each of the Troll experiments at 5°C (including viscosity of the water-free residue).

	Sample	Days	Viscosity Residue (mPas)	Viscosity Emulsion (mPas)	Watercontent (vol%)	Evaporative loss (wt%)
With sun	P11	8	4300	20800	80	28.3
	P12	14	5430	31600	71	33.5
No sun	P10	8	3490	7180	70	28.8
	P11	10	3040	7670	67	29.7

The viscosity of the parent oil is higher in the experiment with solar exposure compared to the experiment without sunlight. This indicates whatever changes have occurred in the oil significantly change the bulk properties of the oil itself.

To try finding causes for the changes in physical properties of the oil some chemical analyses were performed on a selection of samples from the Norne and Troll experiments. The analysis performed were SARA analysis with Iatroscan and FT-IR. The SARA analysis is a chromatographic method giving a coarse separation of chemical compounds based on polarity. In earlier studies the method has proven efficient in showing formation of polar components in oils when subject to solar exposure. This could not be shown in this study.

The FT-IR is also a coarse method giving an image of the relative content of functional groups in the oil. A possible effect of photo-oxidation would for example be a decrease in aromate rings and formation of oxidation products showing an increase in acid, ketone and aldehyde groups. No such effects could be shown in this study.

The results from the chemical analysis are reported in Section 10.3, but are not further discussed.

4.2.4 Submerging

Observations from actual spills suggest that highly weathered oils can submerge, at least temporarily, below the sea surface. Submersion time is expected to be determined primarily by oil density and sea state. Water-in-oil emulsions have higher density than the parent oil and may tend to submerge more easily. However, as long as density of the parent oil is below the density of the ambient sea water (i.e. buoyant), emulsions formed with the same sea water will also be buoyant, but closer to neutral, unless sediment material becomes embedded in the oil.

In the weathering flume tests, lumps of emulsion were observed to form when a slick of weathered water-in-oil emulsion passed the breaking wave in the flume. Some simple tests were performed in order to investigate the potential for submersion of these lumps. The tests were performed by

isolating a lump of emulsion formed, and displacing it to the bottom of the tank inside an inverted cup. By turning the cup right side up, the lump could be released, and its rise velocity recorded by video (Figure 4.14). Rise time and height were extracted from the video, and the rise velocity was calculated (Table 4.4).

Table 4.4 Calculated rising velocity for lumps of emulsion

	Density (g/ml)	Average rising velocity (cm/sec)	% stdev
IF 380 13°C	1.006	12.7	11
IF 380 5°C	0.999	12.3	27
IF 180 13°C	1008	12.9	30

The calculated rise velocities varied from 10-15 cm/sec for all emulsions. Only a limited number of tests were performed, but all rise velocities were of the same order of magnitude as rise velocities found for oil droplets in the size range of 10 mm and above.

In order to obtain a better understanding of the behavior of such weathered lumps of emulsion depending on oil properties and sea state, we initiated a computational investigation of the motion of such lumps in waves by use of a general fluid flow model (FLOW-3D). The final findings from the study are found in Appendix B.

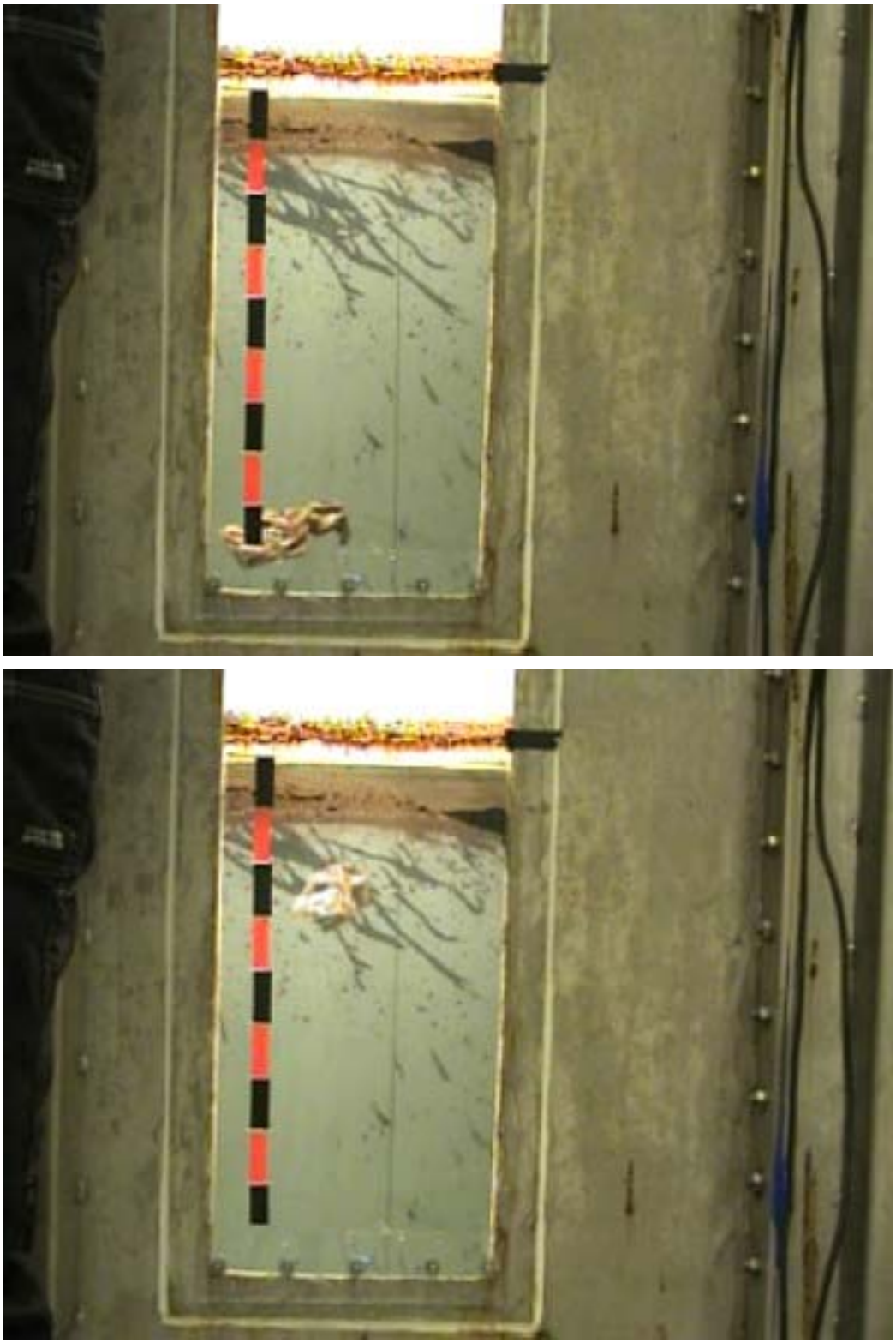

Figure 4.14 Rise of a lump of emulsion formed in the experiment with IF380 at 13°C.

4.2.5 Droplet size distributions over time

As explained in Section 3.1, the LISST could not be used to measure droplet size distributions during actual breaking wave events, since the processes of interest are complete after a few seconds, during which time the LISST has only been able to sample a small volume of water at a single location. Such results are very sensitive to the location of the sampling site relative to the breaking wave, are non-synoptic and very difficult to interpret. In addition, the LISST became very rapidly fouled by the oil, requiring constant cleaning and re-positioning, and interfering further with the possibility of interpreting the data.

However, in a previous weathering flume study with a medium North Sea crude oil (Sture Blend with a fresh oil density of 847 kg/m^3), long term data were obtained with the LISST positioned as shown in Figure 4.15, at a depth of approximately 80 cm. The distance between the breaking wave and the measuring position represents about 45 seconds in circulation time, such that larger droplets would in general resurface before reaching the LISST.

The measurements give an indication of the extent to which smaller droplets accumulate in the water column, representing a balance between entrainment of new droplets in the smaller size range, and eventual resurfacing (Figure 4.16). Figure 4.17 shows the same data in a three-dimensional graph. This figure more clearly shows the increase in concentration associated with droplets less than about 400 µm in diameter, reaching a maximum at about 4 hours, and decreasing thereafter. These graphics reflect the fact that smaller droplets are no longer created as the viscosity of the emulsion increases, at least at the energy levels available in these experiments. These findings are also expected to be valid for the oils tested in the present study, since the properties of the crude oil in the test where in the same range as the oils used in the present study.

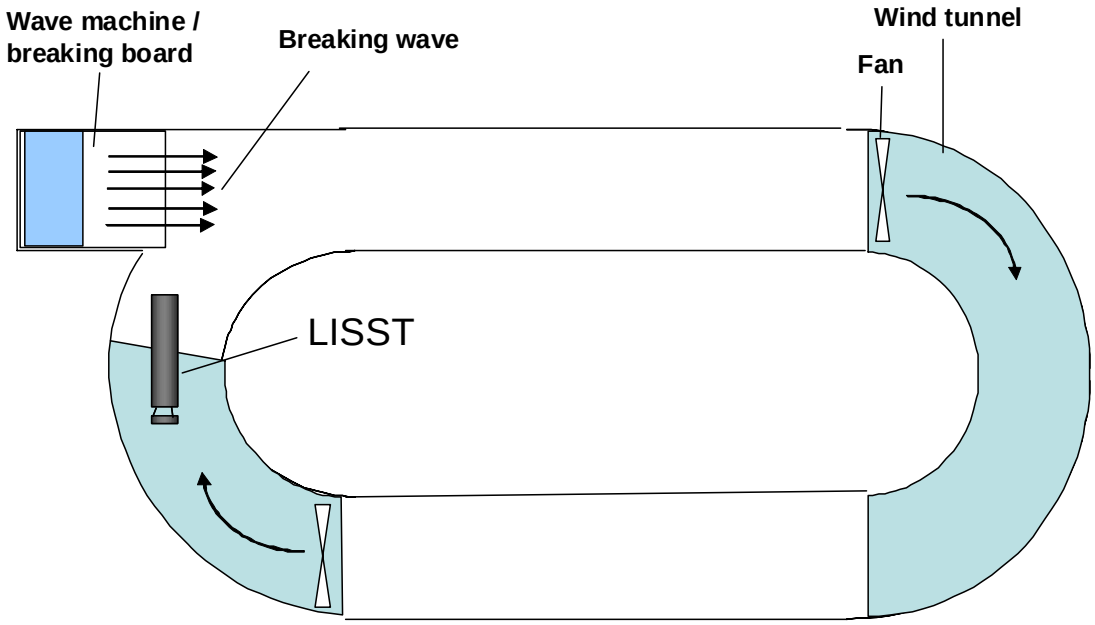

Figure 4.15 Position of the LISST during 20-hour recording of droplet size distributions during a weathering experiment

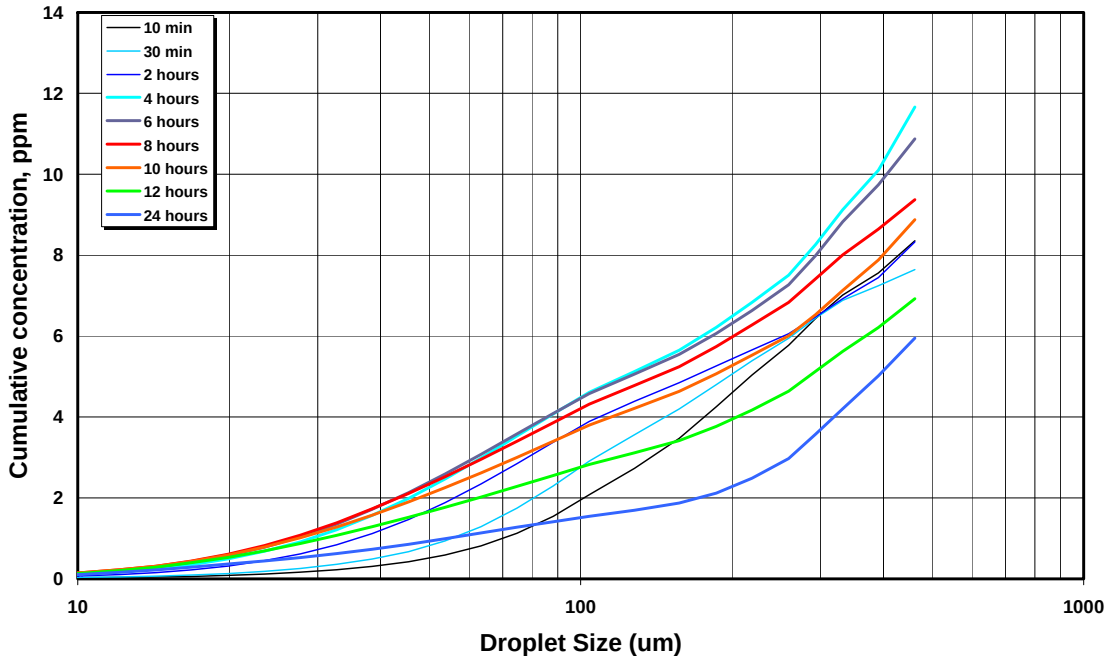

Figure 4.16 Changes in droplet size distributions over time during a 24-hour recording session with the LISST in situ. Maximum concentrations are recorded after 4 hours, after which time concentrations associated with droplets in the range 50 – 250 um are reduced. At about 4 hours the resurfacing of droplets starts to occur more rapidly than the introduction of new droplets through entrainment. The entrainment rate is reduced due to the increase in viscosity through evaporation and emulsification.

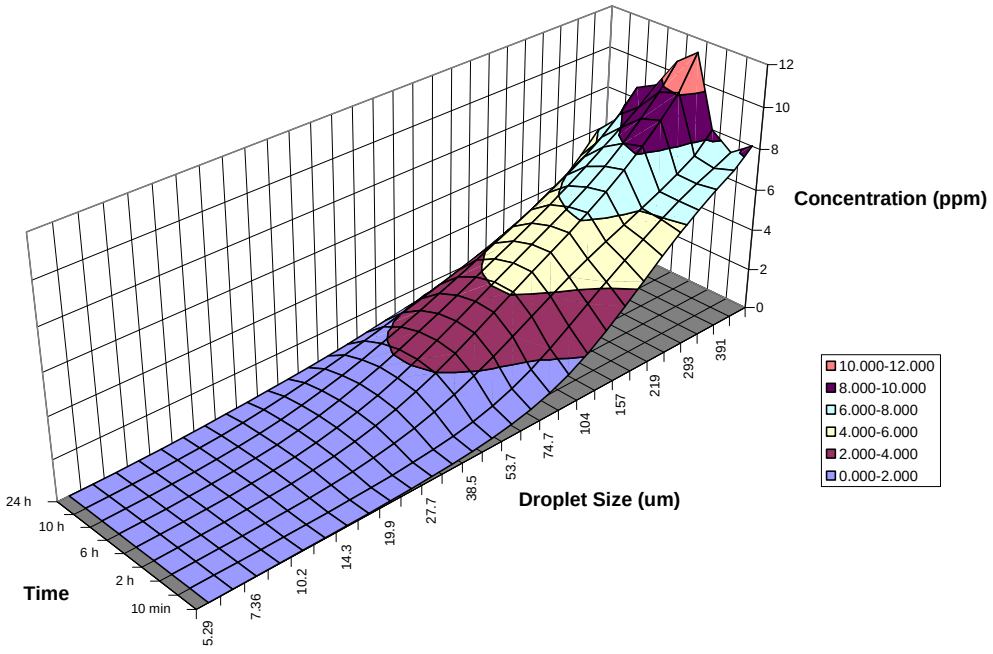

Figure 4.17 As in Figure 4.16, 3-dimensional view showing more clearly the rise and fall of the concentration of small droplets over the first 24 hours of the experiment.

4.3 Plunging jet experiments

Plunging jet experiments were conducted at intervals during the regular oil weathering tests, the first about one hour after test initiation. The wave generator in the weathering flume was shut down some minutes prior to the experiments to allow resurfacing of dispersed oil droplets, and the oil was confined behind a barrier inserted downstream of the test section to obtain a homogeneous oil slick below the plunging water jet. All experiments were conducted with the plunging jet apparatus described previously (Section 3.2). The experimental conditions were varied from one test to the next, with the aim of obtaining a picture of the droplet cloud with sufficient quality for subsequent digital image processing. Most flume tests were conducted at two different water temperatures (5 and 13 ^{o}C). Most tests were conducted with artificial sunlight, but a few tests were made without solar exposure. Tests without solar exposure are marked “no sun”, while tests exposed to sun are marked “w/ sun” in *Table 4.5*.

The film thickness of the confined oil layer differed from one experiment to the next since water-in-oil emulsions with densities approaching the density of sea water tend to form thicker oil layers than more buoyant water-free oil. The free fall height had to be increased from time to time to compensate for the increasing resistance to break-up of the oil film caused by increased viscosity and film thickness. The fall height is recorded in *Table 4.5*.

In the weathering tests with heavy fuel oils, IFO 180 and IFO 380, we were unable to obtain droplet cloud pictures for digital processing. In these cases, the plunging water jet resulted in large irregular oil globules with very brief submersion times, or more often the jet was unable to break through the oil layer at all. In general, we found that the energy level of the entrainment method used here was sufficient for cases with oil/emulsion viscosities below about 10 000 mPas. A higher energy methodology will be necessary for higher viscosities and thick emulsion layers.

An overview of the results from the plunging jet experiments is given in *Table 4.5*. The table contains the experimental conditions in each test and the resulting median droplet size and logarithmic standard deviation obtained from the digital processing of the images of the droplet clouds, where such data were obtained.

The surface tension data given in *Table 4.5* were based on measurements on water-free oil at various degrees of weathering made independent of the oil weathering tests. The emulsion viscosity and density were measured on samples taken prior to each plunging jet experiment, and were measured at a shear rate of 10 s^{-1} at the temperature used in the respective tests (5 or 13 ^{o}C).

The median droplet diameter and the logarithmic standard deviation were obtained from automated droplet counts performed by digital analysis of pictures selected from a sequence of pictures recorded at a rate of 5 per second. The picture to be analyzed was selected by visual inspection of the series obtained in the experiment. A picture judged as the best suited for digital analysis was selected, and, in order to check that this picture was representative, two additional pictures were selected two frames before and after the best selection. A comparison among three such pictures is shown in Figure 4.18 and Figure 4.19. The former figure shows the three picture frames that were used in the digital analysis, while the latter shows the droplet number distributions obtained from the automated droplet counts. The solid black line in Figure 4.19 shows the droplet number distribution obtained by combining the three data sets.

Table 4.5. Overview of experimental and analytic results

	Time from start	Film thickness	Fall height	Emulsion viscosity	Emulsion density	Surface tension	Median diameter	Standard dev.
	Hour or days	mm	cm	mPas	g/cm^3	mN/m	mm	log
Troll [a]								
5°C no sun	1 hour	10	10	1508	0.992	13	0.386	0.389
	6 hours	15	20	2765	0.998	13	0.425	0.332
	1 day	15	30	3645	1.002	14	0.440	0.328
	2 days	15	30	4593	1.003	14	0.394	0.352
5°C w/sun	1 hour	5	10	1750	0.992	13	0.340	0.410
	6 hours	5	10	2620	1.007	13	0.443	0.400
	12 hours	5	10	5940	1.007	14	0.495	0.419
13°C w/sun	1 hour	15	10	43	0.978	13	0.577	0.370
	6 hours	15	10	1840	0.992	13	0.500	0.380
	1 day	30	10	8133	1.000	14	0.467	0.317
	3 days	15	10	13356	1.005	14	0.289	0.298
	3 days	15	20	13356	1.005	14	0.343	0.309
North Slope								
13°C w/sun	1 hour	4	10	56	0.902	22	0.329	0.322
	6 hour	7	10	1659	0.987	25	0.511	0.425
	1 day	3	20	7332	1.001	26	0.275	0.300
Norne [a]								
5°C no sun	3 hours	3	20	4448	0.934	10	0.462	0.266
	1 day	3	20	564	0.980	12	0.524	0.293
13°C w/sun	6 hours	5	20	2290	0.931	10	0.251	0.428
Grane								
13°C w/sun	1 hour	7	20	3810	0.991		0.160	0.374
	6 hours	10	30	5280	1.003		0.203	0.387
IFO 180								
13°C w/sun	1 hour	17	20	9160	0.979		0.176	0.341
	12 hours	10	20	21300	0.996		0.179	0,429
IFO 380 [a]	Neither natural dispersion nor sinking observed at test energy levels						NA	NA

[a] The flume tests for these oils were conducted in the parallel study financed by A/S Norske Shell, StatoilHydro AS and Eni Norge AS.
NA: measurement not available

As Figure 4.19 indicates, the droplet size distributions obtained from the three frames were quite similar, with median diameters ranging from 0.57 to 0.61 mm, and standard deviations varying slightly from 0.36 to 0.38 in $\log_{10}$ units. The median diameter and logarithmic standard deviation from the combined data was 0.592 ± 0.018 mm and 0.367 ± 0.013, where the values after the $\pm$ sign represents the uncertainty (one standard deviation from the mean).

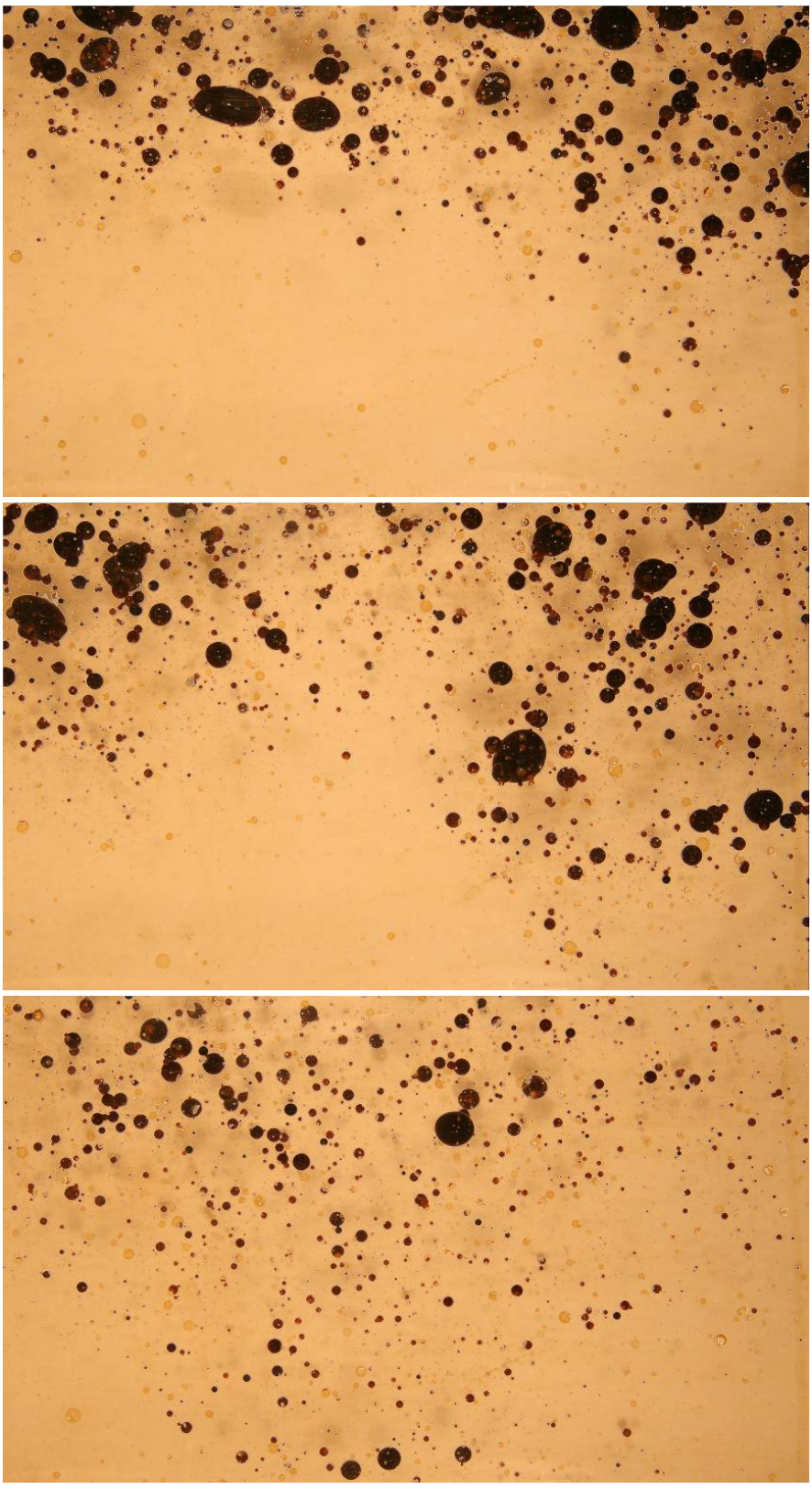

Figure 4.18. Examples of pictures from plunging jet experiments with Troll crude at 13°C. Pictures of droplet clouds obtained in three subsequent pictures 1 hour after start of the flume test. Picture numbers are given to the right of each picture. Note that the picture sequence is obtained within a time period of about 5 seconds.

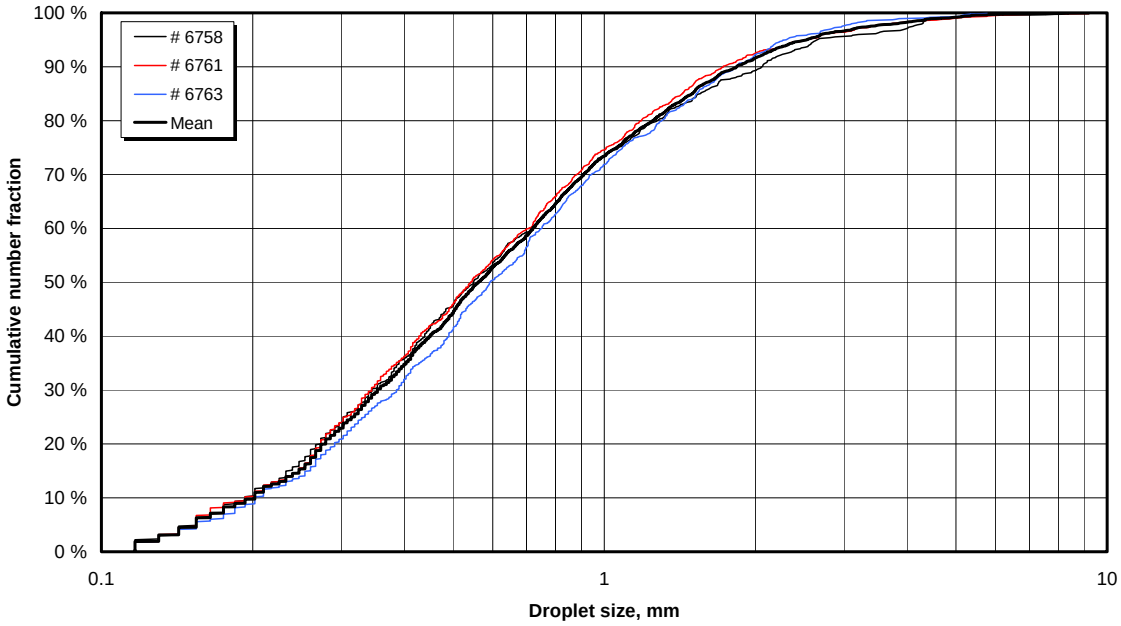

Figure 4.19. Droplet number distribution obtained from the three subsequent picture frames shown in Figure 4.18. The thick black line shows the distribution obtained from a combination of the three data sets.

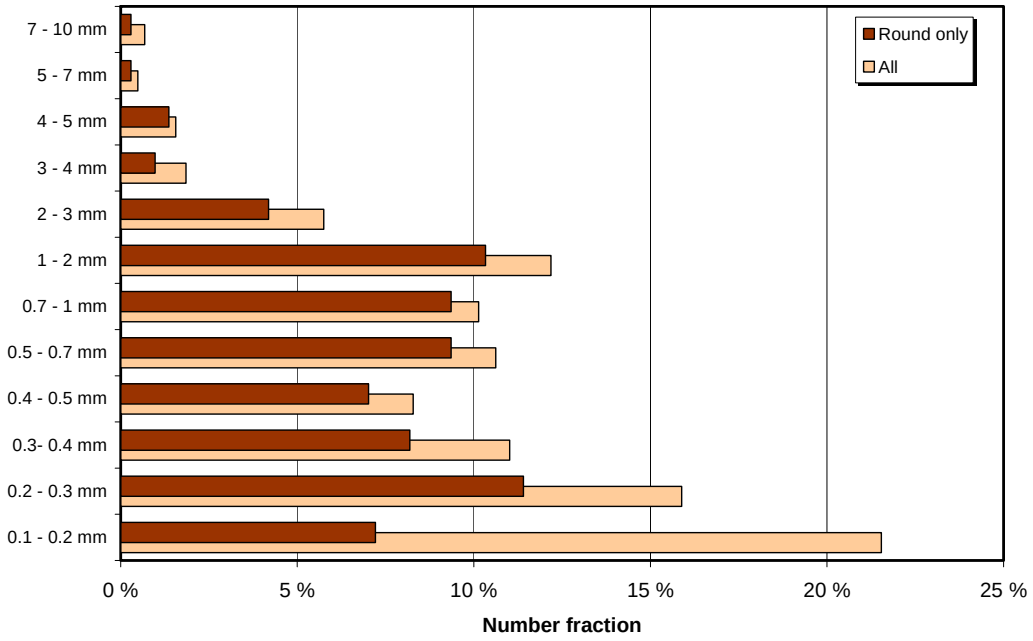

Figure 4.20. Droplet number distribution in bins (d = 0.1 – 0.2 mm, 0.2 – 0.3 mm etc.) obtained from digital analysis of picture # 6758 from Figure 4.18. Bars in light colors are based on counts of all objects, while a roundness criterion R > 0.8 is applied to the bars shown in dark colors. Note that in both cases, the number fractions in each bin are relative to the total number of identified objects before application of the roundness criterion. The large number of rejects in the smallest bin reflects the rejection of background particles in the seawater.

The same strong resemblance was found for pictures selected from the other tests, and for this reason, the droplet size distribution parameters given in Table 4.5 are based on the digital analysis of the selected "best" picture, without biasing the results significantly.

The droplet size data obtained from the digital image analyses contains the equivalent diameter of each identified object in the picture, presuming a circular shape, in addition to the length and width of the object in x- and y-directions (Feret's diameters, or maximum and minimum calipers). Most droplets in the medium to small size range are found to be close to circular, but some objects may represent two or more overlapping droplets. In the present study, a roundness criterion corresponding to a Feret's diameter ratio of $0.8 < R < 1.2$ has been used in order to eliminate objects that are formed by overlapping droplets. However, this criterion may also eliminate some of the larger droplets that may have an elongated shape. These droplets are normally few in number, and will not contribute significantly to the overall number distribution parameters.

This assumption seems to be supported by the results shown in Figure 4.20 from the analysis of one of the pictures. The results of the automated droplet counts are shown in distinct size bins (d = 0.1 – 0.2, 0.2 – 0.3 mm, etc) with and without application of the roundness criterion. The figure demonstrates that application of the roundness criterion tends to eliminate more objects both in absolute and relative terms in the small to medium size range (< 1 mm), than in the large size range (> 1 mm). The large number of rejects in the smallest bin reflects the rejection of background particles in the seawater. (See also discussion in Section 3.1.)

4.4 Algorithm for oil droplet size distribution

4.4.1 Delvigne's Studies

Most state of the art oil drift models apply algorithms for natural dispersion based on the breaking wave experiments conducted by Delvigne and collaborators in the late 1980's and early 1990's (Delvigne and Sweeney 1988, Delvigne 1993, Delvigne and Hulsen 1994). These studies led to a simple empirical correlation among oil viscosity, sea state and the size distribution of droplets entrained by breaking waves. This correlation relates to the first stage of the natural dispersion process (droplet formation and entrainment), while a complete description of the actual dispersion process implies modeling of the subsequent fate of the entrained oil droplets (vertical mixing, resurfacing).

The experimental study of natural dispersion of oil conducted by Delvigne and Sweeney (1988) included three parts. The first part related to droplet formation in homogenous turbulence, and was conducted in a grid column, a vertical cylindrical container where turbulence was generated by an oscillating grid. The second and third parts of the study were concerned with droplet formation in breaking waves, and were conducted partly in a small scale wave flume (15 m long, 0.5 m wide with 0.4 m water depth), and in a large scale flume (200 m long, 5 m wide and 4.3 m water depth). In the small flume, the wave height was in the order of 0.2 m, while wave heights up to 2 m could be generated in the large flume. The turbulent break up experiments indicated a certain dependency of turbulent dissipation rate and oil viscosity on the characteristic droplet size (the droplet size tended to decrease with increasing dissipation rate and increase with increasing viscosity). The dependency on the dissipation rate seems to correspond with the theory for droplet breakup in homogeneous and stationary turbulent flows, but the relevance of such observations for droplet splitting in breaking waves is questionable, mainly due to the intermittent nature of the wave breaking process.

The breaking wave experiments indicated that the initial oil droplet distribution is determined by two major factors – wave energy (external factor) and oil viscosity (internal factor). Based on a number of

experiments with different oils and variable breaking wave heights, Delvigne and Sweeney derived the following empirical equation for the oil mass entrained by breaking waves:

$$\frac{dQ}{dD} = C_o \, E_w^{0.57} \, D^{0.7} \tag{4.1}$$

where Q (kg/m^2) is the entrained mass per unit area of oil droplets with diameter less than or equal D (m), C_o is an oil related constant, and E_w is the dissipated breaking wave energy per unit surface area, expressed in terms of the significant wave height H_s by the equation $E_w = 0.0017 \rho_w \, g \, H_s^2$,[2] where ρ_w (kg/m^3) is the density of sea water, and g is the acceleration of gravity (m/s^2). It should also be noted that this droplet entrainment equation to a large extent depends on the power law relationship that was found for the droplet size distribution of dispersed oil:

$$\frac{dN}{dD} \propto D^{-2.3} \tag{4.2}$$

where N is the number of droplets with diameter less than or equal D.

The authors claim that this power-law relationship was valid for all experiments independent of oil type, weathering state, oil layer thickness, temperature and type of breaking wave. The corresponding volume distribution function dV/dD, where V is the volume contained in droplets with size up to D, can be derived from this equation by taking into account that the droplet volume is proportional to D^3. This explains the exponent of 0.7 in Eq. 4.1 (-2.3 + 3 = 0.7).

Equation 4.1 can be integrated to give the entrained oil mass contained in droplets up to a certain diameter D:

$$Q(D) = C'_o \, E_{bw}^{0.57} \, D^{1.7} \tag{4.3}$$

where $C'_o = C_o / 1.7$.

This entrainment equation includes one term related to the physical properties of the oil (C_o), and one term related to the sea state, E_{bw}. As indicated above, the latter term is proportional to the wave height squared, and within the experimental uncertainties the exponent of 0.57 may as well imply a linear dependency between entrained mass and wave height.

In the original paper, the authors argued for a possible inverse relationship between C_o and the oil viscosity ν_o, $C_o \propto \nu_o^{-1}$, but this relationship was not confirmed in a series of simple plunging jet experiments reported later by the same lead author (Delvigne and Hulsen, 1994). These experiments showed that the resulting droplet size distribution was more sensitive to variations in viscosity for high-viscous oils (kinematic viscosity > 100 cSt), than for low-viscous oils (Figure 4.21).

[2] Delvigne and Sweeney used the r.m.s value of the wave height in their original equation. We have restated the equation in terms of significant wave height, taking into account that $H_{rms} = H_s / \sqrt{2}$

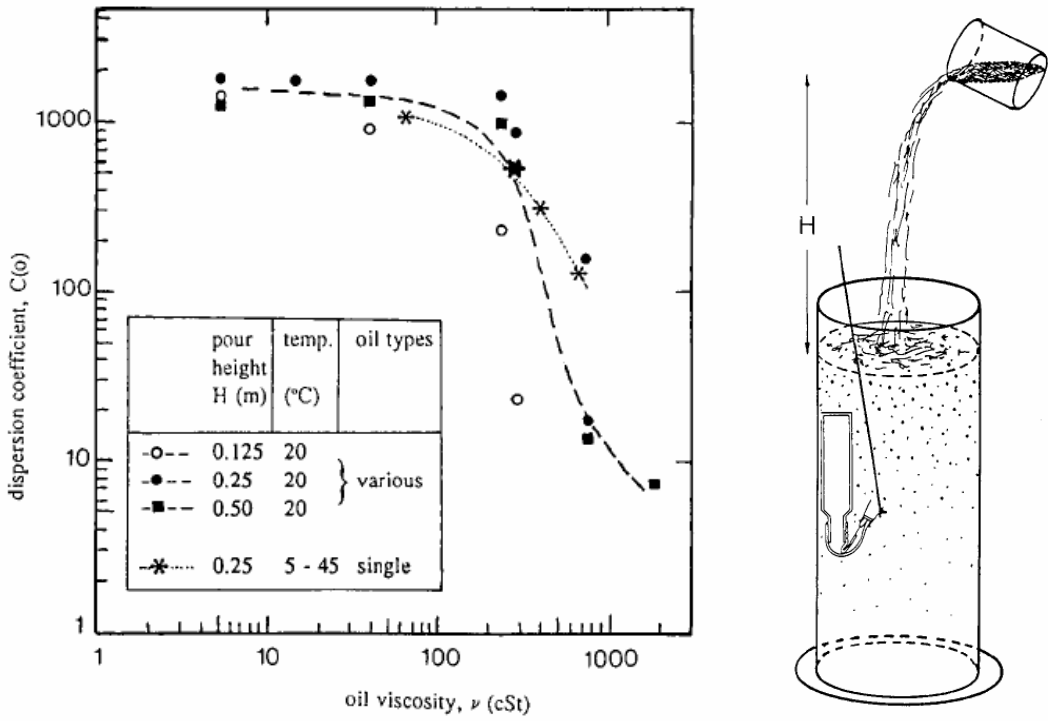

Figure 4.21. Variation of dispersion coefficient with oil viscosity. Data from plunging jet experiments (Delvigne and Hulsen, 1994). The attached drawing describes the experimental setup.

The authors also stated that the droplet size distribution appeared to be independent of the oil film thickness, at least within the experimental range of 0.2 to 1.2 mm. However, they also point out that the film thickness may impose an upper limit on the droplet size.

By assuming that the entrainment relationship (Eq. 4.3) is valid from the smallest to the maximum droplet size, and assuming that the total surface oil mass is entrained by the breaking wave, the maximum droplet size may be found by equating the entrained oil mass to the surface oil mass; $Q(D_{\max}) = \rho_o\, h$, where ρ_o (kg/m^3) is the density of the surface oil, and h (m) is the thickness of the oil slick. Equation 4.3 will then give:

$$D_{\max} = \left(\frac{\rho_o\, h}{C'_o\, E_{bw}^{0.57}} \right)^{1/1.7} \tag{4.4}$$

Delvigne and Sweeney (1988) also defined the entrainment rate per unit area, Q_R (kg/m^2/s), which they assumed would be suitable for practical applications. This rate is found by introducing a breaking wave rate F_{bw}, representing the fraction of the sea surface hit by breaking waves per unit time, $Q_R(D) = C'_o\, E_{bw}^{0.57} D^{1.7} F_{bw}$. The breaking wave rate can be expressed in terms of the white cap coverage S_{bw} and the mean wave period T_m (s); $F_{bw} = S_{bw} / T_m$.

However, in practical applications (oil weathering and oil drift models) entrainment and droplet formation are likely to be conceived as two distinct processes. The surface oil mass per unit area, together with the breaking wave rate F_{bw} defines the total entrainment rate, while the entrainment equation (Eq. 4.3) defines the size distribution of the entrained droplets. Assuming that the power law

distribution is valid for the full range of droplet sizes, the cumulative size distribution can in fact be expressed simply as $V(D) = \left(D / D_{\max}\right)^{1.7}$, where $D_{\max}$ is defined by Eq. 4.4.

The subsequent fate of the droplets (residence time in the water masses) can then be determined from the rise velocities of the droplets (depending on droplet size and oil density) and vertical turbulent mixing in the surface layer induced by wind and waves. In some applications, e.g. ADIOS (Lehr et al. 1992), Delft-3D (Delft Hydraulics 2005), SINTEF OWM (Daling & Strøm, 1999), this problem is simplified by assuming that droplets below a certain critical diameter $D_{\lim}$ will be permanently entrained, while droplets above this diameter will resurface. In that case, the oil mass entrained per unit area by each breaking wave is found simply by inserting $D = D_{\lim}$ in Equation 4.3, and the oil mass per unit area entrained over a time interval Δt is determined by the number N_{bw} of waves breaking in a unit area in the given time interval, $N_{bw} = F_{bw}\,\Delta t$. However, the magnitude of the critical droplet size differs considerably between the different applications (i.e. from 60 to 300 μm) – partly depending on the choices of the other model parameters – and should thus be conceived more as a tunable model parameter than an actual measure of the limiting droplet size for permanent entrainment.

However, it should be noted that these predictions rely on some important assumptions and experimental limitations inherent in Delvigne's study:

First, the entrainment equation depends to a large extent on the postulated power law droplet size distribution (Eq. 4.2). In fact, Delvigne and Sweeney (1989) have taken the general inclination of the distribution function for granted (i.e. the exponent was fixed) and limited the curve-fitting to droplets less than 200 μm, arguing that these size classes had not been distorted by resurfacing during sampling. Extrapolation of this distribution function to larger droplet sizes is therefore questionable. As our experimental studies have shown, another distribution function might have been used to fit the full range of droplet sizes (e.g. the lognormal distribution).

Second, the influence of the oil properties on entrainment was expressed in the entrainment coefficient C_o, which the authors found to depend on the viscosity of the oil. In the original paper, the authors argued for a linear inverse relationship, but this relationship was not confirmed in subsequent studies (Delvigne and Hulsen, 1994). The viscosity-dependency is thus one of the major uncertainties in relation to the use of the findings from these studies, also due to the fact that the experiments covered a rather limited viscosity range.

Finally, it should be mentioned that the entrainment equation (Eq. 4.3) is purely empirical without any theoretical basis. Moreover, the equation is not expressed in terms of normalized or non-dimensional variables commonly used in scientific studies of hydraulic phenomena, and has dimensions without any physical significance.

4.4.2 Theory of Droplet Formation

Theoretical studies of droplet formation indicate that different criteria apply to droplet splitting (Li and Garrett, 1998), depending on the flow conditions. In turbulent regimes, bubble and droplet formation is related to the Weber number, $We = \rho u'^2 D / \sigma$, while in shear flow, droplet breakup is related to a capillary number, $Ca = \mu S D / 2\sigma$. The variables in these dimensionless numbers are:

σ (N/m), interfacial tension between oil and water,
u' (m/s), mean turbulent velocity fluctuations,
D (m), droplet diameter,
μ (kg/m/s) and ρ (kg/m^3), dynamic viscosity and density of the continuous fluid (water),
S (s^{-1}), shear rate or velocity gradient, and

It should be noted that the viscosity of the dispersed phase (oil) is not found explicitly in either of these dimensionless numbers. However, the viscosity ratio between the dispersed and continuous phase, $\lambda = \mu_d / \mu$ enters into the criterion for breakup in shear flow, i.e. in the *critical capillary number* which is related to the viscosity ratio by a so-called Grace curve (Janssen and Meijer, 1993).

Hinze (1955) discussed breakup of droplets in turbulent flow and argued that the size of the largest droplets is determined by dynamic pressure forces that are caused by changes in velocity over distances at most equal to the diameter of the droplet. This implies that eddies that can break a droplet are of the droplet size, while larger eddies will just move the drop, and the smaller ones are too weak to cause breakage. On this basis, he formulated the criterion for droplet breakup as

$$\frac{\rho \left\langle v^2 \right\rangle D_{\max}}{\sigma} = We_c , \tag{4.5}$$

where $We_c \approx 1.2$ is the critical Weber number, and $\left\langle v^2 \right\rangle$ is the average value across the whole flow field of the squared velocity differences over a distance equal to the maximum stable droplet diameter, D_{max}.

In order to derive an expression for the maximum droplet diameter, he made use of the fact that under certain conditions (homogeneous turbulence), the velocity differences at different length scales *d* are determined by the energy input ε (m^2/s^3) per unit mass and unit time, $\left\langle v^2 \right\rangle \approx 2(\varepsilon D)^{2/3}$. By substituting this into Equation 4.5, Hinze arrived at the following expression for the maximum droplet size in turbulent flow,

$$D_{\max} = c\left(\sigma / \rho\right)^{3/5} \varepsilon^{-2/5},$$

where $c \approx 0.7$ is an empirical constant. It should be noted that this breakup criterion defines the maximum stable droplet size, but many fine droplets will be produced even if larger droplets are stable.

However, experimental studies of droplet splitting in breaking waves clearly demonstrate that the droplet size depends on the viscosity of the oil, at least in experiments with oil of moderate to high oil viscosities (Figure 4.21). Hinze was aware of this fact and introduced a non-dimensional viscosity group $Vi = \mu_d / \sqrt{\rho_d \, \sigma \, D}$, where μ_d and ρ_d are properties of the dispersed phase. He postulated that the critical Weber number was a function of this group, $We_c = C\left[1 + \varphi(Vi)\right]$, where *C* is the value of the critical Weber number for vanishing viscosity effects. Even if the function $\varphi(Vi)$ is not known in general, and probably will depend on the type of flow, this idea might prove to be a useful for normalization of experimental data.

From a practical point of view, the definition of the Weber number is an open question. Preferably, the velocity and length scales should be based on directly measurable variables, and if possible, defined by the experimental conditions. As an example, Martinez-Bazan (2002) defined an empirical formula for breakup of air bubbles in a water jet in terms of a jet Weber number $We_J = \rho U_J^2 D_J / \sigma$, where U_J is the jet exit velocity and D_J is the nozzle diameter. The maximum bubble size was expressed in terms of this Weber number by the relationship

$$D_{\max} / D_J = F \; We_J^{-3/5},$$

where *F* is a coefficient depending on the size of the injected bubbles and the location of the injection point.

In the context of oil droplet breakup by breaking waves, the oil slick thickness h might be chosen as the length scale, and the velocity scale might be expressed in terms of the free fall velocity $V_H = \sqrt{2gH}$, where H is the wave height. The characteristic droplet size might be expressed as

$$D/h = F\,We_H^{-p}, \tag{4.6}$$

where p is an empirically determined exponent, $We_H = \rho g H h/\sigma$ and the coefficient F is related to the properties of the oil, expressed as $F = f(Vi)$, where $Vi = \mu_d/\sqrt{\rho_d \sigma h}$ is the viscosity group, with the oil film thickness h replaces the droplet size used originally by Hinze.

Equation 4.6 combines the major experimental variables in non-dimensional form, and might prove to be useful for generalizing experimental data. Since the droplet size data from our experiments was found to fit closely to log-normal number distributions with a fairly constant standard deviation, the characteristic droplet size D in this equation might be unambiguously defined in terms of the median diameter D_{50}. Certain characteristics of the lognormal distribution will be discussed in the next section.

4.4.3 Size distribution functions

In the previous section, two types of droplet size distribution functions have been mentioned – the power law distribution used by Delvigne and the log-normal distribution found from our experimental studies. According to Mitzenmacher (2003), the argument over whether a lognormal or power law distribution is a better fit for some empirically observed distributions has been repeated across many fields over many years. He also points out that power law and lognormal distributions are intrinsically connected, and concluded that very similar basic generative models can lead to either power law or lognormal distributions, depending on seemingly trivial variations.

Mitzenmacher defines a power law distribution for a non-negative random variable X in terms of the equation $\Pr[X \geq x] \approx c\,x^{-\alpha}$ with constants $c > 0$ and $\alpha > 0$. The $\approx$ sign is used to indicate that a power law distribution can not be valid down to infinitely small droplet sizes, since at some limiting small value of x (depending on c), the calculated probability will reach an unrealistic value larger than one. This is taken into account in the Pareto distribution, defined by the equation $\Pr[X \geq x] = (x/k)^{-\alpha}$, with the requirement $X \geq k$. On a log-log plot, the Pareto distribution will show a straight line with a slope $-\alpha$. Mitzenmacher also mentions a novel type of power law distributions called a double Pareto distribution, originally derived by Reed (2001). In a log-log plot, this function has a density distribution that consists of two straight segments that meet at a transition point. Assuming that the transition point is at $x = 1$, the density function for $x > 1$ can be expressed as $f(x) = (\alpha/2)\,x^{-\alpha-1}$, while for $x < 1$, $f(x) = (\alpha/2)\,x^{\alpha-1}$, where the constant $\alpha \geq 1$. Reed (2001) points out that certain economic variables (e.g. the size of settlements) show power law distributions at both tails, and offers a theoretical explanation for this double Pareto type of behavior. According to Mitzenmacher, the double Pareto distribution function can be made to closely match the body of a lognormal distribution and the tail of a Pareto distribution.

More recently, however, Eekhout (2004) discussed the relevance of lognormal vs. Pareto type distributions for the size of US cities, and found that data covering the entire size distribution (not only the largest) could be fitted successfully with a lognormal distribution. He also tried to fit Pareto distributions to the upper tail of the data, but concluded that the estimated slope was strongly sensitive to the choice of the truncation point. In contrast to most previous studies that used data for

metropolitan areas (MAs) in the US (the 100 largest cities), Eekhout used data for the entire range of US settlements, ranging from villages to towns and cities, comprising more than 25 000 settlements.

Eeekhout found that the observed lognormal distribution follows from the law of proportionate growth (Gibrat's law), which states that cities (or companies) grow at a stochastic rate that is independent of the city (company) size. The existence of a fixed growth rate was confirmed from the available data. He remarked that his findings could be made because of availability of new data that covered the entire size distribution. Interestingly, he notes that a change of conclusion following availability of new data is a common occurrence in science, and he refers to a similar phenomenon related to the size distribution of aerosol particles in the atmosphere (quote):

> "When the measurement of particles is restricted to those with the largest size (often due to the absence of measurement technology that can capture the distribution of the smaller ones), the resulting observed distribution is in fact the truncated distribution and is often fit to a power law. With the advent of advanced measurement technology, however, smaller particles and hence the total size distribution can be measured. [..] For the entire size distribution of many aerosol types, the distribution is actually lognormal, or a convolution of different lognormals."

This brief review of distribution functions shows that discussion about the use of lognormal or power law distributions is an unresolved issue in many different fields. In practice, however, the choice between the two must be decided on the basis of the quality of the fit to the empirical data. In order to illustrate this point, we have compared the two distributions with droplet size data from the flume tests (Figure 4.22). The lognormal distribution shows an excellent fit to the whole range of the data, while it not possible to fit the whole range with the Double Pareto distribution.

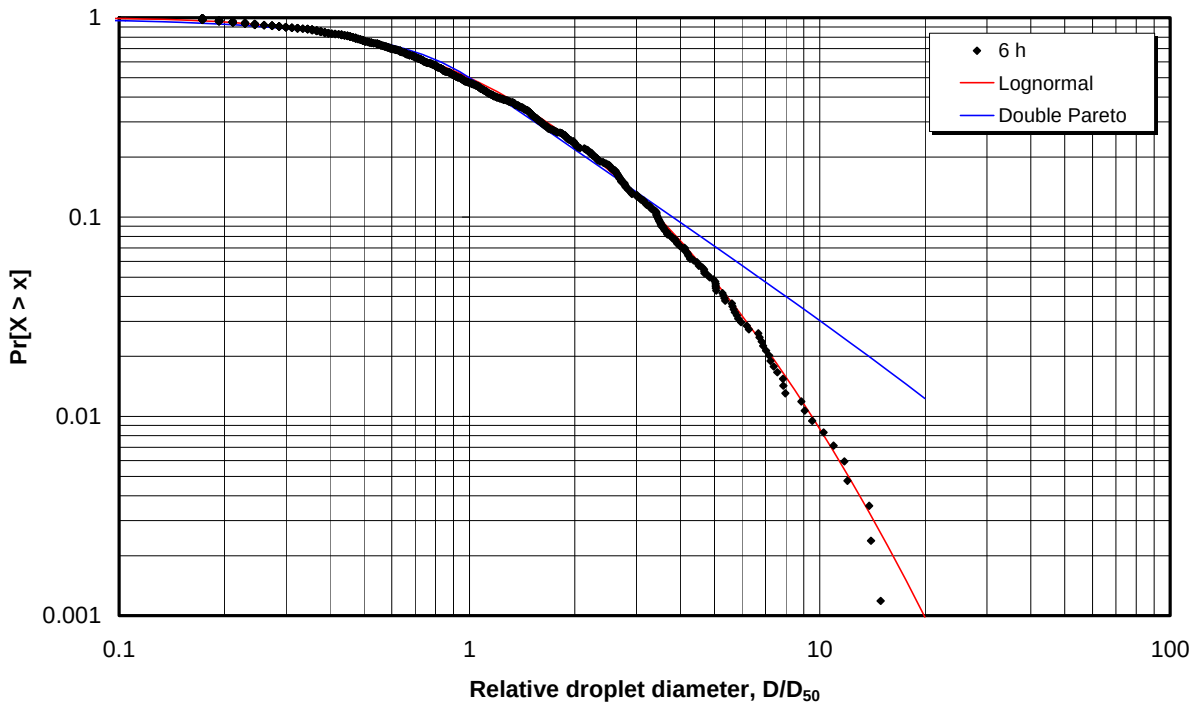

Figure 4.22. Cumulative droplet number distributions obtained from plunging jet experiments with Troll crude at 5 °C. Markers show droplet diameters from image analysis scaled by the logarithmic mean diameter (D_{50}).The data points are from one of the plunging jet experiments conducted 6 hours after start of the flume test. The red line is a lognormal distribution with logarithmic standard deviation s = 0.42, while the blue line is a Double Pareto distribution with $\alpha = 1.2$.

It should be noted that the droplet size distributions determined in the flume test represent number distributions. However, a log-normal number distribution may be transformed into a log-normal volume distribution by an up-scaling of the logarithmic mean diameter:

- Assuming spherical droplets, the volume of each droplet will be proportional to the cube of the diameter, $v_i \sim d_i^3$.
- Then, if the mean logarithmic diameter in the number distribution is m, the standard deviation of the volume distribution will be the same, while the mean logarithmic diameter will be $m_V = m + 3s^2$, where s is the logarithmic standard deviation of the number distribution.

Since droplet diameters in general will be limited to a certain maximum size (for instance due to resurfacing of the largest droplets), an upper limit log-normal distribution may be a more appropriate choice. This implies that the distribution is assumed to add up to 100 % at a certain maximum droplet size. Such an upper limit distribution can be expressed in mathematical terms as:

$$Q(d) = Normdist(\log d, m_V, s) / Normdist(\log d_{\max}, m_V, s),\ d \le d_{\max}$$

where Q is the cumulative volume fraction contained in droplets with diameter less than d, while m_V and s are the mean logarithmic diameter and logarithmic standard deviation of the unlimited volume distribution.

Figure 4.23 shows an example of a curve fit based on the upper limit lognormal distribution for droplet size data from the plunging jet experiments with Troll crude at 13°C, conducted one day after start of the weathering flume test. Black markers show the number distribution obtained by sorting the droplet diameters from the automated image analysis, while blue markers show the corresponding volume distribution calculated from the same data by assuming spherical droplets. The black line shows the log-normal distribution fitted to the number distribution by use of the mean logarithmic diameter and standard deviation obtained from the droplet size data. The red line shows a log-normal volume distribution which is estimated by assuming unlimited droplet diameters, while the blue line shows the upper-limit log-normal volume distribution based on the maximum droplet size observed in the data.

The upper limit log-normal distribution may seem to be a useful concept for transforming predicted number distributions into volume distributions, but the result will to a large extent depend on the maximum droplet diameter in a given droplet population, which will be difficult to assess.

However, a log-normal volume distribution based on the distribution parameters derived from the experimental droplet number counts may serve as an estimate of the initial droplet size distribution generated in a breaking wave event. With this as the starting point, the subsequent change in this distribution due to resurfacing of the larger droplets may be modeled as a predictable physical process (advection/diffusion).

Figure 4.24 is included to illustrate this point. The figure shows the calculated change in a droplet size distribution due to settling in a well mixed dispersion of oil droplets. The rise velocity of each droplet class is calculated from the droplet diameter and a presumed oil density (950 kg/m^3). The black lines show the initial distributions, while the red lines show the distributions after 60 seconds settling time. It is interesting to note that the calculation shows a marked reduction in the volume median diameter after the settling period, while a more moderate change is found in the number median diameter.

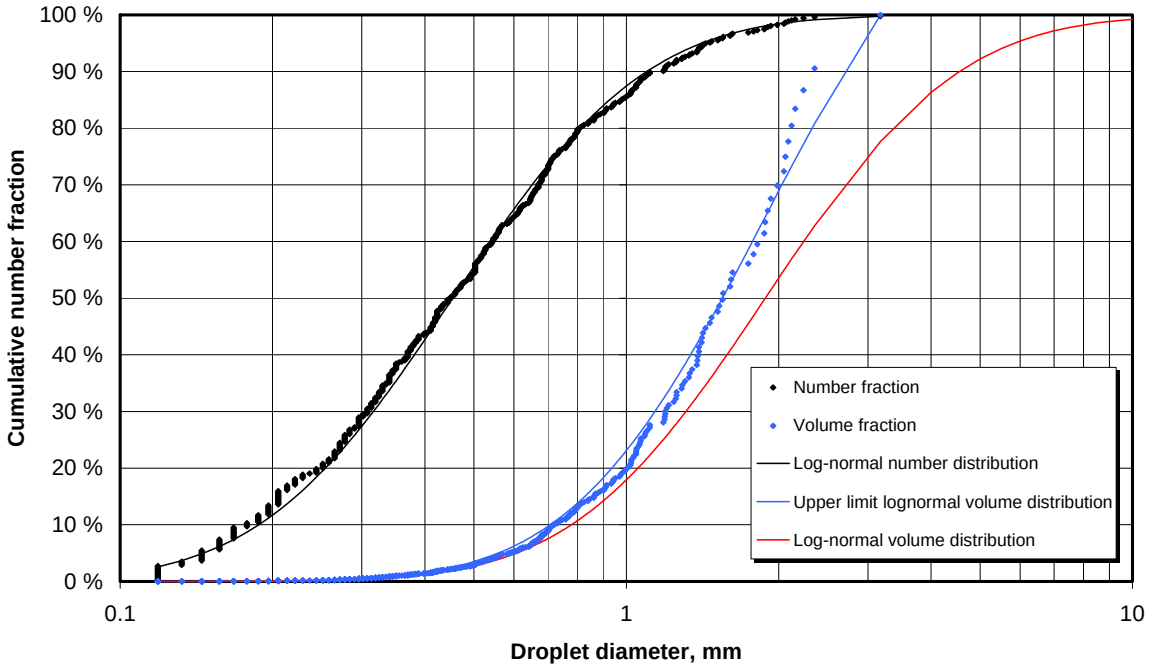

Figure 4.23. Example of application of upper log-normal distribution to droplet size data. See text for details.

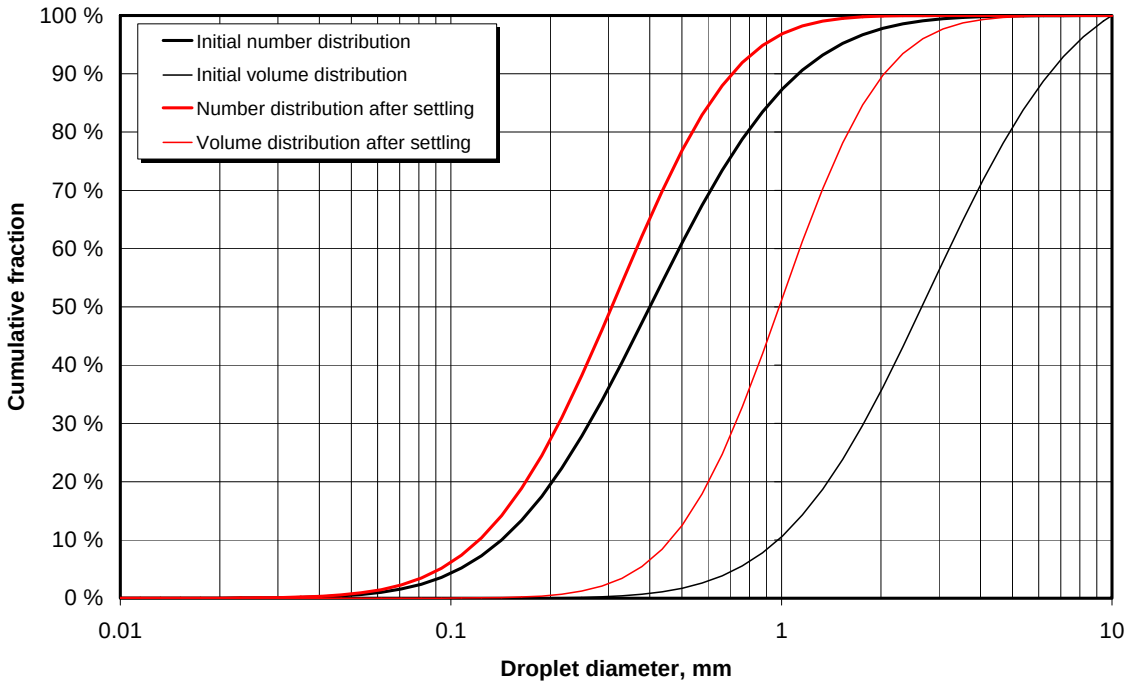

Figure 4.24. Computed change in a droplet size distribution due to settling. Thick lines refer to number distributions, while thin lines are used for volume distributions. The initial distributions are shown in black, while the distributions obtained after a certain settling period are shown in red. Although there are relatively few large droplets, they represent a larger fraction of the total volume, and settle out most rapidly.

4.4.4 Empirical correlation for droplet size

The main objective of the plunging jet experiments was to establish algorithms for prediction of the size distribution of oil droplets formed in breaking wave events. Since the droplet size distributions in general showed a close fit to log-normal number distributions, we concluded that the size distribution may be characterized by two parameters, the mean logarithmic diameter D_{50} and the logarithmic standard deviation s. Since the latter was found to be fairly stable, with no clear trend, we propose that a constant value should be used for this parameter, corresponding to the mean value obtained in the experiments.

In the earlier section on the theory of droplet breakup, we postulated that the median droplet size D_{50} could be expressed by a non-dimensional equation of the form $D_{50} / h = F\,\mathrm{We}^{-p}$. Here h is the oil film thickness, F is a coefficient depending on the viscosity of the oil, We is a Weber number defined as $\mathrm{We} = \rho g H h / \sigma$, where ρ is the density of water, g is the acceleration of gravity, H is the free fall height (or wave amplitude), and σ is the interfacial tension between oil and water. The exponent p will be determined empirically. The coefficient F might be expressed as $F = f(\mathrm{Vi})$, where $\mathrm{Vi} = \mu_O / \sqrt{\rho_O \sigma h}$ is the viscosity group where the oil film thickness h is used instead of the droplet size used originally by Hinze, and μ_O and ρ_O are viscosity and density of the dispersed phase (i.e. the oil). This non-dimensional equation leads to the following explicit equation for the median droplet size:

$$D_{50} = F\,H^{-p} h^{1-p} \left(\sigma / g\rho\right)^{p} \equiv FD^{*}, \tag{4.7}$$

where D^* can be seen as an estimate of the droplet size without the influence of the viscosity.

The median droplet sizes obtained from the weathering flume tests are summarized in Table 4.6 together with the relevant experimental variables.

Due to the limited energy available in the experimental methodology used here, we are skeptical as to the validity of some of the data from higher viscosity oils. Specifically, when the induced mean droplet size begins to decrease with increasing viscosity and yield stress, at the same time that the plunging jet is observed not to penetrate the oil layer to any significant degree, interpretation of results becomes uncertain. In such cases the assumption invoked in this study and in the earlier studies by Delvigne et al. of complete entrainment of the surface slick under the wave is clearly violated, and the data are therefore disqualified from the analysis.

The data qualified for use in the correlation are marked with colored shading in the table, while data excluded from the correlation are without shading. The disqualified data represent low quality images with few droplets, in general observed in tests with high viscosity (viscosity exceeding 5000 - 8000 cP). The results are mostly characterized by comparatively small median droplet size and diminished logarithmic standard deviation (Table 4.6). The reason appears to be that the plunging jet was unable to penetrate and break up the slick efficiently in these experiments. The resistance of the slick to breakup is not necessarily due only to high viscosity, but may be caused by other rheological properties of these samples, such as yield stress. Since high viscosities are in general correlated with high values of yield stress (see Table 4.6), the two properties can not be easily distinguished.

In the case of the wax-rich Norne crude, the median droplet size found in the experiments at 5°C is probably excessive due to precipitation and solidification of wax. This might affect the break up process, but may not necessarily be reflected in the measured bulk viscosity. For this oil, the emulsion viscosity also falls with increasing water uptake over the first two days, as is typical for wax-rich oils (refer to discussion in Section 4.2.2), whereas the mean droplet size increases. Inclusion of such "contrarian" oils in a general algorithm for entrainment will require additional work.

Table 4.6. Median droplet size data from flume experiments

	Time from start	Film thickness mm	Fall height cm	Emulsion viscosity mPas	Yield stress Pa	Emulsion density g/cm^3	Surface tension mN/m	Median diameter mm	Standard dev. log
Troll									
5°C no sun	1 hour	10	10	1510	5.6	0.992	13	0.386	0.389
	6 hours	15	20	2770	9.2	0.998	13	0.425	0.332
	1 day	15	30	3650	11.3	1.002	14	0.44	0.328
	2 days	15	30	4590	12	1.003	14	0.394	0.352
5°C w/sun	1 hour	5	10	1750	7.5	0.992	13	0.34	0.41
	6 hours	5	10	2620	8.7	1.007	13	0.443	0.4
	12 hours	5	10	5940	11	1.007	14	0.495	0.419
13°C w/sun	1 hour	15	10	43	-	0.978	13	0.577	0.37
	6 hours	15	10	1840	6.2	0.992	13	0.5	0.38
	1 day	30	10	8133	13	1.000	14	0.467	0.317
	3 days	15	10	13356	17	1.005	14	0.289	0.298
	3 days	15	20	13356	17	1.005	14	0.343	0.309
North Slope									
13°C w/sun	1 hour	4	10	56	-	0.902	22	0.329	0.322
	6 hour	7	10	1659	16.5	0.987	25	0.511	0.425
	1 day	3	20	7332	86.2	1.001	26	0.275	0.3
Norne									
5°C no sun	3 hours	3	20	4448	15	0.934	10	0.462	0.266
	1 day	3	20	564	1.9	0.98	12	0.524	0.293
13°C w/sun	6 hours	5	20	2290	*2*	0.931	10	0.251	0.428
Grane									
13°C w/sun	1 hour	7	20	3810	14.3	0.991	20	0.16	0.374
	6 hours	10	30	5280	20	1.003	20	0.203	0.387

Taking into account only the qualified data, (Table 4.6), we find that the mean value of the logarithmic standard deviation is $s = 0.38 \pm 0.04$ in $\log_{10}$ units.

With the same data set, a least mean square method has been used to determine the parameters in the proposed equation for the median droplet size (Eq. 4.7). The shape of the function F was determined from a plot of the ratio D_{50}/D^* against the viscosity group Vi. A plot of predicted vs. observed median droplet size is shown in Figure 4.25, while the correlation for the function F(Vi) is shown at Figure 4.26.

The best fit to the data was obtained with $p = 0.5$ and an exponential formula for the coefficient F; $F = C\, e^{a\,\mathrm{Vi}}$ with $C = 1.154$ and $a = 0.0253$.

With these parameters, the regression coefficient between observed and predicted data was found to be $R = 0.86$, where R is computed from $R^2 = 1 - \frac{SS_{err}}{SS_{tot}}$, where $SS_{tot} = \sum_{i=1,n} (y_i - \bar{y})^2$ and $SS_{err} = \sum_{i=1,n} (y_i - f_i)^2$. Here, the values y_i are the observed values and f_i are the predicted values.

It should be noted that the shape of the function F will govern the sensitivity of the median droplet diameter to variations in viscosity, here expressed in terms of variations in the viscosity number Vi.

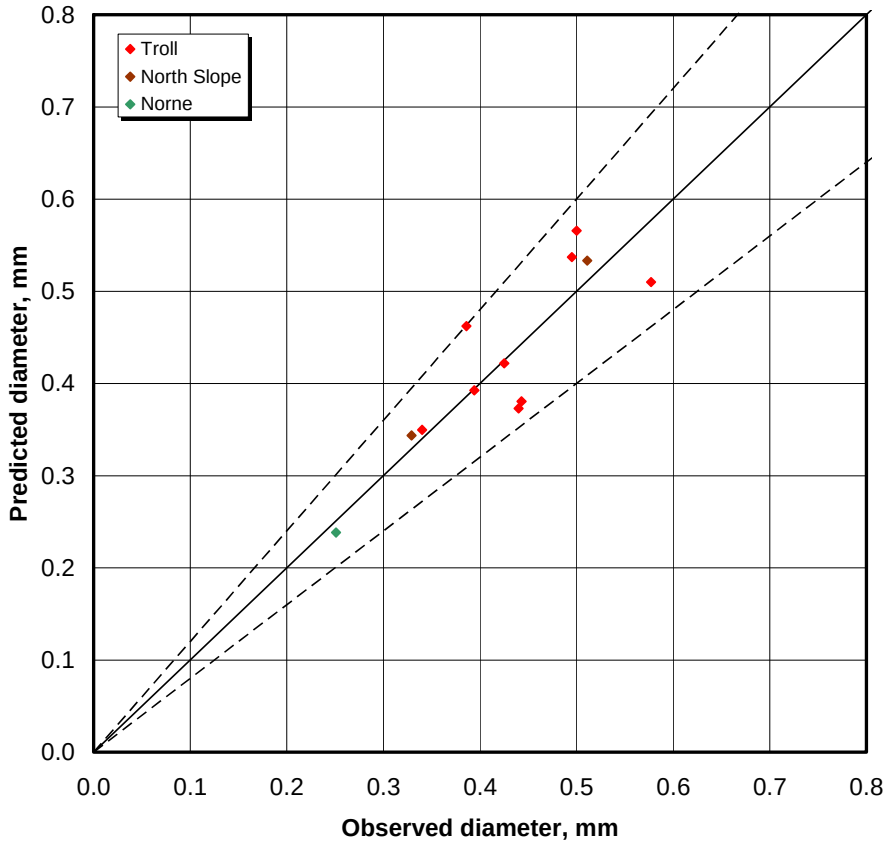

Figure 4.25. Regression plot of computed vs. observed median droplet size. The dashed lines represent +/- 20% deviations. The fit is based on a value of exponent p = 0.5. Data used in the correlation are shown with filled markers.

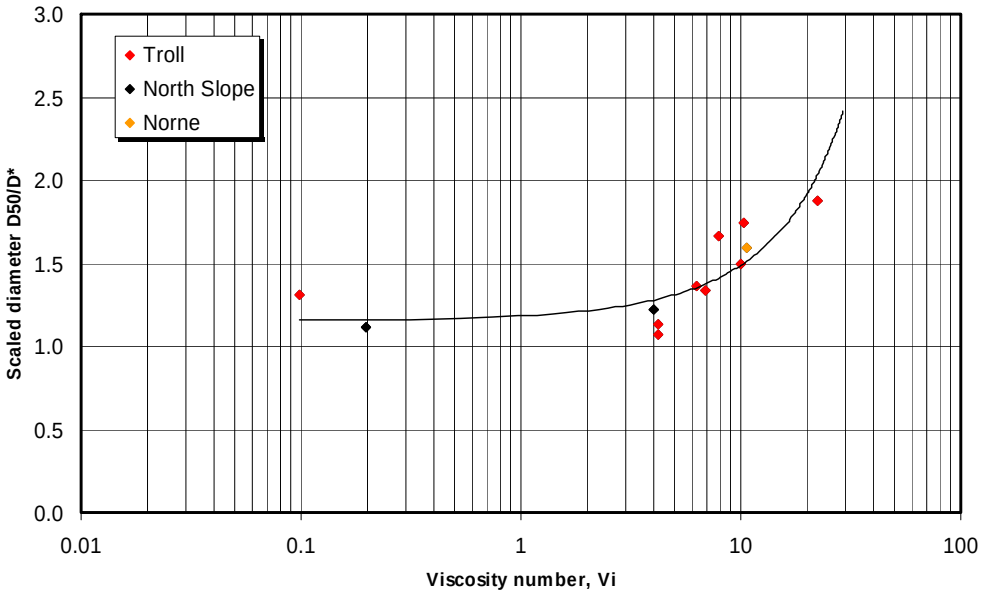

Figure 4.26. Plot of the coefficient $F = D_{50}/D^*$ versus the viscosity group Vi. The line represents an exponential function with parameters as defined in the text.

The data points together with the fitted exponential function shown in Figure 4.26 indicate that the median droplet size will increase by a factor of about 2 within the viscosity range of the qualified experimental data (i.e. from about 60 cP to about 6000 cP). This sensitivity is in fact found to be less than observed in the most recent work reported by Delvigne (Delvigne and Hulsen, 1994). A comparison of the sensitivities can be made on the basis of the plot of the dispersion coefficient (for convenience reproduced in Figure 4.27) by utilizing the expression for the maximum droplet size derived previously from Delvigne's empirical entrainment formula, as explained in the following.

In Delvigne's work, the effect of viscosity is expressed in terms of the dispersion coefficient C_o. In the equation for the maximum droplet diameter derived above, $D_{\max} = \left[\rho_o \, h / \left(C_o \, E_{bw}^{0.57}\right)\right]^{1/1.7}$, the dispersion coefficient enters into the denominator of the equation and is raised to the power 1/1.7.

Taking this into account, we have produced a plot of the viscosity factor corresponding to the reported dispersion coefficients (Figure 4.27). The viscosities are expressed in terms of the Viscosity number Vi defined previously, with an assumed oil film thickness of 0.5 mm. The film thickness was estimated from the reported amounts of oil and the water volume used in the experiments (1.5 g oil was reported to be filled on top of 0.25 L water in the beaker). The results show a considerably larger sensitivity to the viscosity number than found in the plunging jet experiments conducted in the present study (black solid line).

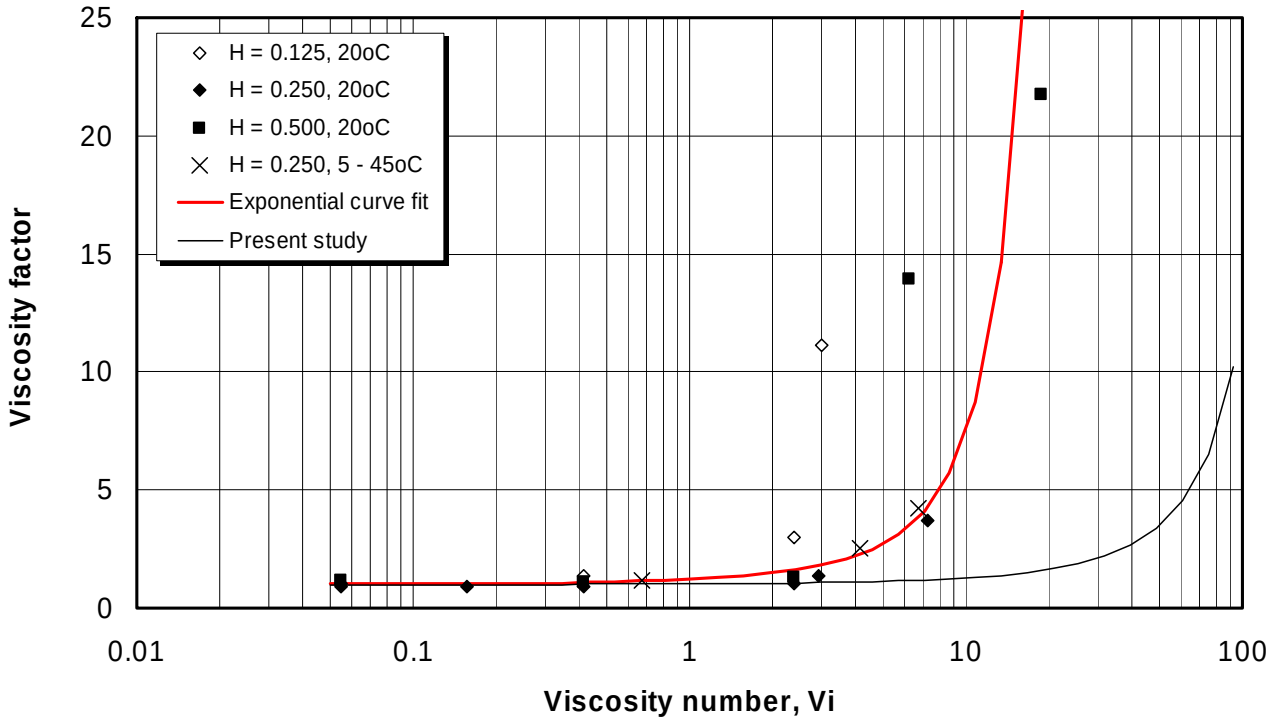

Figure 4.27. Plot of the viscosity factor as a function of viscosity number. The data points are computed from the dispersion coefficient data reported by Delvigne and Hulsen (1994) (see text for details). The red line shows an exponential curve fit to the data, while the black line shows the viscosity factor obtained from the experiments reported here.

4.4.5 Natural dispersion

In the following, we will demonstrate the effect of viscosity on natural dispersion by comparison with predictions based on SINTEF's Oil Weathering Model. We have based our calculations of the findings from the wave tank calibration experiment that show that the wave amplitude *A* (half the wave height) corresponds closely to the free fall height *H* in the entrainment experiments. Taking this into account, Equation 4.7 can be used to predict the median droplet size generated by breaking waves for given amplitude. The number distribution of the droplets by the breaking wave can then be predicted from a lognormal distribution with this median droplet size and a presumed fixed logarithmic standard deviation $s = 0.4$.

The volume distribution can be established as explained in the following:

- The volume median droplet diameter $D_{50}^{(V)}$ can be determined from the number median droplet size D_{50} by the theoretical relation mentioned previously, i.e. $m_V = m + 3s^2$, where m and m_V are natural logarithmic values corresponding to D_{50} and $D_{50}^{(V)}$, and s is the natural logarithmic standard deviation.
- This equation implies that the ratio between the volume median droplet size and number median droplet size can be expressed as $f_D = \exp(3s^2)$, where the standard deviation s is given in natural logarithmic units.
- The mean value of the logarithmic standard deviation of the number distribution reported previously ($s = 0.4$), was expressed in logarithmic units with base 10. In natural logarithmic units, this will correspond to $s = 0.92$, taking into account that $\ln(x) = \log(x)\ln(10)$. For the mean value of the standard deviation, the diameter ratio f_D will thus be 12.7.

As mentioned previously, in some models for predicting natural dispersion, a limiting droplet size $D_{\lim}$ have been introduced to obtain an estimate of the permanently dispersed volume fraction of oil that is entrained by breaking waves. The concept is based on the following major assumptions:

- The oil in the surface slick hit by the breaking wave will be completely submerged and split into droplets.
- The volume of oil entrained per unit area per breaking wave event can then be estimated as $Q_{BW} = h\, S_{bw}$, where h is the oil film thickness and S_{bw} is the white cap coverage.
- The permanently dispersed volume per unit area will then be $Q_d = P_{\lim} Q_{BW} = P_{\lim} h\, S_{bw}$, where $P_{\lim} = F_V\left[D < D_{\lim}\right]$ is the volume fraction of the entrained oil contained in droplets with diameter less than the limiting diameter.
- The permanently dispersed volume of oil per unit area and time is found by dividing by the mean wave period T_m, i.e. $\dot{Q}_d = P_{\lim} h\, S_{bw} / T_m$.
- The dissipation rate α is defined by the differential equation $dQ/dt = -\alpha Q$. Taking into account that the volume of oil per unit area equals the film thickness (assuming a homogeneous thickness and 100 % oil coverage), i.e. $Q = h$, the dissipation rate will be given as $\alpha = P_{\lim} S_{bw} / T_m$.

In addition, we may note that this implies that the fraction P_d of surface oil that will be dissipated by natural dispersion in a time interval Δt will be $P_d = 1 - \exp(-\alpha \Delta t)$, and that the fraction of the surface oil remaining from one timestep to the next will be $P_r = \exp(-\alpha \Delta t)$.

The limiting droplet size concept is obviously a strong simplification of a process that starts with entrainment of oil droplets to a certain depth in the order of the wave height, followed by resurfacing of droplets of various sizes, counteracted by vertical turbulent mixing. However, as mentioned before, the concept is widely used, and has served as a first order semi-empirical approximation with the limiting droplet size as a tuning parameter.

Presently, we will use this concept to enable a comparison of the new droplet size distribution model with a droplet size model based on the work of Delvigne. For this purpose, we have used the following formulas for the wind dependency of the sea state variables:

From Neuman and Pierson (1966):

Significant wave height (fully developed sea): $H_s = 0.021U^2$

Mean wave period (fully developed sea): $T_m = 0.81\dfrac{2\pi U}{g}$

From Monahan and O'Muircheartaigh (1980):

White cap coverage: $S_{bw} = 2.95\times10^{-5}U^{3.52}$

The required oil properties for estimation of the droplet size distributions (oil density, viscosity, film thickness etc.) were found from predictions with the SINTEF Oil Weathering Model (OWM). The predictions were made for Troll crude at 10°C sea temperature and a wind speed of 10 m/s. The relevant results are given in Table 4.7. The last two columns on the left labeled "Oil" and "Emulsion" represent the remaining oil and emulsion mass relative to the initial oil mass. As mentioned before, the SINTEF OWM is based on Delvigne's droplet size distribution model, with the limiting droplet diameter D_{lim} as a tuning factor to match observations from field experiments.

Figure 4.28 shows a comparison between predictions of the remaining oil and emulsion mass made with OWM and with the new droplet size distribution model. Three different calculations were made with different values for the coefficient a in the viscosity function $F = C\exp(a\,\mathrm{Vi})$. The three values represent respectively 1/10, 1/5 and ½ of the value $a = 0.025$ found from the correlation with the experimental data. The coefficient $C = 1.15$ was chosen according to the value found from the data correlation. The limiting droplet size was adjusted to $D_{lim} = 0.037$ mm to match the OWM-predictions with the smallest value of the coefficient a.

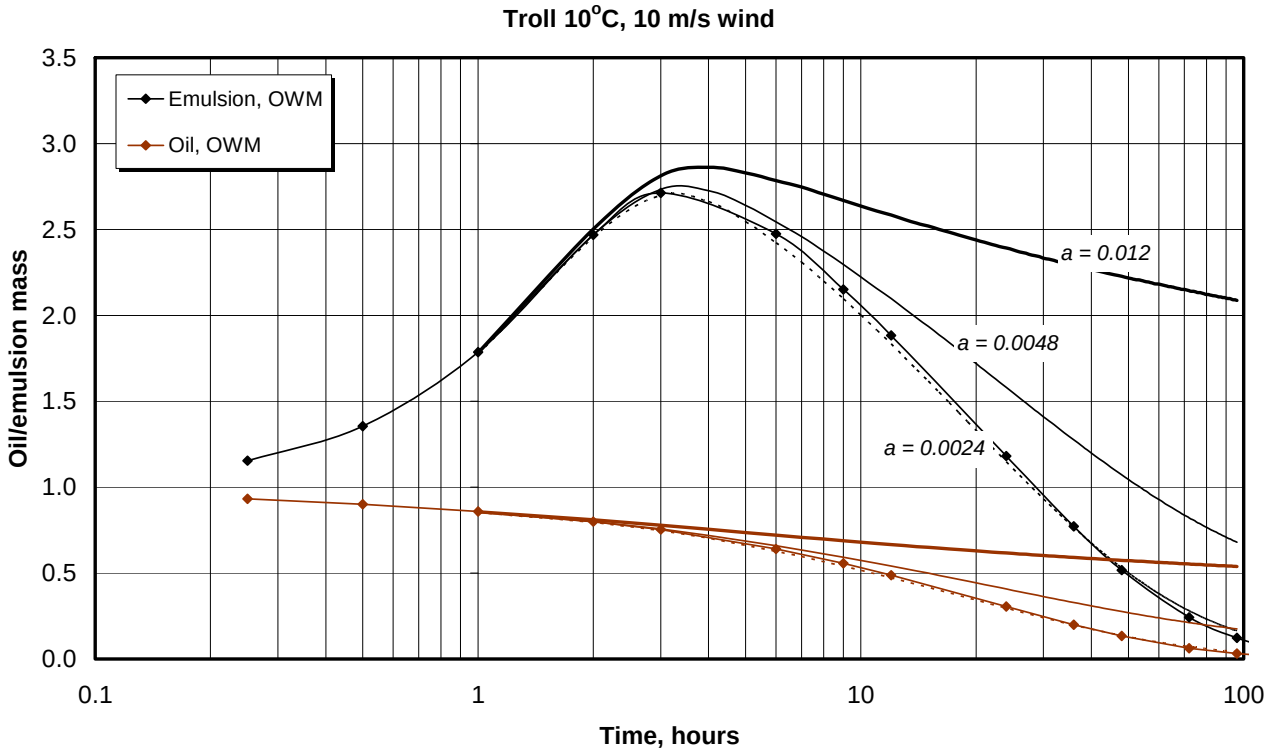

Figure 4.28. Remaining mass of oil and emulsion predicted by SINTEF OWM (lines with markers), compared with computations based on the new droplet size distribution model (unmarked lines). The different curves are computed with different coefficients in the exponential viscosity function (see text for more details).

Table 4.7. Predictions from SINTEF Oil Weathering Model for Troll crude at 10 m/s wind speed

Hours	% Evap.	% Disp	% W	Emuls. density, kg/m^3	Emuls. visc., cP	Emuls thickn., mm	Oil	Emulsion
0.25	6.0	0.8	19.3	924	95	2.249	0.932	1.155
0.5	8.2	1.7	33.5	944	203	1.967	0.901	1.355
1	10.7	3.4	51.9	968	618	1.922	0.859	1.786
2	13.7	6.3	67.6	988	2087	1.933	0.800	2.469
3	15.6	9.0	72.2	994	3474	1.777	0.754	2.712
6	18.7	17.2	74.1	997	5567	1.546	0.641	2.475
9	20.3	24.0	74.1	998	6679	1.547	0.557	2.151
12	21.3	29.9	74.1	998	7549	1.547	0.488	1.884
24	23.3	46.1	74.1	999	10257	1.547	0.306	1.181
36	24.4	55.6	74.1	1000	12586	1.547	0.200	0.772
48	25.1	61.5	74.1	1000	14822	1.547	0.134	0.517
72	25.8	67.9	74.1	1001	17429	1.547	0.063	0.243
96	25.9	70.9	74.1	1001	18209	1.547	0.032	0.124
120	26.0	72.4	74.1	1001	18780	1.547	0.016	0.062

It is interesting to note that the new droplet size distribution model can be made to match the OWM predictions by tuning the limiting diameter and adjusting the exponential coefficient in the viscosity

function. However, a complete match can only be obtained with the smallest values of the exponential coefficient *a* in the viscosity function. This is due to the fact that the OWM model has a quite limited sensitivity to variations in viscosity.

As mentioned previously, Delvigne and Sweeney originally proposed an inverse linear variation with viscosity for the viscosity related coefficient C_o, i.e. $C_o \sim \mu^{-1}$, while an exponent of -0.4 is used in the OWM model, probably to fit the low viscosity range in Delvigne and Hulsen's data, neglecting the steep decline at higher viscosities. More recently, Delft Hydraulics reports to be using the whole range of Delvigne and Hulsen's data by fitting a two equation model to the dispersion coefficient data (Delft Hydraulics, 2005). Obviously, this model will produce very limited natural dispersion after a certain time of weathering.

In total, we have found that the plunging jet method used in the present study has made it possible to significantly extend the investigated range of viscosities, compared to the studies reported earlier by Delvigne and collaborators. With droplet size data successfully obtained up to viscosities of about 5000 cP, we observed a smaller sensitivity to increasing viscosity than in Delvignes studies. The effect of viscosity on droplet size was found to be small or negligible up to viscosities in the order of 1000 – 3000 cP, followed by an apparent exponential rise in sensitivity for viscosities above this range. However, since we are on the limit of the experimental method, extrapolations based on these observations are uncertain.

5.0 Conclusions

The objective of this project has been to develop a set of algorithms for modeling natural dispersion of spilled oil at sea, with an eye towards unifying real oil-in-water dispersion (i.e. clouds of droplets being driven into the water column by breaking waves) with submergence, under a single concept. Submergence can be viewed as "dispersion of non-dispersible oil", resulting in the over-wash of near-neutrally buoyant “blobs” or "patches" or "carpets" of non-Newtonian oils such that they may be submerged for long periods of time, given sufficient surface turbulence. Such oil mats are probably subject to breakdown into tar balls, but over a time scale that is poorly known.

The methodology proposed was anticipated to carry the experimental work started by Delvigne and Sweeney (1988, 1993, 1994) into higher viscosity, non-Newtonian regions in the parameter space of the problem. Whereas Delvigne and Sweeney worked with a maximum viscosity of about 1000 cP, this study has produced data for emulsions in the 10,000 cP range. However, the energy levels available using the present methodology have been insufficient to break up higher viscosity oils and emulsions, such that data above about 10,000 cP is still lacking. In addition, none of the heavy oils studied here achieved a density greater than seawater during the 14-day weathering time period allocated for each. This has meant that we have only been partially successful in achieving the goals of the study.

Significant advances have been made to place the entrainment process on a stronger scientific footing, such that subsequent work can be focused on filling specific knowledge gaps, rather than establishing a new basis.

5.1 Long term experiments

The findings from the weathering flume experiments may be summarized as follows:

- The weathering flume tests covered a wide range in oil types, from a light oil/condensate, via medium and heavy crude oils, to heavy fuel oils. However, after 14 days exposure in the weathering flume, the residues of the various oils were found – with a few exceptions, to be quite similar in terms of density and viscosity.
- None of the tested oils reached densities exceeding the density of the sea water in the flume, so the water-in-oil emulsions were buoyant in sea water throughout the 14 day duration of the experiments.
- Exposure to artificial sunlight was found to cause a significant increase in the viscosity of water-in-oil emulsions, compared to tests without solar exposure. This effect appears to be due to changes in the chemistry of the oil caused by photo-oxidation. Evaporative losses and water uptake were found to be practically identical with and without solar exposure. Moreover, different chemical analyses which were performed to detect possible changes in the chemical makeup of the oil related to photo-oxidation did not show any significant formation of polar components or other functional groups.
- The various oil properties determined during the long term flume experiments were found to correspond satisfactorily with predicted oil properties for the whole 14 day duration. This conclusion is based on results from two of the tested oils (Norne and Troll crude), for which oil weathering predictions were available with SINTEF’s oil weathering model (SINTEF OWM).

5.2 Natural dispersion experiments

The main findings from the plunging jet experiments were as follows:

- Droplet break-up could be obtained with the plunging jet until about 2 days after start of the weathering tests, or as long the viscosity did not exceed about 10 000 mPas. In order to reach this limit, the free fall height was increased to overcome the increasing resistance to breakup caused by the increasing viscosity yield stress, and thickness of the oil layer. Above this limit, breakup could not be accomplished with any further increase in the fall height (within practical limits). For the heaviest oils used in the study, no droplet breakup data could be provided using the methodology applied here.
- The droplet size distributions obtained from the successful experiments showed in general a close fit to log-normal number distributions. The results from each test could therefore be expressed in terms of two distribution parameters, the mean logarithmic droplet diameter and the logarithmic standard deviation.
- Both parameters were found to vary within relatively narrow ranges, but trends were found in the data that indicate that the median droplet size correlates with fall height, film thickness and oil viscosity, while no clear trends were found for the logarithmic standard deviation.

The calibration study performed prior to the flume tests indicated that a one-to-one relation exists between the free fall height in the plunging jet tests and the amplitude of the breaking wave (half the wave height). The droplet size distribution data obtained from these experiments may thus be used to derive correlations for prediction of initial droplet size distributions generated in breaking wave events.

5.3 Algorithm development

An empirical correlation function has been developed to predict the droplet size distribution of entrained oil as a function of oil film thickness, wave amplitude, oil viscosity, and oil-water interfacial tension. As mentioned above, since the droplet size number distributions in general showed a close fit to log-normal number distributions, the number distribution could be characterized by two parameters, the mean logarithmic diameter and the logarithmic standard deviation. Since the latter was found to be fairly stable, an empirical correlation was developed for the mean logarithmic diameter (Eqs. 4.6 and 4.7), while a constant value was proposed for the logarithmic standard deviation ($s \approx 0.4$ in logarithmic units with base 10). This empirical correlation function differs substantially from earlier work in that it is built up from a dimensional analysis of the problem, incorporating both the Weber number and a non-dimensional viscosity group as proposed in the state-of-the-art report (Johansen, 2007).

The correlation is based on tests with oil and water-in-oil emulsions with viscosity up to about 10,000 cP, an order of magnitude higher than previous work permitted. Limitations in the experimental methodology, specifically the available energy input in relation to the viscous forces in and thickness of the high-viscosity emulsions precluded the development of data in the next higher viscosity decade. There remains therefore some uncertainty as to the best value for the coefficient a in the viscosity function. Since this coefficient appears in the exponential term, the results are relatively sensitive to this value. Wax-rich oils also remain a challenge, since precipitation and solidification of wax at low temperatures appears to affect droplet formation processes, and emulsion viscosity falls with increasing water uptake over the first few days, whereas the mean droplet size increases.

Inclusion of such “contrarian” oils in a general algorithm for entrainment will require additional work.

By combining this correlation function with equations for wave height and period as functions of wind speed and whitecap coverage, in addition to model predictions of oil weathering properties, we have demonstrated how the new droplet size distribution correlation function can by used to make predictions of natural dispersion depending of time at a given wind speed (section 4.4.5). However, this correlation function for the may be used in any oil drift or oil weathering model where the droplet size distribution of entrained oil is required.

5.4 Limitations of the study

The experimental work was carried out in an elliptical flume measuring approximately 10 m in circumference, and a little less than meter in width and depth. The weathering environment included a fan-induced wind at about 7 m/s, temperature control set at 5 or 13 degrees C for these experiments, and a breaking wave in one of the longer sides of the ellipse, with a height of 15 – 20 cm. The creation of the wave induces a circulation in the flume of about 1 round per minute. Two solar lights simulate the effect of solar radiation on the physical-chemical composition of the oil.

Clearly all of these aspects of the test environment pose potential problems when attempting to relate results to full scale events at sea. Many years of comparative studies between laboratory and field weathering results (e.g. Daling and Strøm, 1999) support the proposition that evaporation and emulsification are well reproduced in the flume environment, although the latter occurs perhaps a little more rapidly in the flume than in the real world.

Natural dispersion of oil vertically into the water column is difficult to measure in the field. In the flume, oil that is dispersed in small droplets will accumulate in the limited mixing volume available until an approximate equilibrium is reached between the continued creation of new small droplets, and the resurfacing of droplets already created. Thereafter small droplets will be created at slower and slower rates, as the surface oil viscosity increases, and the net oil remaining in the water column decreases until only the smallest droplets remain. This process is reflected nicely in the time series provided by the LISST-100X (*Figure 4.16*).

The horizontal dispersion of the oil is even more clearly limited by the test environment. After 14 days in the flume, all oil on the surface remains within the confines of the flume, whereas it would be spread over many square kilometers in the open ocean. In most of the tests the surface oil appeared as small independent globules, probably pre-cursors to eventual tar balls. These of course tended to cluster together, whereas in the ocean they would have been scattered far and wide, and would perhaps have been broken into smaller entities due to passing storms and significantly higher breaking wave energies.

In summary, the results obtained here give us some new insight into key weathering processes and rates, but the limited spatial and energetic scales of the experiments increase the uncertainty associated with application of results to full scale events.

6.0 Discussion and Importance to Oil Spill Response/Restoration

Equations were developed for droplet size distribution as a function of oil film thickness, wave amplitude, oil viscosity, and oil-water interfacial tension. Combined with equations for wave height and period as a functions of wind speed (plus fetch, dept and duration if desired), and whitecap coverage, an algorithm for natural dispersion is presented. This algorithm differs substantially from earlier work in that it is built up from a dimensional analysis of the problem, incorporating both the Weber number and non-dimensional viscosity group.

The algorithm developed here represents an improved methodology for modeling natural dispersion of spilled oil at sea. The model algorithms can be implemented in OSCAR, as well as other oil spill simulation models with applicability to spill response preparedness and decision-making, and implementation of optimum spill recovery strategies. The new algorithms will improve the understanding of transport and weathering processes, development of improved response strategies, and improved response actions in general. The results of the study will allow for improved trajectory analysis, since oil which is primarily subsurface will be driven by currents more than directly by wind. The results will therefore improve our ability to predict oil transport, a key part of response as well as the damage assessment activities.

7.0 Technology Transfer

The results of this work will be published in an international scientific journal such that other model developers may implement these new algorithms. A presentation of results has been accepted for the 2009 InterSpill Conference in Marseilles in May, 2009, and another is planned for the International Marine Environmental Modeling Seminar (IMEMS) being planned in Durham, NH in 2010.

8.0 Achievement and Dissemination

A manuscript is in preparation, although the publishing journal has not yet been selected. A paper is also in preparation for presentation at Interspill 2009 in Marseilles in May, 2009.

9.0 References

Buist, I. A. and Potter, S.G. 1987. Oil submergence: Wind/wave tank tests and modelling. AMOP Proceedings No. 10: 1-20.

CIE publication, 1989: 85 Solar spectral Irradiance - Table 4, 1989. ISBN 3 900 734 22 4

Daling, P. S., and T. Strøm, 1999. Weathering of oils at sea: model/field data comparisons. Spill Science & Technology Bulletin, Vol. 5, No. 1, pp 63 - 74,

Delft Hydraulics, 2005: Delft3D-PART, User Manual, WL|Delft Hydraulics, Delft, The Netherlands.

Delvigne, G. and C. Sweeney. 1988. Natural dispersion of oil. Oil & Chemical Pollution (4): 281-310.

Delvigne, G. 1993. Natural dispersion of oil by different sources of turbulence. Proceedings of the Sixteenth Arctic and Marine Oil Spill Program (AMOP) Technical Seminar, Calgary, Alberta, June 7-9, 1993, Ottawa, Ontario: Environment Canada. pp 415-419.

Delvigne, D.A.L. and L.J.M. Hulsen, 1994: Simplified Laboratory Measurements of Oil Dispersion Coefficient – Application in Computations of Natural Dispersion. Proceedings of the 17th Arctic and Marine Oil Spill Program (AMOP) Technical Seminar. Vancouver, British Columbia. Vol. 1, pp. 173-187

Eekhout, J., (2004): Gibrat's law for (All) Cities. The American Economic Review, Vol. 94, pp. 1429-1451.

Hinze, J.O., 1955: Fundamentals of the hydrodynamic mechanism of splitting in dispersion processes. A.I.Ch.E. Journal, Vol. 1, pp. 289-295.

Jansen, J.M.H. and H.E.M. Meijer, 1993: Droplet breakup mechanisms: Stepwise equilibrium versus transient dispersion. J. Rheology, Vol. 37, pp. 597-608.

Johansen, Ø. 1991. Numerical modelling of physical properties of weathered North Sea crude oils. DIWO-report no. 15. IKU-report 02.0786.00/15/91. Open.

Johansen, Ø. 2007: Lifetime for heavily weathered oils on the sea surface – Literature review, Coastal Oil Spills JIP. SINTEF Report No. 2, SINTEF Report F8885, 24 pp.

Lee, S.C., Mackay, D., Bonville, F., Joner, E. and Shiu, W.Y. 1989. A study of the long-term weathering of submerged and over-washed oil. AMOP Proceedings No. 12: 33-60.

Lee, S.C., Shiu, W.Y. and Mackay, D. 1990. The long-term weathering of heavy crude oils: Experimental measurements and development of models. AMOP Proceedings No. 13: 49-74

Lefebvre, A.H., 1989: Atomization and Sprays, Taylor and Francis, USA, 421 pp.

Lehr, W.J, R. Overstreet, R. Jones and G. Watabayashi, 1992. ADIOS - Automated Data Inquiry for Oil Spills, Proceedings of the fifteenth Arctic and Marine Oil Spill Program Technical Semiar, Edmonto, Alberta, pp. 31 – 45.

Li, M and C. Garrett, 1998: The relationship between oil droplet size and upper ocean turbulence, Marine Pollution Bulletin, Vol. 36, pp. 961-970.

Mackay, D., Chau, A., Clark, B., Yen, C., Parsons, J. and Ahier, B. 1986. The dispersion and submergence of oil spills. AMOP Proceedings No. 9: 101-111.

Mackay, D., Berger, D., Charles, M.E. and Ooijen, H.V. 1993. Rheological characterization of waxy crude oils for environmental purposes. AMOP Proceedings No. 16a: 85-98.

McDonagh, M, J.N. Hokstad and A.B. Nordvik. 1995. ”Standard procedure for viscosity measurement of water-in-oil emulsions”. Marine Spill Response Corporation, Washington, D.C. MRSC Technical Report Series 95-030, 36 p

Martinez-Bazan, C., J.L. Montanes and J.C. Lasheras, 2002: Statisitcal description of the bubble cloud resulting from the injection of air into a turbulent water jet. Int. J. Multiphase Flow, Vol. 28, pp. 597-615.

Mitzenmacher, M., 2003: A Brief History of Generative Models for Power Law and Lognormal Distributions. Internet Mathematics, Vol. 1, pp. 226-251.

Monahan, E.C. and I. O’Muircheartaigh, 1980: Optimal power-law description of oceanic white cap coverage dependent on wind speed. J. Physical Oceanography. Vol. 10, pp. 2094-2099.

Neuman, G. and W.J. Pierson Jr, 1966: Principles of Physical Oceanography. Prentice-Hall, p. 351.

Reed, W.J., 2001: The Pareto, Zipf and other power laws. Economics Letters, Vol. 74, pp. 15–19

Singsaas, I., Daling, P.S., and Jensen, H. 1993: Meso-scale laboratory weathering of oils. IKU Report 22.2042.00/04/93, IKU, Trondheim, Norway, 81 p.

10.0 Appendix A: Laboratory Results from the meso scale flume experiments

Table 10.1 Results from flume experiment with the Troll crude at 5°C with artificial sunlight

Sample n°	Time (Hours)	Water Content (vol%)	Evaporative Loss (vol%)	Viscosity (mPas)	Yield Stress (Pa)	Oil in Water (ppm)	Oil density (Kg/L)	Emulsion density (Kg/L)
0	0	0	0,0	113			0,900	0,900
1	0,5	64	12,0	974			0,915	0,985
2	1	71	12,4	1750	7,5		0,915	0,992
3	2	77	16,9	2230			0,920	1,001
4	4	81	54,7	3540			0,962	1,012
5	6	83	18,3	2620	8,7		0,922	1,007
6	11	83	19,6	5940	11		0,923	1,007
7	24	80	22,1	9360	3,7		0,926	1,005
8	48	77	24,0	11000			0,928	1,002
9	72	75	29,4	11000			0,934	1,001
10	168			22100	19			
11	192	80	28,3	20800			0,933	1,006
12	336	78	33,5	31600	28		0,938	1,005

Table 10.2 Results from flume experiment with the Troll crude at 5°C -no light

Sample n°	Time (Hours)	Water Content (vol%)	Evaporative Loss (vol%)	Viscosity (mPas)	Yield Stress (Pa)	Oil in Water (ppm)	Oil density (Kg/L)	Emulsion density (Kg/L)
0	0	0	0,0	113			0,900	0,900
1	1	71	12,8	1510	5,58		0,915	0,992
2	3	75	16,1	2070	8,39		0,919	0,994
3	6	79	18,1	2770	9,23		0,921	0,998
4	12	77	20,3	3330	14,84		0,924	1,003
5	24	78	22,0	3650	11,25	188	0,926	1,002
6	48	76	23,8	4590	11,98		0,928	1,003
7	72	75	25,3	6480		193	0,929	1,001
8	96	71	27,0	5840	12,63		0,931	1,001
9	144	73	27,7	6580	9,29		0,932	0,998
10	192	70	28,8	7180			0,933	1,000
11	240	69	29,7	7670	14,9	363	0,934	0,997

Table 10.3 Results from flume experiment with the Troll crude at 13°C with artificial sunlight

Sample n°	Time (Hours)	Water Content (vol%)	Evaporative Loss (vol%)	Viscosity (mPas)	Yield Stress (Pa)	Oil in Water (ppm)	Oil density (Kg/L)	Emulsion Density (Kg/L)
0	0	0	0,0	52			0,900	0,900
1	1	57,0	13,5	43		58,6	0,916	0,978
2	3	68,1	16,4	2225			0,920	0,991
3	6	68,3	19,4	1840	6,16	25,9	0,923	0,992
4	12	71,1	21,2	4593			0,925	0,995
5	24	75,0	24,2	8133			0,929	1,000
6	48	79,4	25,8	8600			0,930	1,005
7	72	79,2	26,4	13356		16,8	0,931	1,005
8	96	79,7	28,4	12036			0,934	1,006
9	144	76,9	30,3	13966	16,58	42,8	0,936	1,004
10	192	75,6	30,0	19561		24,3	0,935	1,002
11	240	72,9	31,8	15668	18,43		0,938	1,001
12	288	74,4	34,3	22987			0,942	1,003
13	336	74,6	32,9	20522	22,79	21,0	0,941	1,003

Table 10.4 Results from flume experiment with the Norne crude at 5°C with artificial sunlight

Sample n°	Time (Hours)	Water Content (vol%)	Evaporative Loss (vol%)	Viscosity (mPas)	Yield Stress (Pa)	Oil in Water (ppm)	Oil density (Kg/L)	Emulsion density (Kg/L)
0	0	0	0,0	3721			0,860	0,860
1	1	43	9,3	1640	3		0,871	0,936
2	3	40	13,1	4040	10	48,9	0,875	0,934
3	6	45	15,0	3070	11		0,877	0,943
4	12	65	17,9	2940	7		0,881	0,974
5	24	69	19,5	2810	4		0,882	0,980
6	48	76	23,0	4390	2		0,886	0,991
7	72	80	22,1	5520	30	26,3	0,886	1,002
8	96	77	24,0	7280	3		0,887	1,007
9	168	83	29,4	12490	193	10,8	0,888	1,001
10	192	82	27,5	16400	188		0,891	1,000
11	216	79	27,7	16300	191		0,892	0,996
12	240	79	28,1	17700	133		0,892	0,996
13	264	78	29,3	17600	3		0,893	0,995
14	336	75	29,9	20000	21		0,894	0,992

Table 10.5 Results from flume experiment with the Norne crude at 5°C -no sun.

Sample n°	Time (Hours)	Water Content (vol%)	Evaporative Loss (vol%)	Viscosity (mPas)	Yield Stress (Pa)	Oil in Water (ppm)	Oil density (Kg/L)	Emulsion density (Kg/L)
0	0	0	0,0	3721			0,810	0,810
1	1	12	3,7	7650	30		0,865	0,884
2	3	41	10,0	4450			0,873	0,934
3	6	52	12,2	2090	5,7		0,874	0,952
4	12	60	15,5	947			0,878	0,966
5	24	67	18,9	564	1,9	6,3	0,881	0,977
6	48	71	20,7	144	2,1		0,883	0,983
7	120	66	23,4	3580	3,0		0,886	0,977
8	168	67	25,2	3930	2,7	191	0,888	0,979
9	192			3390				

Table 10.6 Results from flume experiment with the Norne crude at 13°C with artificial sunlight

Sample n°	Time (Hours)	Water Content (vol%)	Evaporative Loss (vol%)	Viscosity (mPas)	Yield Stress (Pa)	Oil in Water (ppm)	Oil density (Kg/L)	Emulsion density (Kg/L)
0	0	0	0,0	434			0,810	0,810
1	1	49	13,0	995	2,9	12,1	0,875	0,948
2	3	56	16,4	1150	7,8		0,879	0,960
3	6	35	17,6	2290			0,881	0,931
4	12	39	19,1	1710			0,882	0,937
5	24	54	22,6	1650	3,7	14,8	0,885	0,961
6	48	79	25,1	423		141	0,887	0,995
7	72	79	27,7	1780			0,890	0,995
8	96	81	40,4	2420	1,5	154	0,904	1,001
9	144	73	31,9	2350			0,896	0,989
10	192	82	35,8	9670	0,78		0,900	1,000
11	240	82	43,0			49,4	0,906	1,003

Table 10.7 Results from flume experiment with the Grane crude at 13°C with artificial sunlight

Sample n°	Time (Hours)	Water Content (vol%)	Evaporative Loss (vol%)	Viscosity (mPas)	Yield Stress (Pa)	Oil in Water (ppm)	Oil density (kg/L)	Emulsion density (kg/L)
0	0	0	0,0	434			0,941	0,941
1	1	56	4,0	3810	14,3		0,949	0,991
2	3	69	5,1	5540	12,7	16,3	0,951	1,001
3	6	71	6,3	5280	20,0	15,0	0,953	1,003
4	12	73	7,6	9880	25,8		0,955	1,005
5	24	73	10,0	13700	36,3		0,959	1,006
6	48	71	11,2	24500	85,5	23,7	0,961	1,006
7	72	71	10,7	29600	81,8	17,4	0,940	1,000
8	96	67	12,2	35500	82,1	18,4	0,963	1,004
9	168	73	13,1	38000	160	36,3	0,964	1,008
10	192	69	13,5	42500	158	32,0	0,973	1,008
11	216	71	14,7	41600	159		0,967	1,007
12	240	71	14,7	45100			0,967	1,007
13	240	70	14,8	45300	161	83	0,967	1,007
14	264	71	17,7	48600			0,971	1,009

Table 10.8 Results from flume experiment with the North Slope crude at 13°C with artificial sunlight

Sample n°	Time (Hours)	Water Content (vol%)	Evaporative Loss (vol%)	Viscosity (mPas)	Yield Stress (Pa)	Oil in Water (ppm)	Oil density (Kg/L)	Emulsion density (Kg/L)
0	0	0,0	0,0	9			0,852	0,852
1	1	1,5	26,9	56			0,900	0,902
2	3	55,6	31,9	471			0,908	0,973
3	6	66,0	36,0	1660	16,5		0,916	0,987
4	12	71,3	39,0	3600			0,922	0,995
5	24	76,2	43,2	7330	86,2		0,927	1,001
6	48	77,1	44,9	12700			0,932	1,003
7	72	85,4	47,4	16800	253		0,936	1,011
8	96	78,1	47,1	20800	0		0,936	1,005
9	144	76,8	49,7	26400	0		0,940	1,004
10	192	78,7	49,7	29900	0		0,941	1,006
11	240	74,2	50,7	34100	478		0,943	1,003
13	336	75,5	53,5	40200	0		0,949	1,006

Table 10.9 Results from flume experiment with the IF180 at 13°C with artificial sunlight

Sample n°	Time (Hours)	Water Content (vol%)	Evaporative Loss (vol%)	Viscosity (mPas)	Yield Stress (Pa)	Oil in Water (ppm)	Oil density (Kg/L)	Emulsion density (Kg/L)
0	0	0	0,0	5500	0,14		0,932	0,932
1	1	30	29,8	9160	51,3		0,960	0,979
2	3	46	46,4	12700	73,8		0,961	0,990
3	6	53	52,6	12900	58,7		0,961	0,994
4	12	56	55,6	21300	51,6		0,962	0,996
5	24	63	63,4	28100	42,4		0,963	1,002
6	48	64	64,1	32100	38,3		0,965	1,003
7	72	69	69,0	23900	77,5	1,7	0,968	1,007
8	96	63	63,0	32200	171	3,0	0,971	1,005
9	144	63	62,5	79900	345	3,8	0,977	1,006
10	192	62	61,5	90600	206		0,978	1,006
11	240	63	63,3	118000	374		0,978	1,007
12	288	63	62,7	114000	263		0,000	1,007
13	336	64	64,2	158000	157	2,8	0,979	1,008

Table 10.10 Results from flume experiment with the IF380 at 5°C with artificial sunlight

Sample n°	Time (Hours)	Water Content (vol%)	Evaporative Loss (vol%)	Viscosity (mPas)	Yield Stress (Pa)	Oil in Water (ppm)	Oil density (Kg/L)	Emulsion density (Kg/L)
0	0	0	0,0	74000			0,963	0,963
1	1	14	0,1	54700	14	1,51	0,962	0,971
2	3	20	0,3	52400			0,963	0,975
3	6	27	0,7	55800	426		0,963	0,979
4	12							0,000
5	24	47	1,0	70700	29	1,06	0,964	0,992
6	48	53	1,8	95700			0,965	0,996
7	72	52	2,7	179000	35		0,966	0,996
8	96	59	3,6	186000	189	0,53	0,968	1,001
9	144	56	3,9	246000			0,968	0,999
10	192	54		230000	188	0,55	0,969	0,998
11	240	53		263000	115	0,59	0,970	0,999

Table 10.11 Results from flume experiment with the IF380 at 13°C with artificial sunlight

Sample n°	Time (Hours)	Water Content (vol%)	Evaporative Loss (vol%)	Viscosity (mPas)	Yield Stress (Pa)	Oil in Water (ppm)	Oil density (Kg/L)	Emulsion density (Kg/L)
				16100			0,963	0,963
1	1	21	9,3	18800	2,7	2,63	0,964	0,976
2	3	41	13,1	25300			0,964	0,989
3	6	51	15,0	37400	31	1,65	0,966	0,996
4	12	54	17,9	43500			0,967	0,998
5	24	63	19,5	63600	41	1,89	0,967	1,003
6	48	64	23,0	77900	7	1,81	0,968	1,004
7	72	63	24,3	120700	13	1,58	0,969	1,004
8	96	66	25,3	117000	0,13	1,47	0,970	1,005
x	144		25,9	116000				
9	192	66	27,5	110000	70		0,970	1,006
10	240	62	27,7	144000	102		0,971	1,004
11	288	65	28,1	153000	24	1,00	0,971	1,006

10.1 Results from the meso scale flume experiments - figures

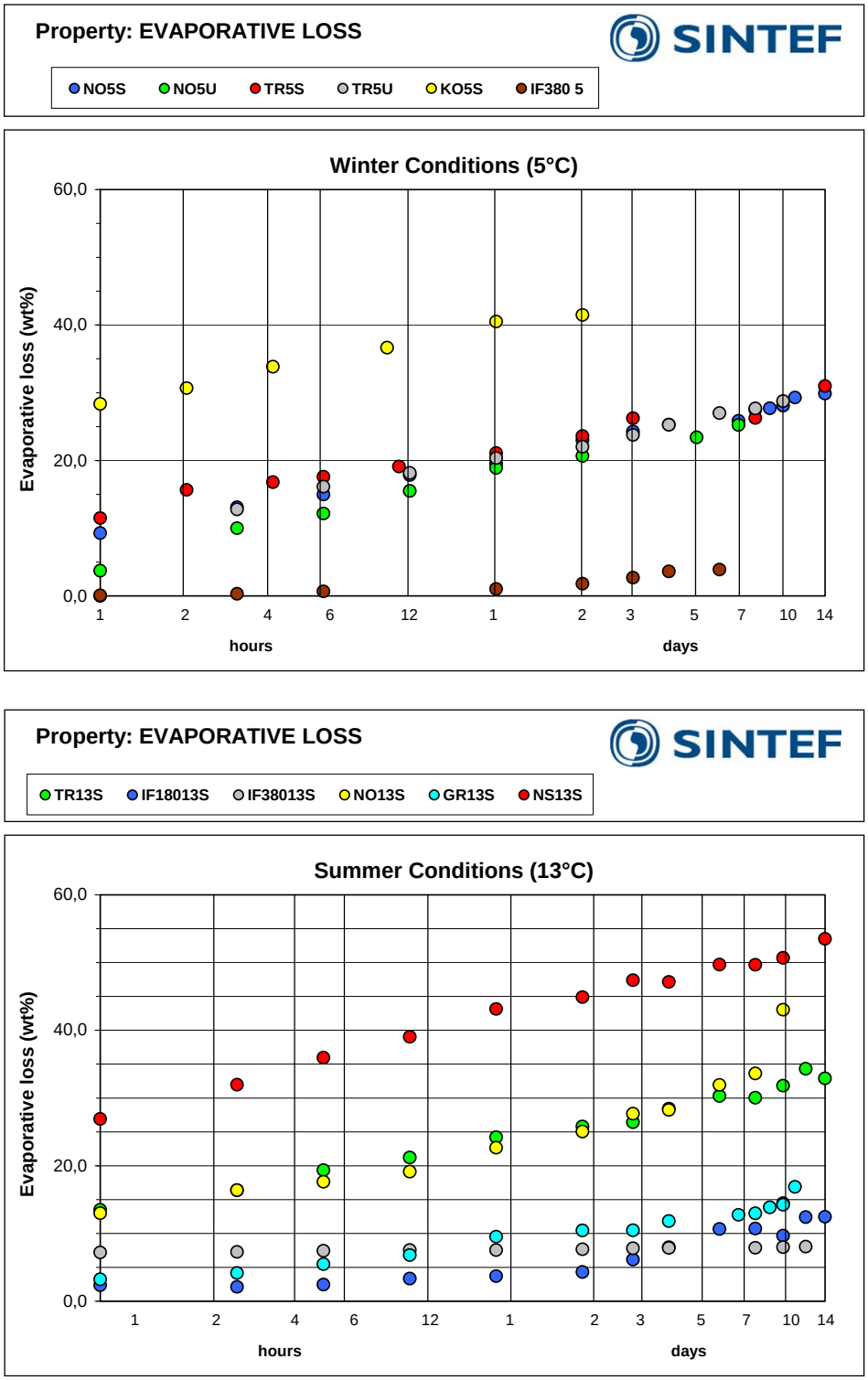

Figure 10.1 Measured evaporative loss for all experiments (5°C above, 13°C below)

NO-Norne, TR-Troll, KO-Kobbe, GR-Grane, NS-North Slope
Numbers indicate temperature, S-Solar simulator, U-No Sunlight

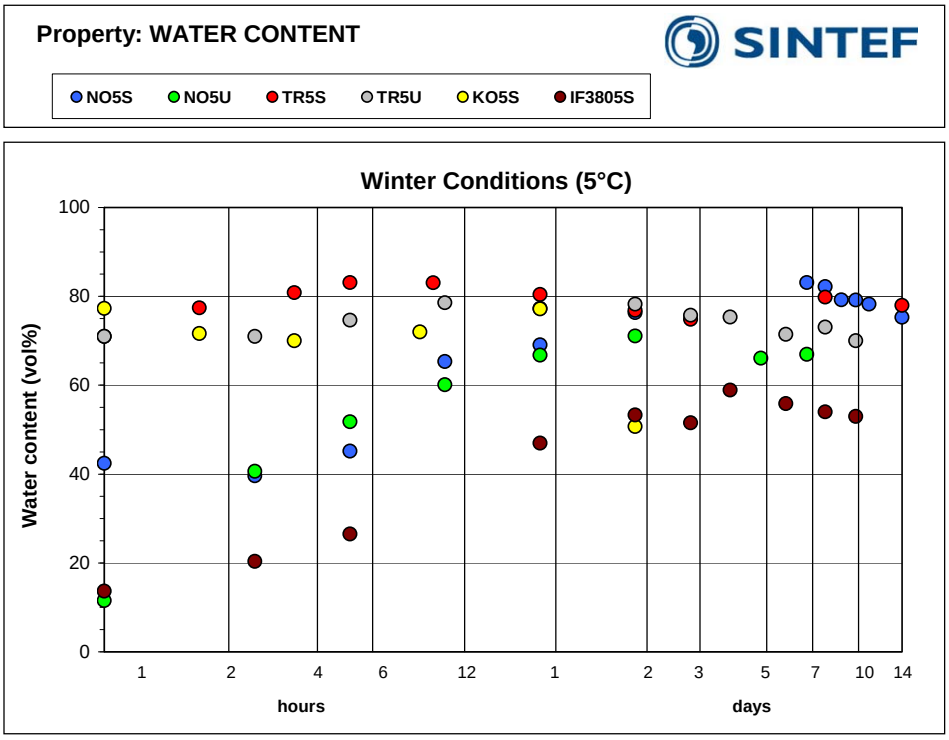

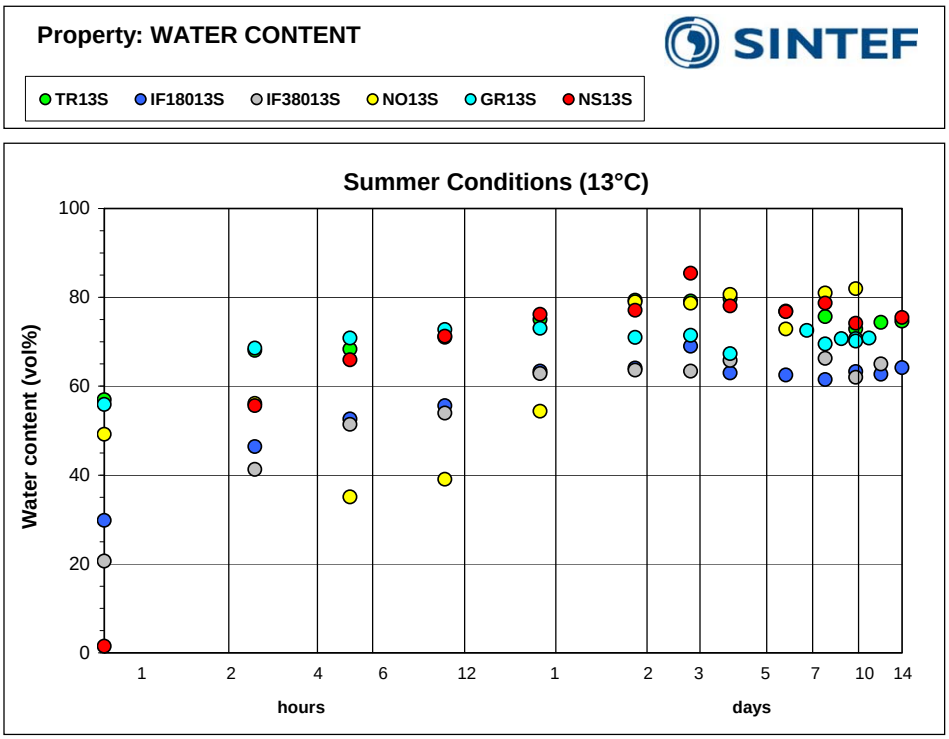

Figure 10.2 Measured water content for all experiments (5°C above, 13°C below)

NO-Norne, TR-Troll, KO-Kobbe, GR-Grane, NS-North Slope
Numbers indicate temperature, S-Solar simulator, U-No Sunlight

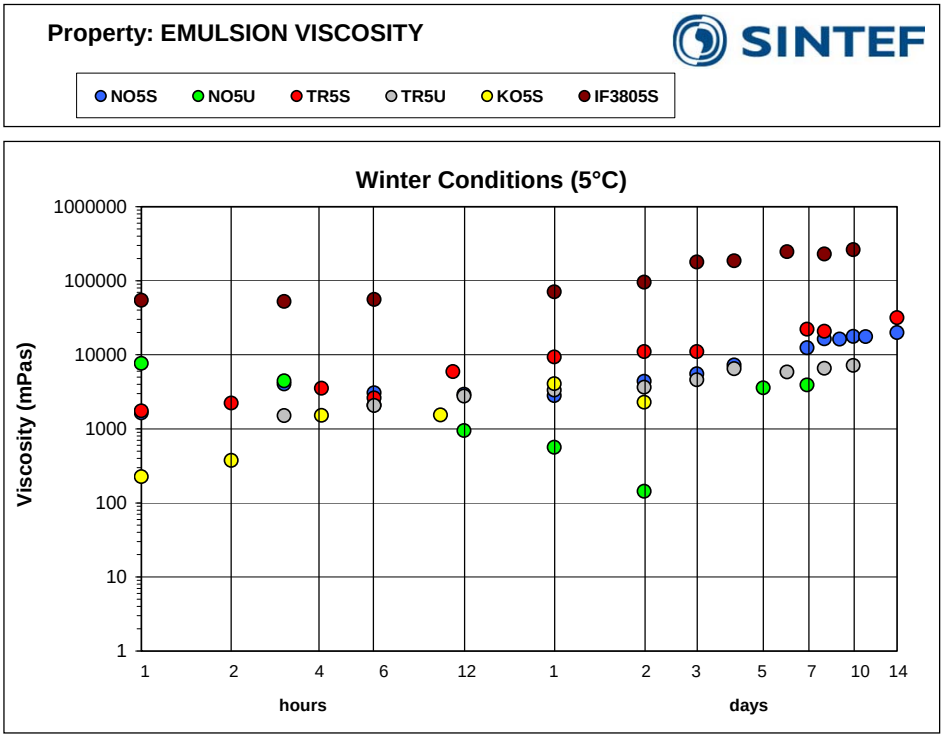

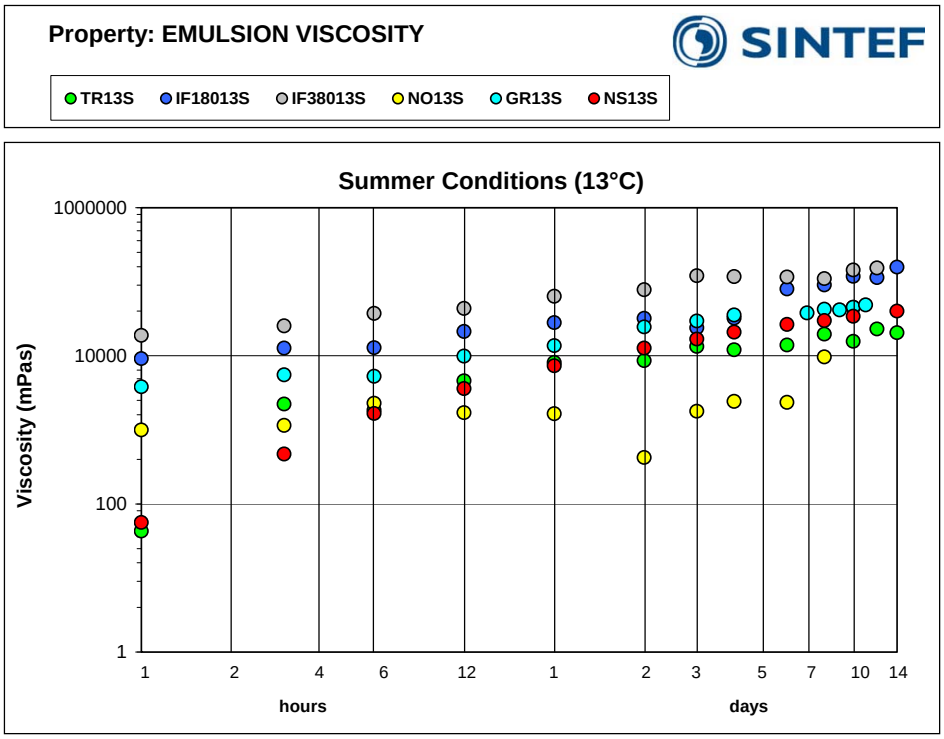

Figure 10.3 Measured emulsion viscosity for all experiments (5°C above, 13°C below). Viscosity is reported at shear rate $10s^{-1}$.

NO-Norne, TR-Troll, KO-Kobbe, GR-Grane, NS-North Slope
Numbers indicate temperature, S-Solar simulator, U-No Sunlight

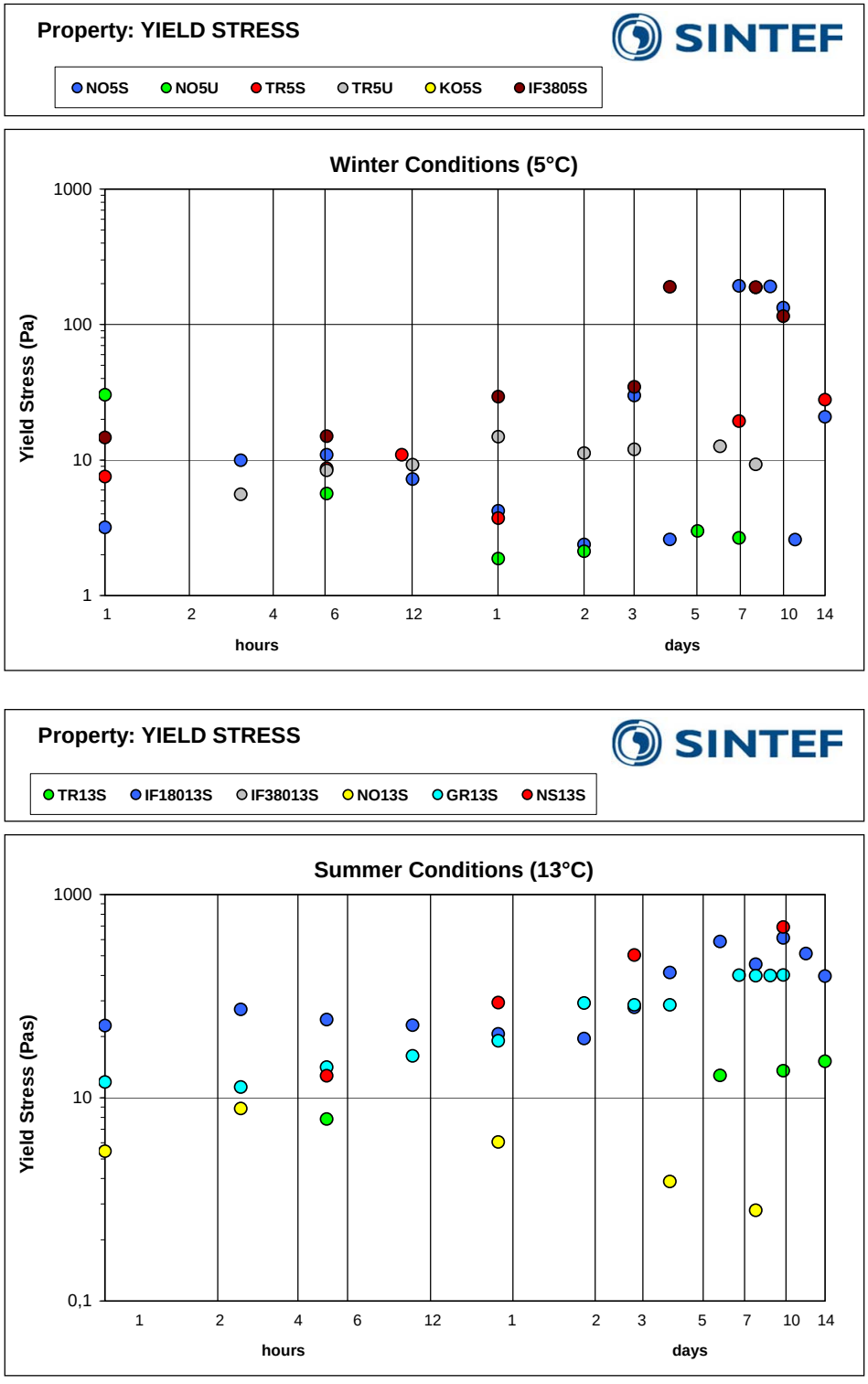

Figure 10.4 Measured yield stress for all experiments (5°C above, 13°C below)

NO-Norne, TR-Troll, KO-Kobbe, GR-Grane, NS-North Slope
Numbers indicate temperature, S-Solar simulator, U-No Sunlight

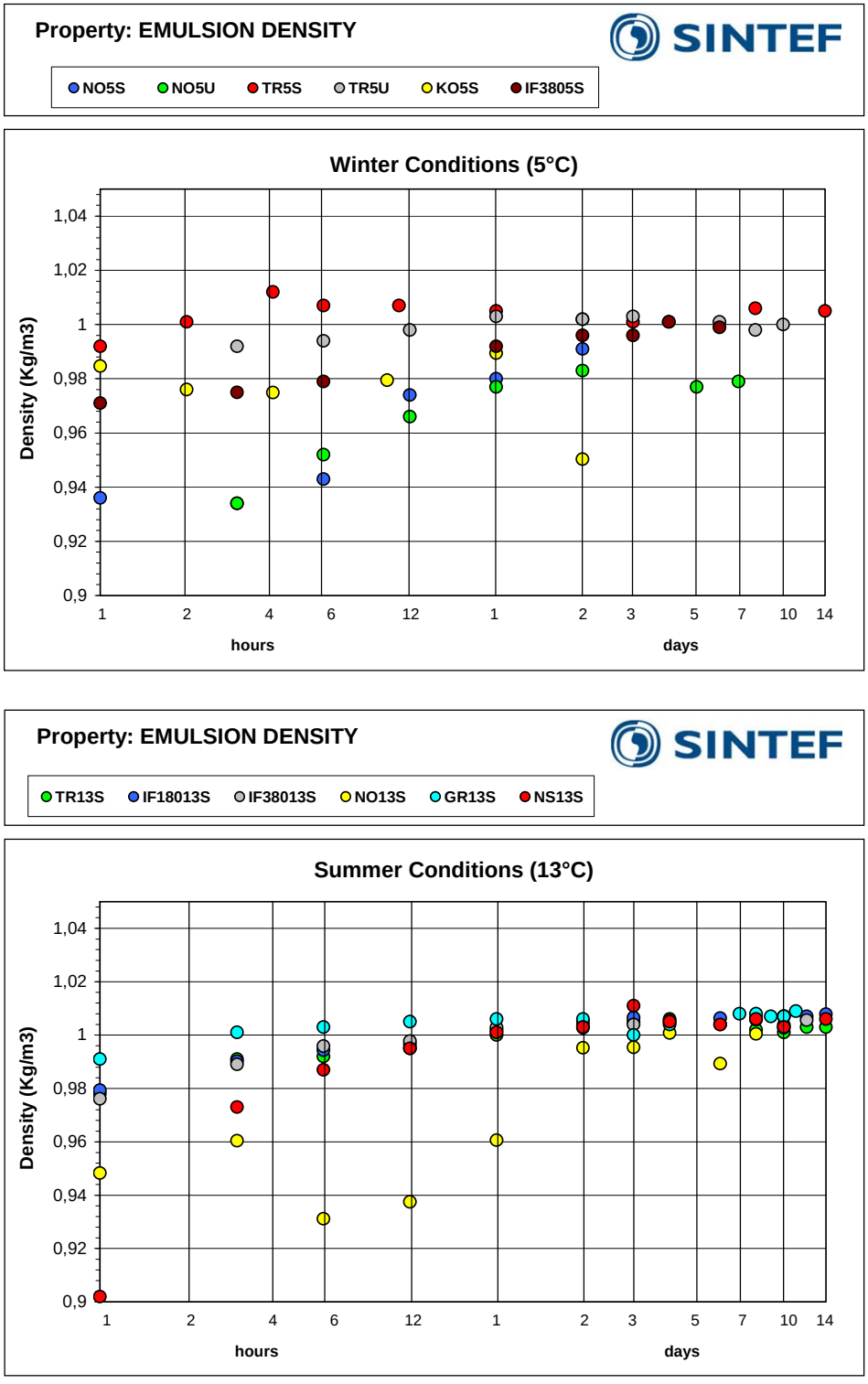

Figure 10.5 Measured emulsion density for all experiments (5°C above, 13°C below)

NO-Norne, TR-Troll, KO-Kobbe, GR-Grane, NS-North Slope
Numbers indicate temperature, S-Solar simulator, U-No Sunlight

10.2 Results compared to predictions from the SINTEF OWM

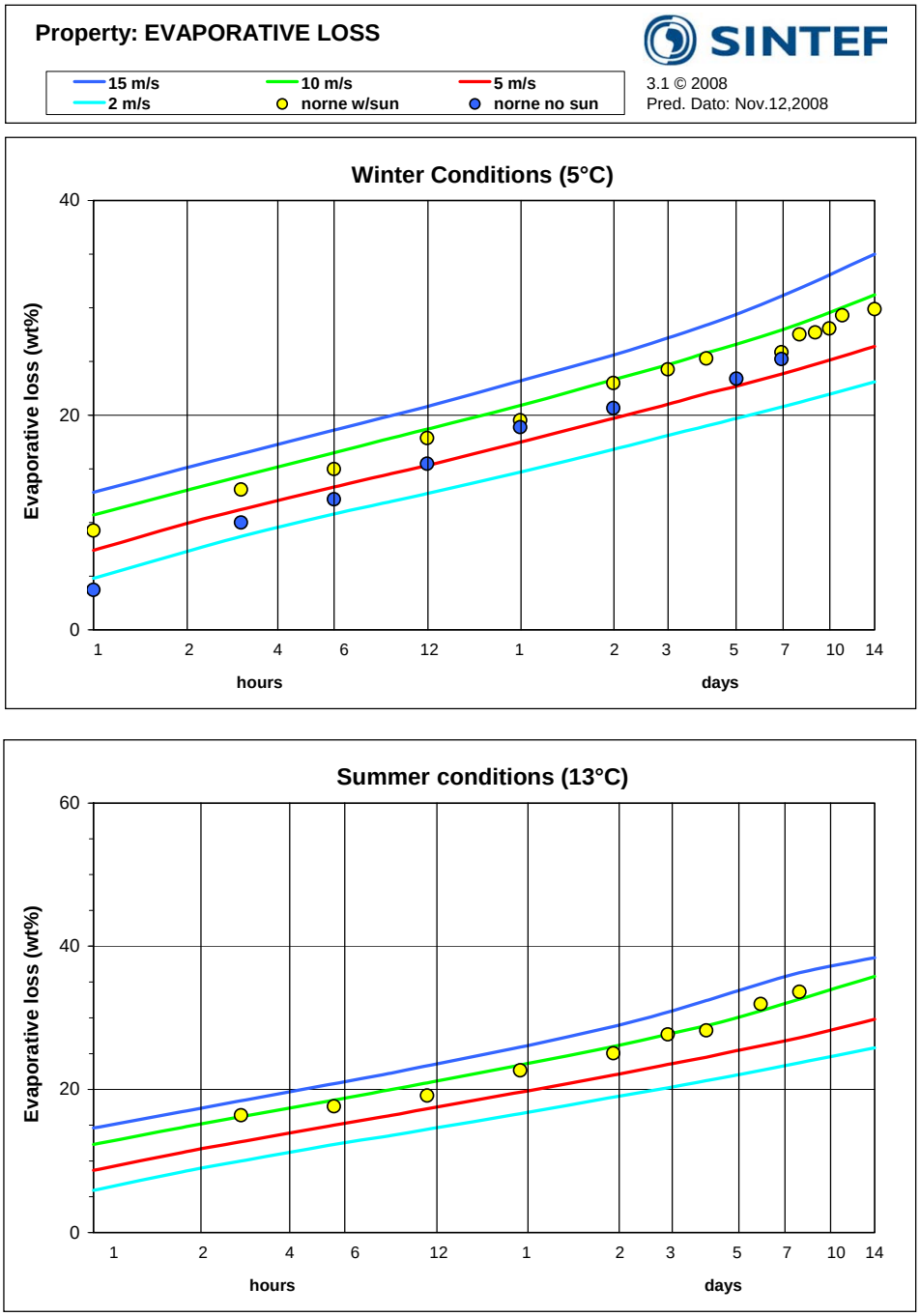

Figure 10.6 Measured evaporative loss for the Norne experiments compared to predictions from the SINTEF OWM.

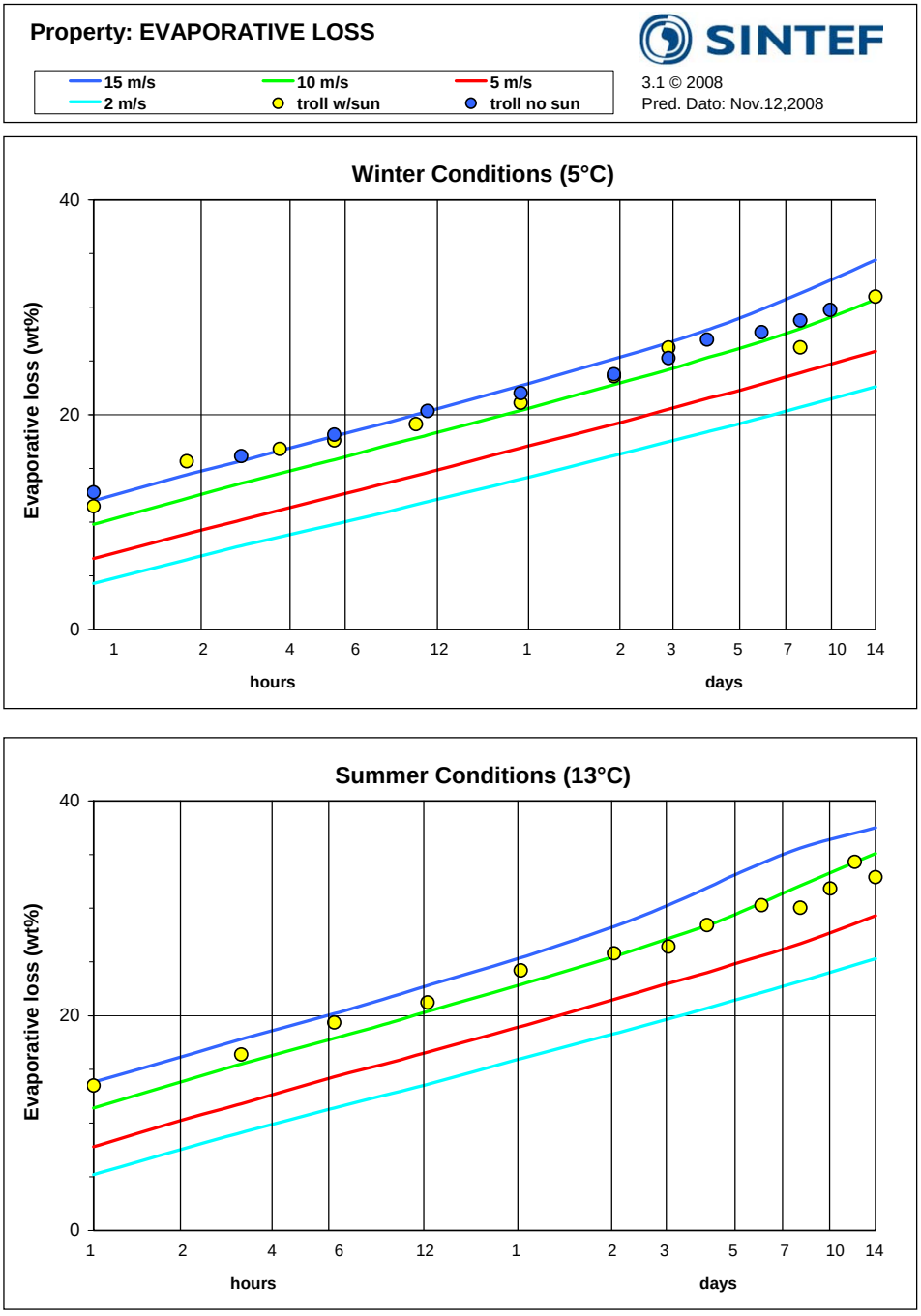

Figure 10.7 Measured evaporative loss for the Troll experiments compared to predictions from the SINTEF OWM.

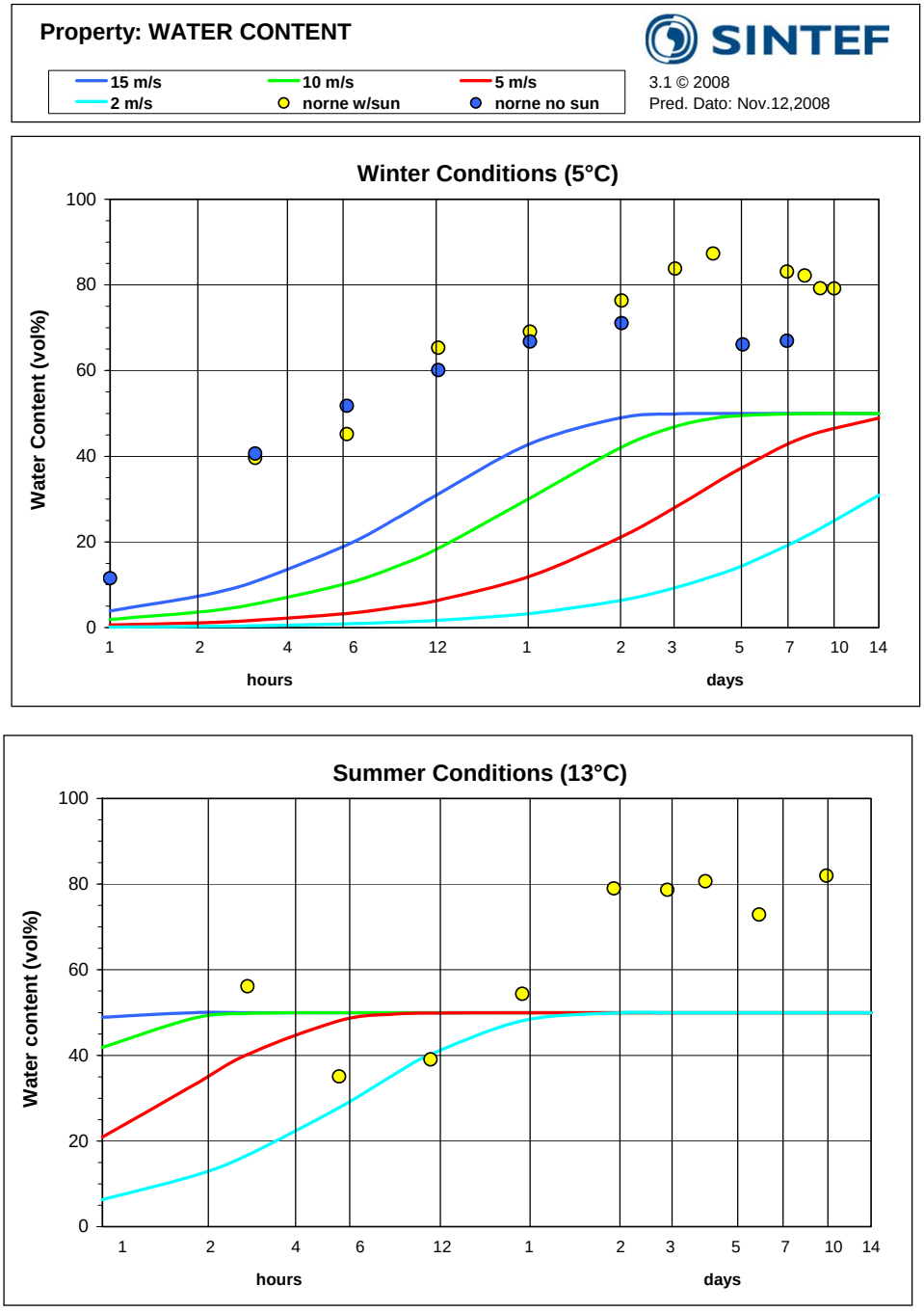

Figure 10.8 Measured water content for the Norne experiments compared to predictions from the SINTEF OWM.

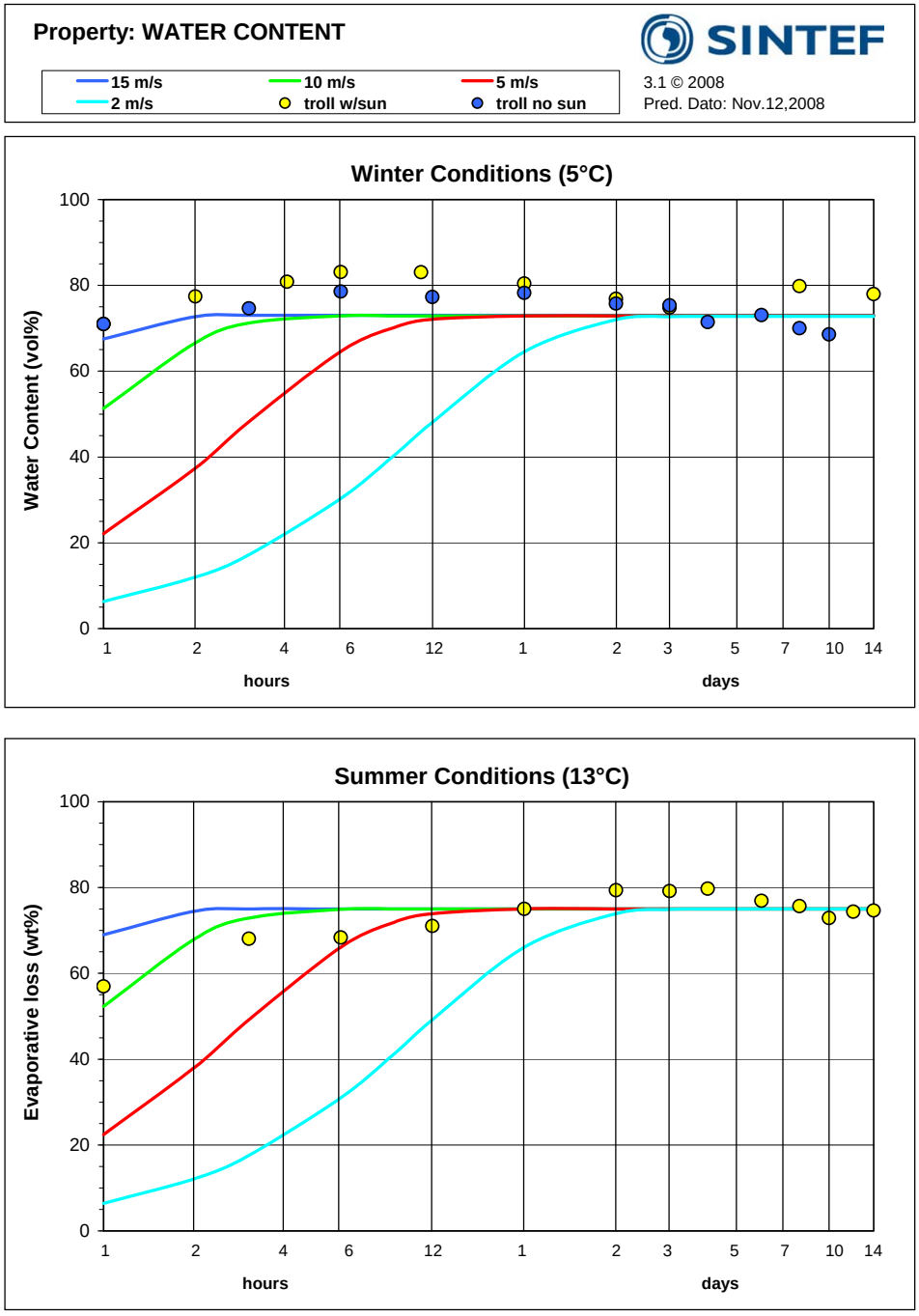

Figure 10.9 Measured water content for the Troll experiments compared to predictions from the SINTEF OWM.

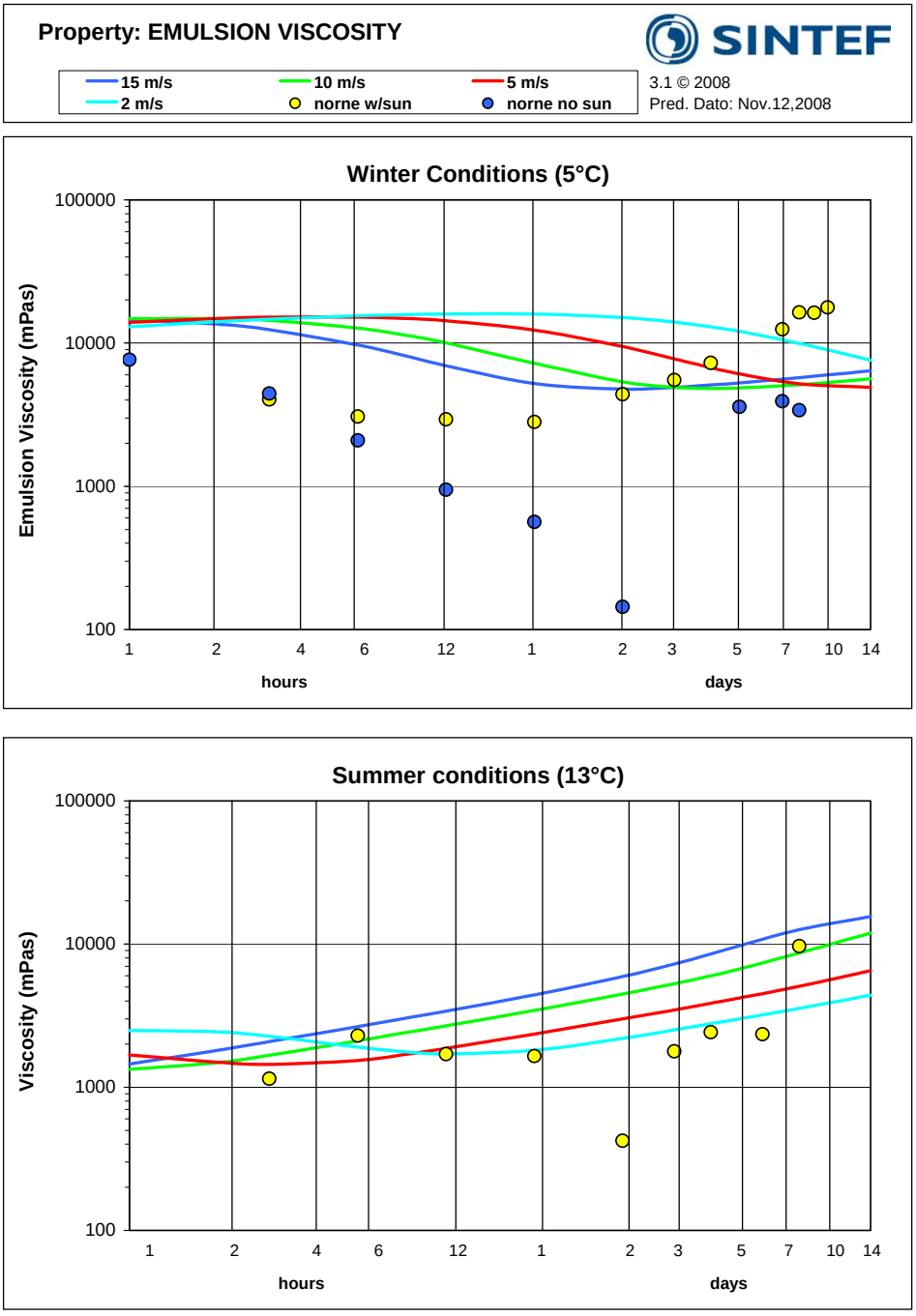

Figure 10.10 Measured emulsion viscosity for the Norne experiments compared to predictions from the SINTEF OWM. Viscosities are reported at shear rate $10s^{-1}$.

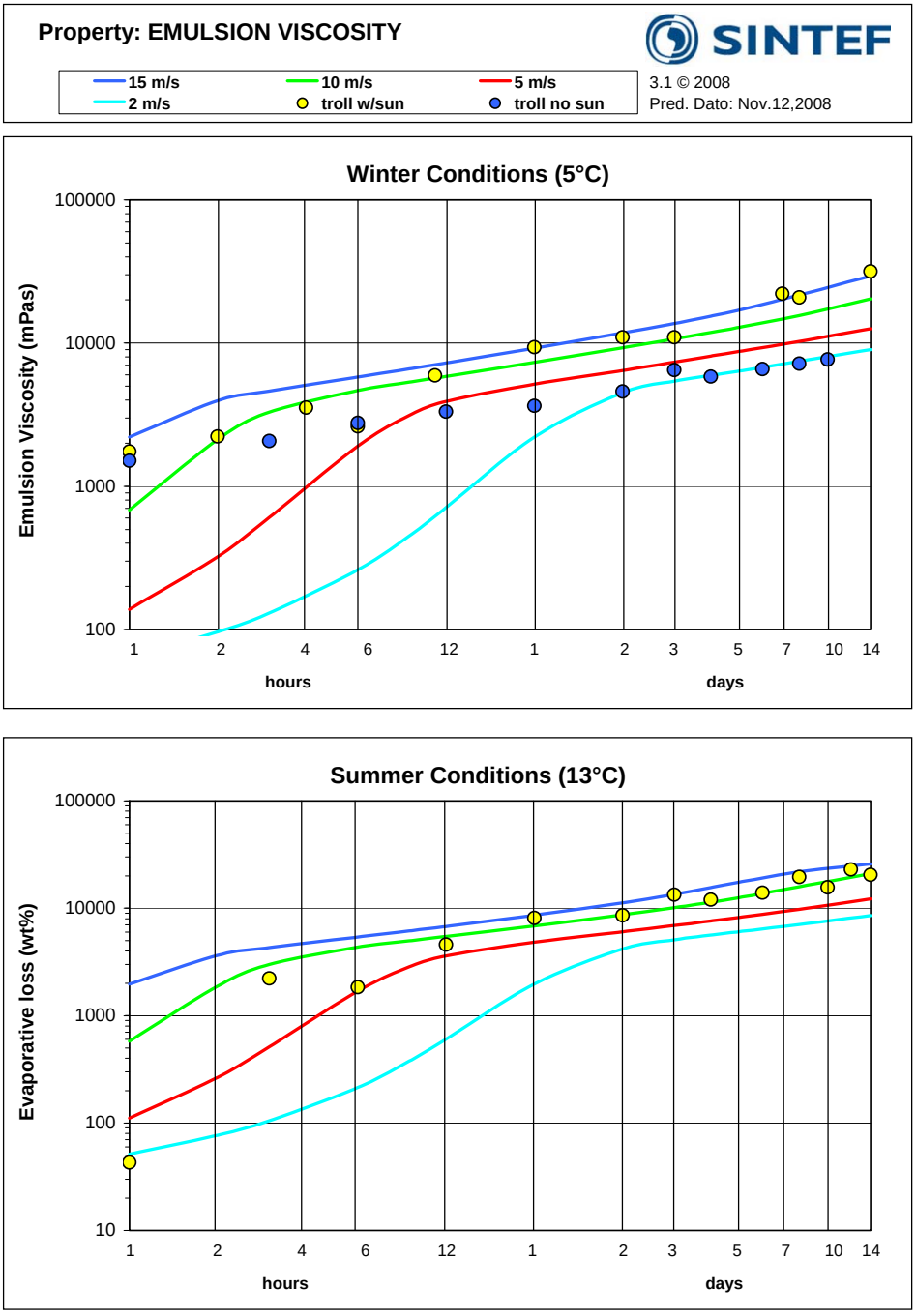

Figure 10.11 Measured emulsion viscosity for the Troll experiments compared to predictions from the SINTEF OWM. Viscosities are reported at shear rate $10s^{-1}$.

10.3 Chemical analysis – SARA, FT-IR and chromatograms

Table 10.12 Results from the SARA analysis performed on a selection of samples from the meso scale flume experiments

		Sat.	Aro.	Resins	Asph.	Tot. HC	Tot. pol.
		(wt%)	(wt%)	(wt%)	(wt%)	(wt%)	(wt%)
Troll 5°C with sunlight	1 hour	45,3	51,3	3,34	0,04	96,6	3,38
	1 day	46,7	47,3	5,81	0,14	94,1	5,95
	8 days	46,5	48,1	5,18	0,25	94,6	5,43
	14 days	50,0	44,7	5,13	0,22	94,7	5,35
Troll 5°C No sun	1 hour	47,2	48,5	4,01	0,30	95,7	4,32
	1 day	45,8	50,2	3,75	0,25	96,0	4,00
	8 days	42,1	54,3	3,59	0,10	96,3	3,69
Troll 13°C With sunlight	1 hour	37,6	55,8	5,88	0,77	93,4	6,65
	1 day	38,9	53,7	6,95	0,43	92,6	7,38
	8 days	37,0	57,5	4,87	0,67	94,5	5,54
	14 days	35,2	59,0	5,09	0,81	94,1	5,90
Norne 5°C With sunlight	1 hour	66,8	31,7	1,44	0,05	98,5	1,49
	1 day	59,1	38,8	2,04	0,04	97,9	2,08
	8 days	64,4	32,7	2,74	0,09	97,2	2,83
	14 days	61,1	35,2	3,63	0,17	96,2	3,79
Norne 5°C No sun	1 hour	65,7	32,7	1,61	0,03	98,4	1,65
	1 day	60,6	37,5	1,65	0,20	98,2	1,85
	8days	56,7	41,6	1,65	0,05	98,3	1,70
Norne 13°C With sunlight	1 hour	61,2	37,2	1,48	0,06	98,5	1,54
	1 day	59,8	38,4	1,68	0,11	98,2	1,79
	7 days	64,0	33,2	2,58	0,25	97,2	2,83
	14 days	67,4	27,7	4,80	0,14	95,1	4,94

Table 10.13 Results from FT-IR analysis - Ration of carbonyl and aromatic bands to aliphatic C-H bands

		C=O (1735) / C-H	C=O (1710) / C-H	ar (1600) / C-H
Norne 13°C with sun	1 hour			0,023
	1 day			0,011
	7 days		0,015	0,033
	14 days		0,022	0,031
	1 hour			0,028
Norne 5°C with sun	1 day			0,014
	8 days		0,008	0,016
	14 days		0,008	0,016
Norne 5°C no sun	1 hour			0,021
	1 day			0,015
	8 days			0,024
Troll 5°C with sun	1 hour	0,023	0,023	0,031
	1 day	0,042	0,034	0,038
	8 days	0,04	0,027	0,027
	14 days	0,028	0,028	0,028
Troll 5°C no sun	1 hour		0,031	0,042
	1 day		0,02	0,04
	8 days		0,026	0,046

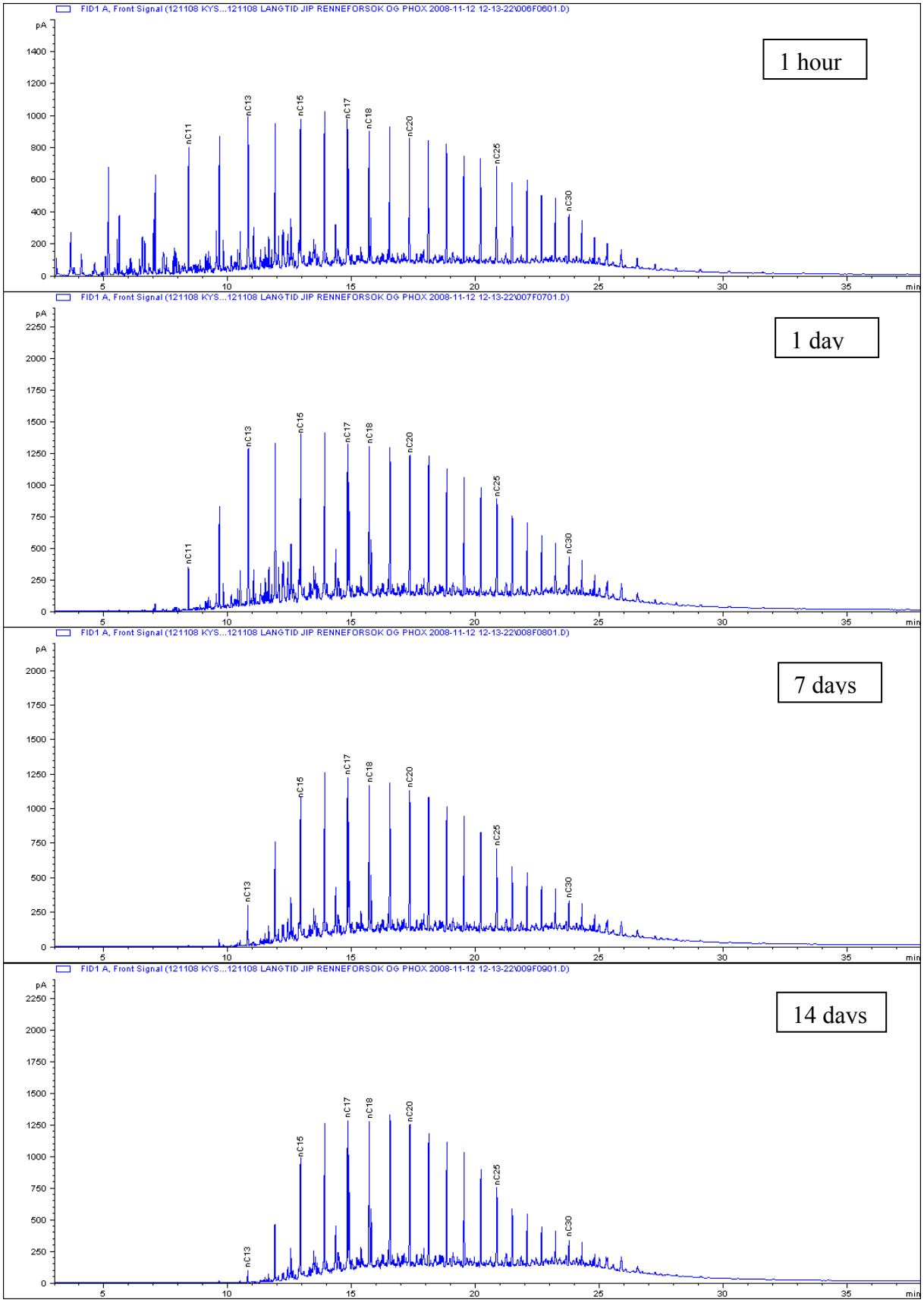

Figure 10.12 Chromatograms from the flume experiment with Norne at 13°C and artificial sunlight

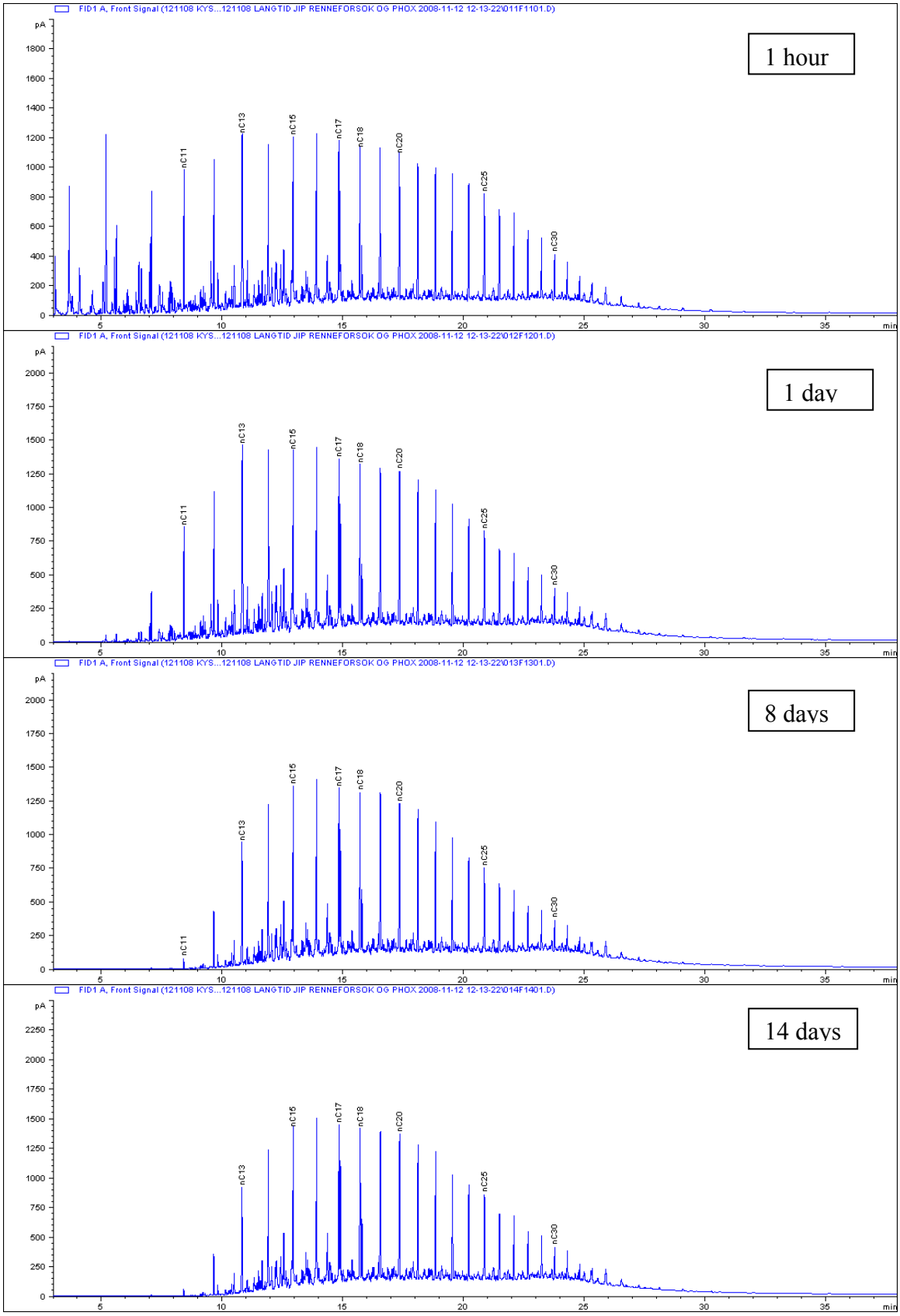

Figure 10.13 Chromatograms from the flume experiment with Norne at 5°C and artificial sunlight

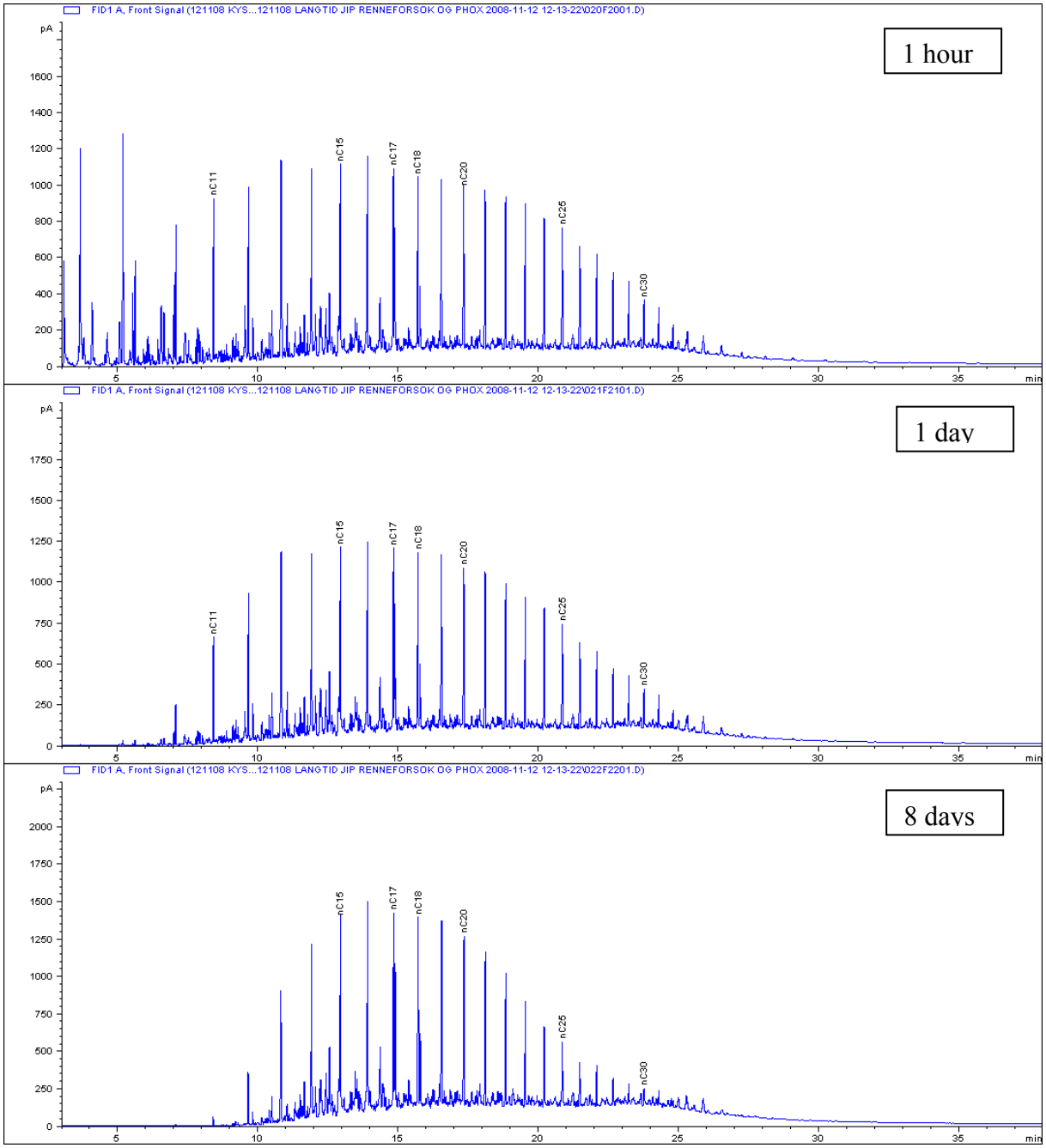

Figure 10.14 Chromatograms from the flume experiment with Norne at 5°C and no sun

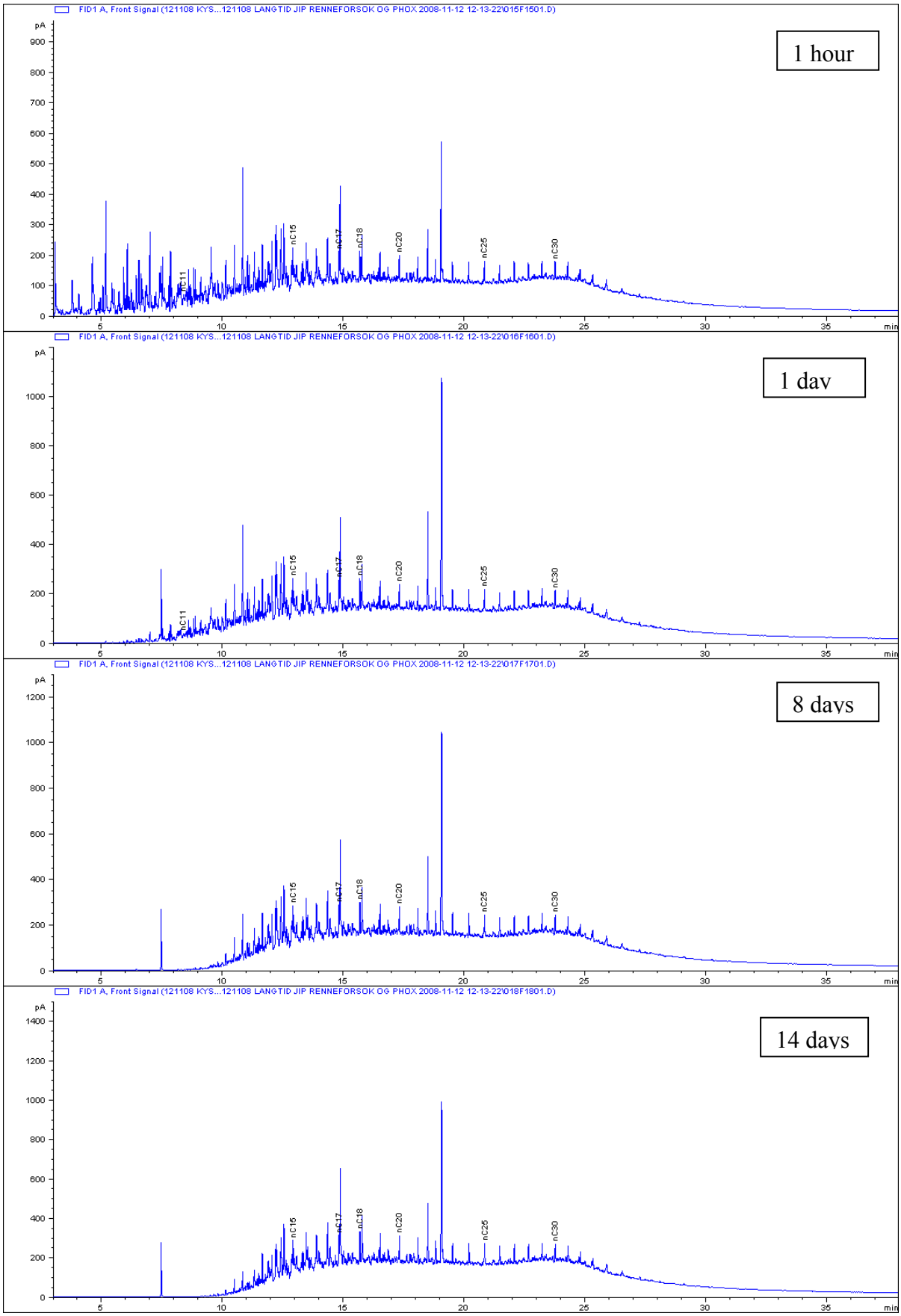

Figure 10.15 Chromatograms from the flume experiment with Troll at 5°C and artificial sunlight

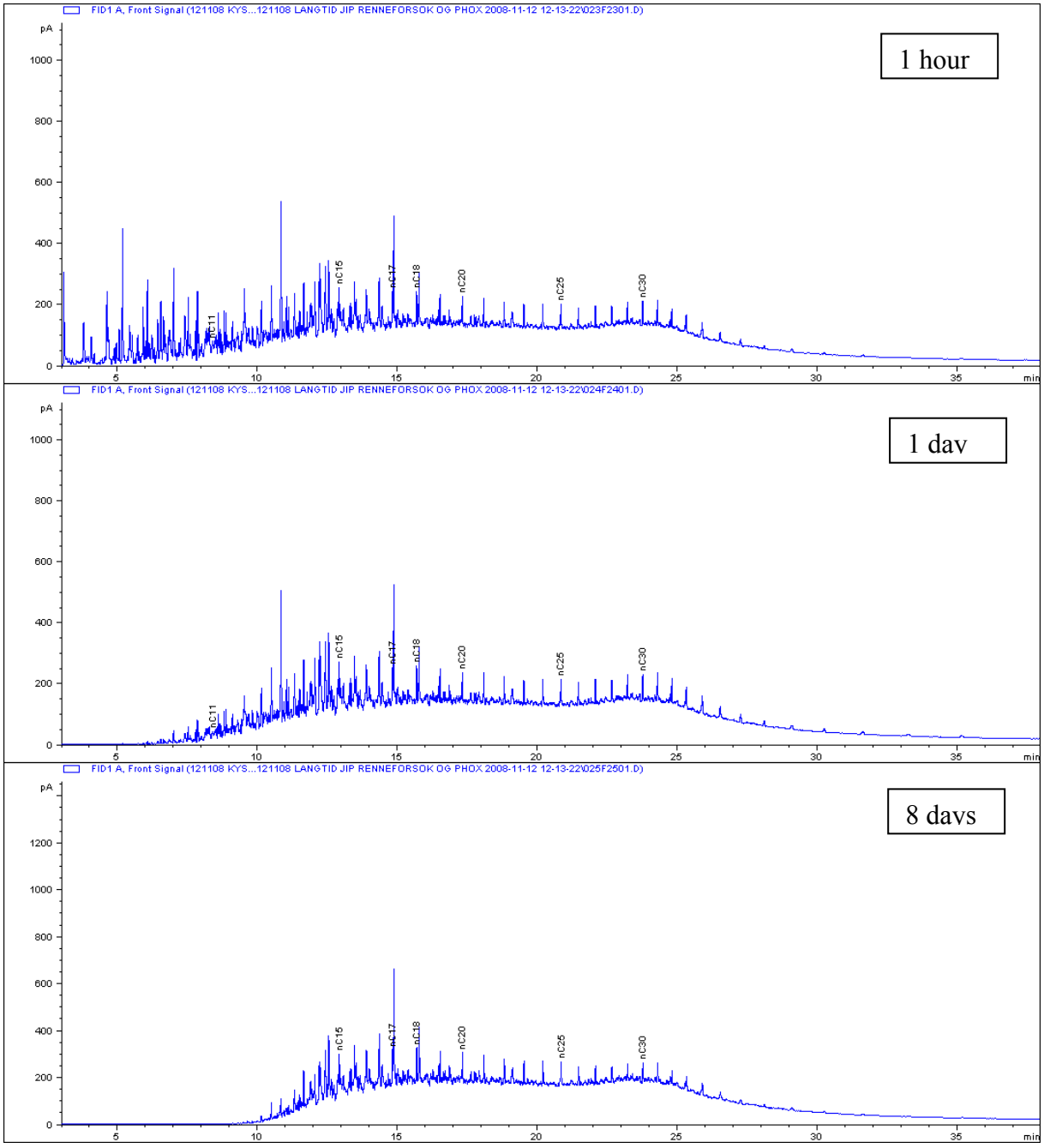

Figure 10.16 Chromatograms from the flume experiment with Troll at 5°C and no sun

10.4 Images from the flume experiments

3 hours

1 day

3 days

14 days

Figure 10.17 Images at various times in the flume experiment with Troll at 5°C and artificial sunlight.

3 hours

1 day

7 days

Figure 10.18 Images at various times in the flume experiment with Troll at 5°C and no sunlight.

3 hours

1 day

8 days

14 days

Figure 10.19 Images at various times in the flume experiment with Troll at 13°C and artificial sunlight.

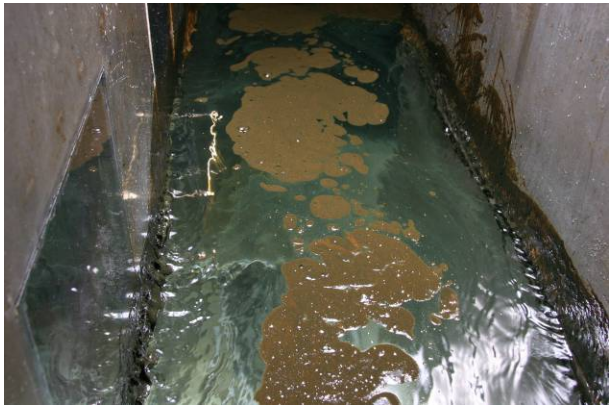

3 hours

1 day

7 days

14 days

Figure 10.20 Images at various times in the flume experiment with Norne at 5°C and artificial sunlight.

3 hours

1 day

7 days

Figure 10.21 Images at various times in the flume experiment with Norne at 5°C and no sunlight.

3 hours

1 day

7 days

14 days

Figure 10.22 Images at various times in the flume experiment with Norne at 13°C and artificial sunlight.

Kobbe 5° with solar simulation

3 hours

1 day

7 days (wax scraped off tank walls)

Figure 10.23 Images at various times in the flume experiment with Kobbe at 5°C and artificial sunlight.

1 hour

1 day

7 days

14 days

Figure 10.24 Images at various times in the flume experiment with IF 380 at 13°C and artificial sunlight.

3 hours

1 day

7 days

11 days

Figure 10.25 Images at various times in the flume experiment with Grane at 13°C and artificial sunlight.

IF 180 13° with solar simulation

3 hours

1 day

8 days

Figure 10.26 Images at various times in the flume experiment with IF180 at 13°C and artificial sunlight.

3 hours

1 day

7 days

13 days

Figure 10.27 Images at various times in the flume experiment with North Slope at 13°C and artificial sunlight.

11.0 Appendix B: Numerical Modeling of Floating Lumps

11.1 Background

Weathered oils spilled at sea of emulsified oil have been observed to submerge below the sea surface during periods of high winds and large waves. A series of weathering studies with heavy crude and petroleum products in the SINTEF weathering flume did not produce any sign of sinking oil after up to two weeks of weathering. It was therefore of interest to investigate the possibility for transient over-washing in higher energy wave environments. Some numerical tests were therefore performed to identify possible mechanisms that could explain such behavior.

11.2 Numerical model and setup

The computations were made with Flow-3D. It is a general purpose computational fluid dynamics (CFD) model based on the volume of fluid method (Hirt and Nichols). It is fully three-dimensional, and has the possibility of a free surface and wave boundary conditions. The oil lumps were modeled with Flow-3D's general moving object (GMO) model.

The GMO requires that the moving objects are resolved by the grid, meaning that the grid cells have to be smaller than the moving object (probably 4-5 cells across the GMO at least). At the same time, when predicting a situation with waves, the computational domain should be at least a couple of wavelengths long. A realistic "ocean" situation with D = 5 cm lumps in swell with wavelength and L = 50 m (L/D = 1000) would require > $5 \cdot 10^3$ cells along the wave. Another > $2 \cdot 10^2$ cells would be needed in the vertical, bringing the total number of cells to ~ 10^6 for a two-dimensional situation. A three-dimensional simulation would probably be prohibitive in terms of memory size and computing time.

In order to be able to run the simulations in a reasonable time on a powerful PC, wavelength was chosen to be L ~ 6 m and the lump diameter D = 0.2 m. These kinds of waves are likely to form at short wind duration and/or short fetch situations.

11.3 Simulations

Initial tests with the numerical model showed that single lumps moved in the waves as though they were a part of the wave (see Figure 11.1.), following the water surface orbital motion and drifting slowly in the wave direction (Stokes drift). Even with density only 1 % less than water they would float, and did not get submerged at any time during the wave cycle.

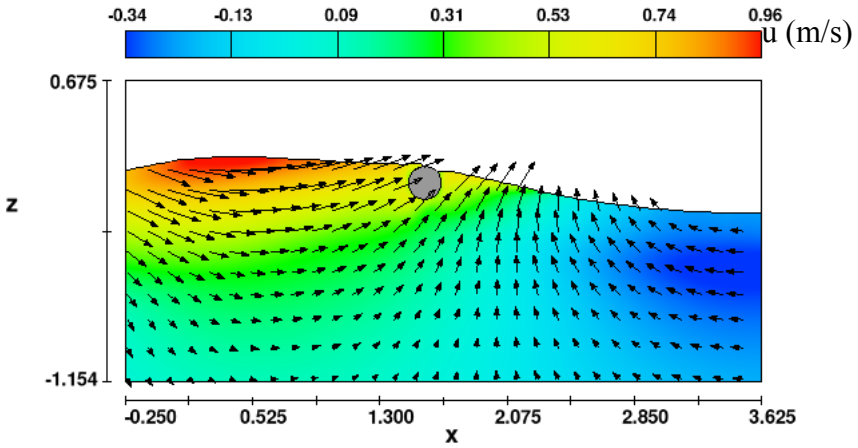

Figure 11.1 Snapshot from single lump simulation. The colour shows x-component of velocity.

A downward-directed impulse seems to be needed in order to send a lump downwards into the water column. It is imaginable that collisions between lumps can provide enough momentum to send some of them downwards every now and then. This idea was tested with a triple lump setup in steep but non-breaking waves in Subsection 11.4.

Submerging of lumps is probably most likely to happen when the vertical orbital velocity is largest, at the wave crest, particularly if the wave is breaking. A lump free-falling from the crest, or being hit by free-falling water from the crest, is likely to get submerged.

Unfortunately, it was not possible to produce a breaking wave in the numerical wave tank with the Flow-3D version and time available. (A newer version has the possibility of superimposing several waves and thereby promote wave-breaking). Therefore, this concept was tested by simulating a tank with still water (with high spatial resolution) where a lump (or water) was dropped from a height above the surface. This represents in a simplified manner what could happen at a breaking wave crest.

11.4 Lumps in waves

A 20 m long and 4 m deep "numerical wave tank" was set up for this test. The mesh was refined to $\Delta x = \Delta y = \Delta z = 0.05$ m for the upper part of the water column in a "test" section in the middle (between $x = -1.4$ and $x = 4.1$ m). The left boundary was set up so as to produce a regular sinusoidal wave with amplitude $a = 0.2$ m and period $T = 2$ s. This proved to produce a wave with length $L \sim 6$ m. Three spherical $D = 0.2$ m lumps with density 2 % less than the water was placed on the left side of the test section, with their tops flush with the water surface and a horizontal spacing (between their centers) of 0.25 m as shown in Figure 11.2.

Except for some over-washing water when the first wave hits, the lumps follow the water surface. There is an accordion effect, with the lumps being drawn apart from each other whilst going back in the wave troughs and brought together whilst being pushed forward by the advancing crests. Collisions take place, but the hits seem to be directed parallel to the water surface and only seem to influence the horizontal positions.

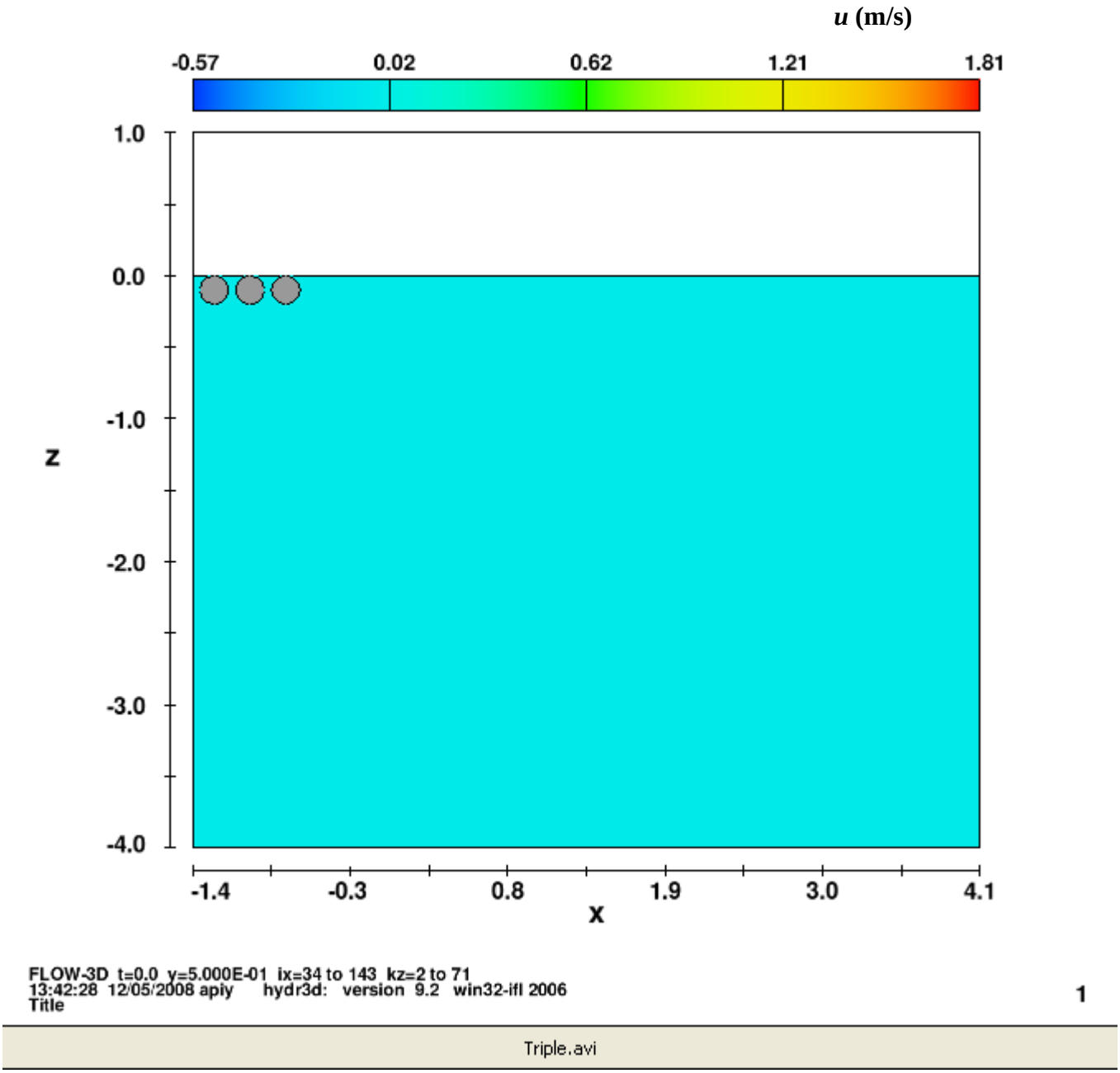

Figure 11.2Initial position of oil lumps in wave simulation. Colour denotes x-component of velocity. Double-click figure for animation.

11.5 Free-falling lumps

A 0.6m by 0.6 m "tank" with a water depth of 2 m was set up for this numerical experiment. The resolution of the mesh is relatively high, with a cell size of $\Delta x = \Delta y = \Delta z = 0.025$ m. The initial condition is a spherical $D = 0.2$ m lump lifted to a height h above the water surface as shown in Figure 11.3 (it can be double-clicked to show an animation of the simulation).

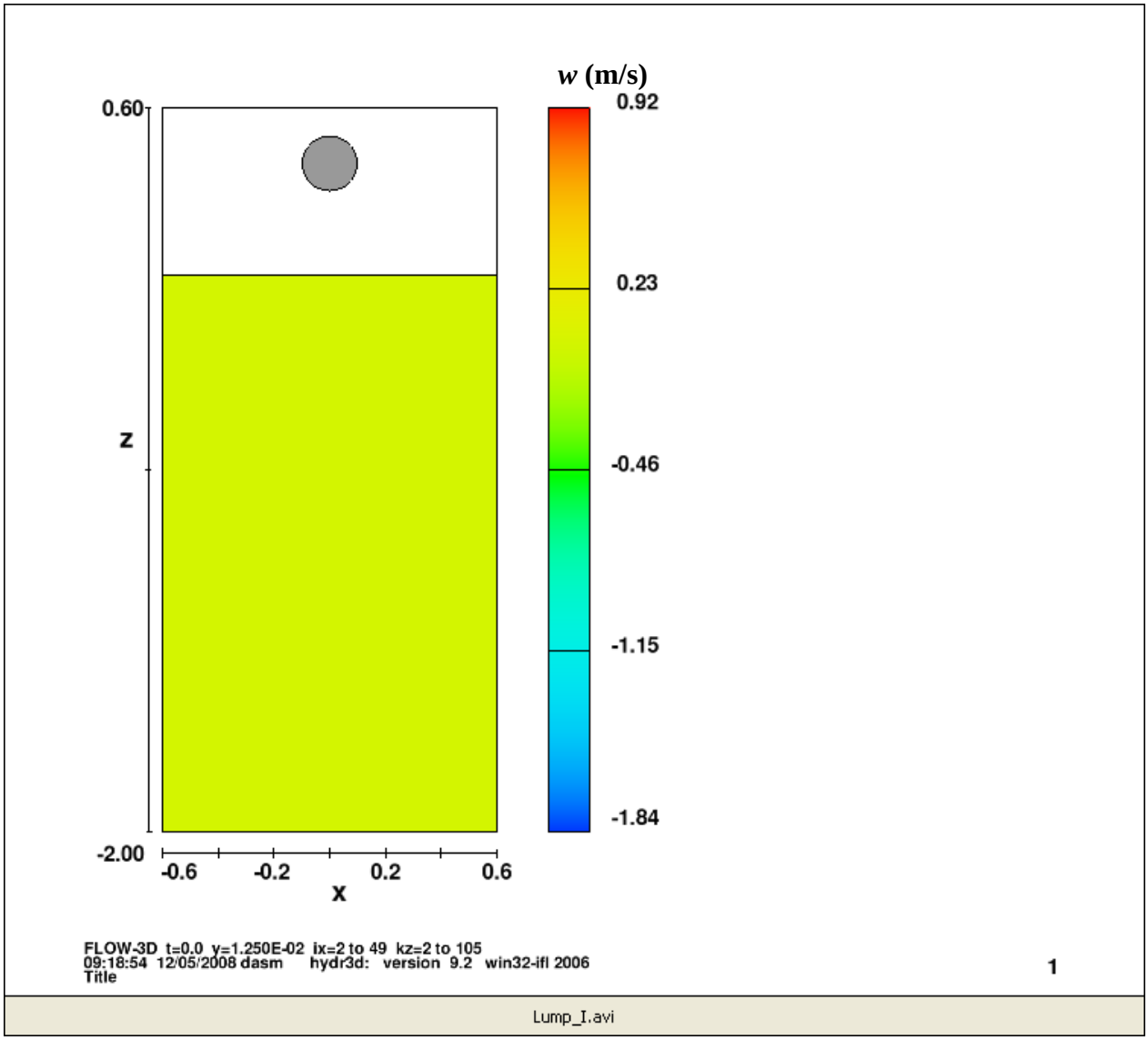

Figure 11.3Initial position and animation of free-falling oil lump simulation. Colour denotes z-component of velocity. Case: D = 0.2 m, h = 0.4 m, ρ = 984 kg/m^3, ρ_w =1025 kg/m^3 (density of lump 4 % less than water). Double-click figure for animation.

Snapshots from a simulation with a fall height of h = 0.4 m is shown Figure 11.4. One second after the drop, the lump has reached a depth of $z \sim 0.9$ m and is moving downwards with a velocity of 0.9 m/s. At t = 3 s it has reached its maximum depth of z = 1.59 m and has just started to move upwards. (It also moves a little sideways, probably due to vortex shedding.) At t = 5 s it is seen to be rising through the remnants of its own wake, and at t = 7 s it appears to be reaching its terminal rise velocity (of about 0.5 m/s) shortly before breaking the surface.

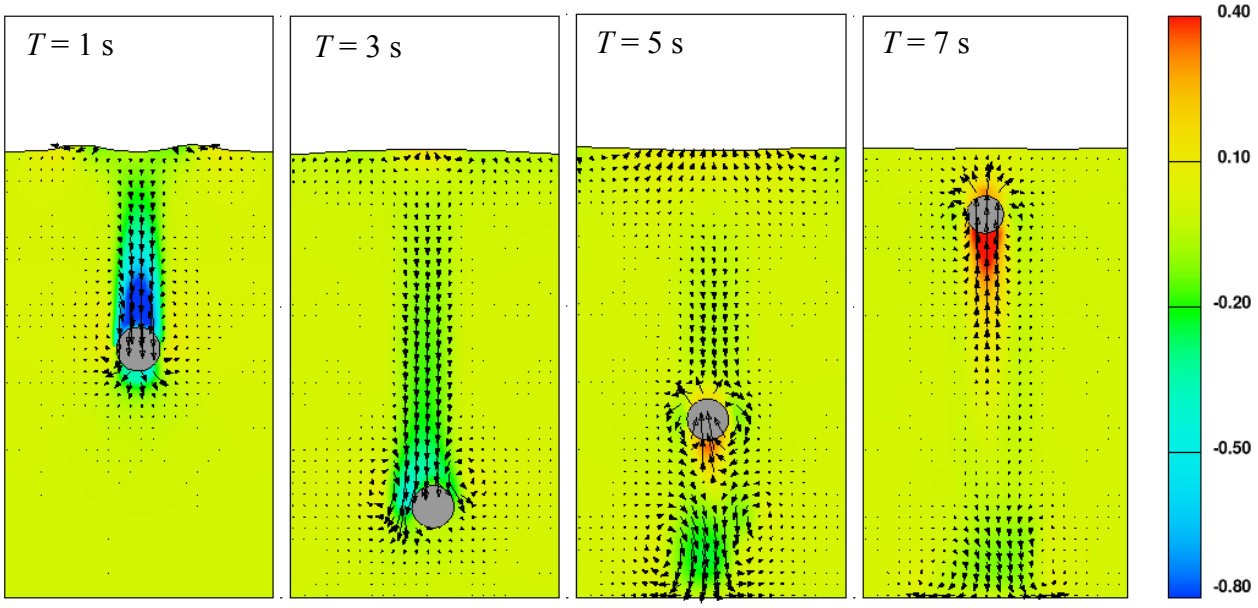

Figure 11.4 Snapshots from simulation with free-falling oil lump. Colours represent the vertical component of the fluid velocity. Case with D = 0.2 m, h = 0.4 m, ρ = 984 kg/m³, ρ_w = 1025 kg/m³.

Time-series of the lump position and velocity are shown in Figure 11.5. The figure also shows the position and velocity computed from the drag equation

$$\dot{w} = \frac{1}{\rho + C_M \rho_1}\left[(\rho - \rho_1)\cdot g - \frac{1}{2} C_D \rho_1 \mid w \mid w \cdot \frac{Area}{Vol}\right], \qquad (1)$$

were ρ is the density of the lump and ρ_1 is the density of the ambient ($\rho_1 = \rho_a$ =1.5 kg/m^3 in air and $\rho_1 = \rho_w$ = 1025 kg/m^3 in water). The projected area to volume ratio is $Area/Vol = 3/(2D)$ for a spherical lump. An explicit numerical solution was made of (1). With the drag coefficient set to C_D = 0.4 and the added mass coefficient set to C_M = 0.5, equation (1) is seen to predict the position of the lump in good agreement with the simulation for two different cases.

The slower initial rise (and longer duration of submergence) of the lump in the Flow-3D simulation compared to the solution of (1) can be explained by the fact that it has to rise through its own wake. (No ambient flow is assumed in (1)).

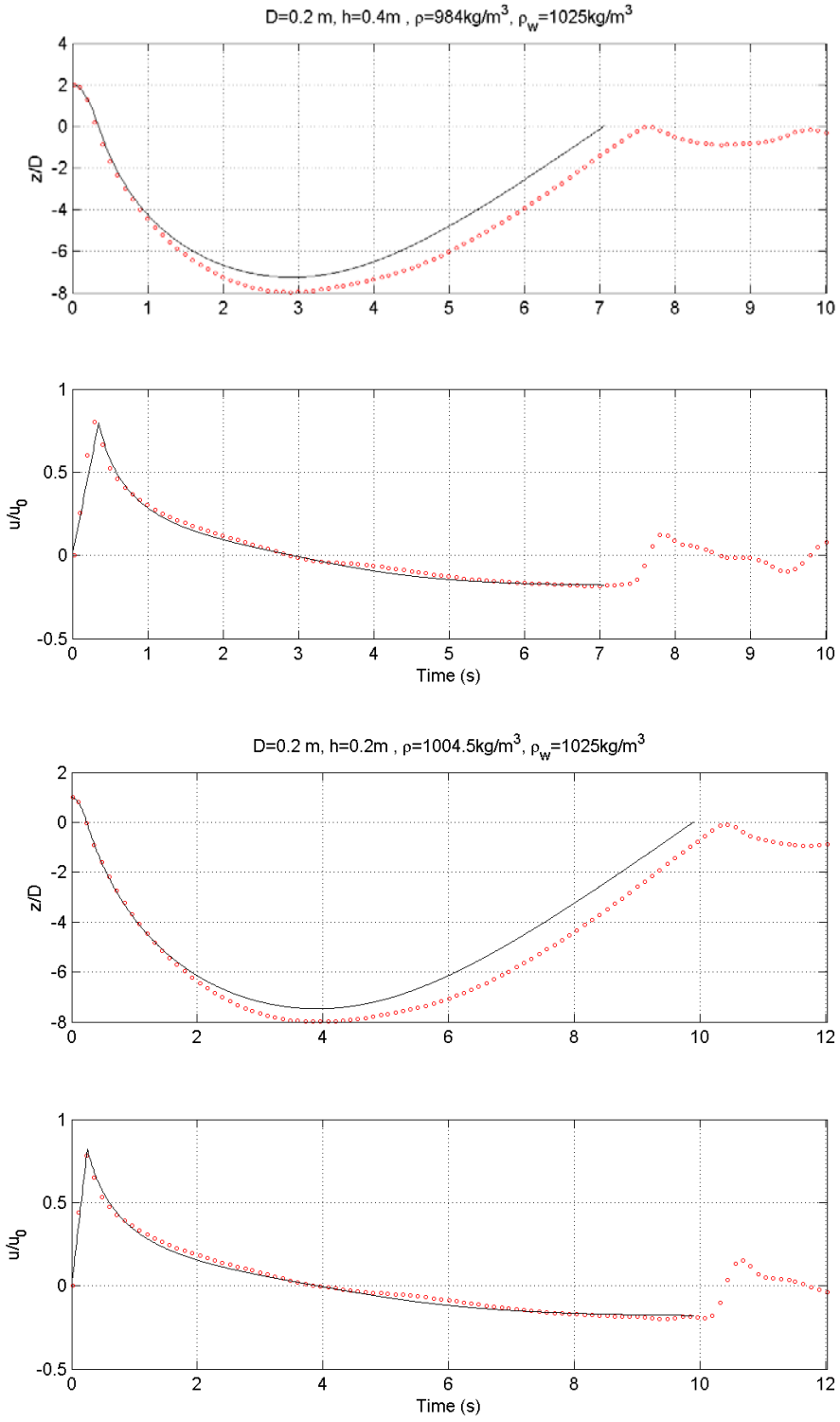

Figure 11.5 Vertical position and velocity of free-falling lump. Comparison of Flow-3D result (full line) with result from (1). Scaling with lump diameter D and max free-fall velocity $u_0 = (2gh)^{½}$. Two different cases with parameters as indicated.

Figure 11.6 shows maximum submergence depth and immersion time as a function of density difference and fall height predicted with the drag formula (1).

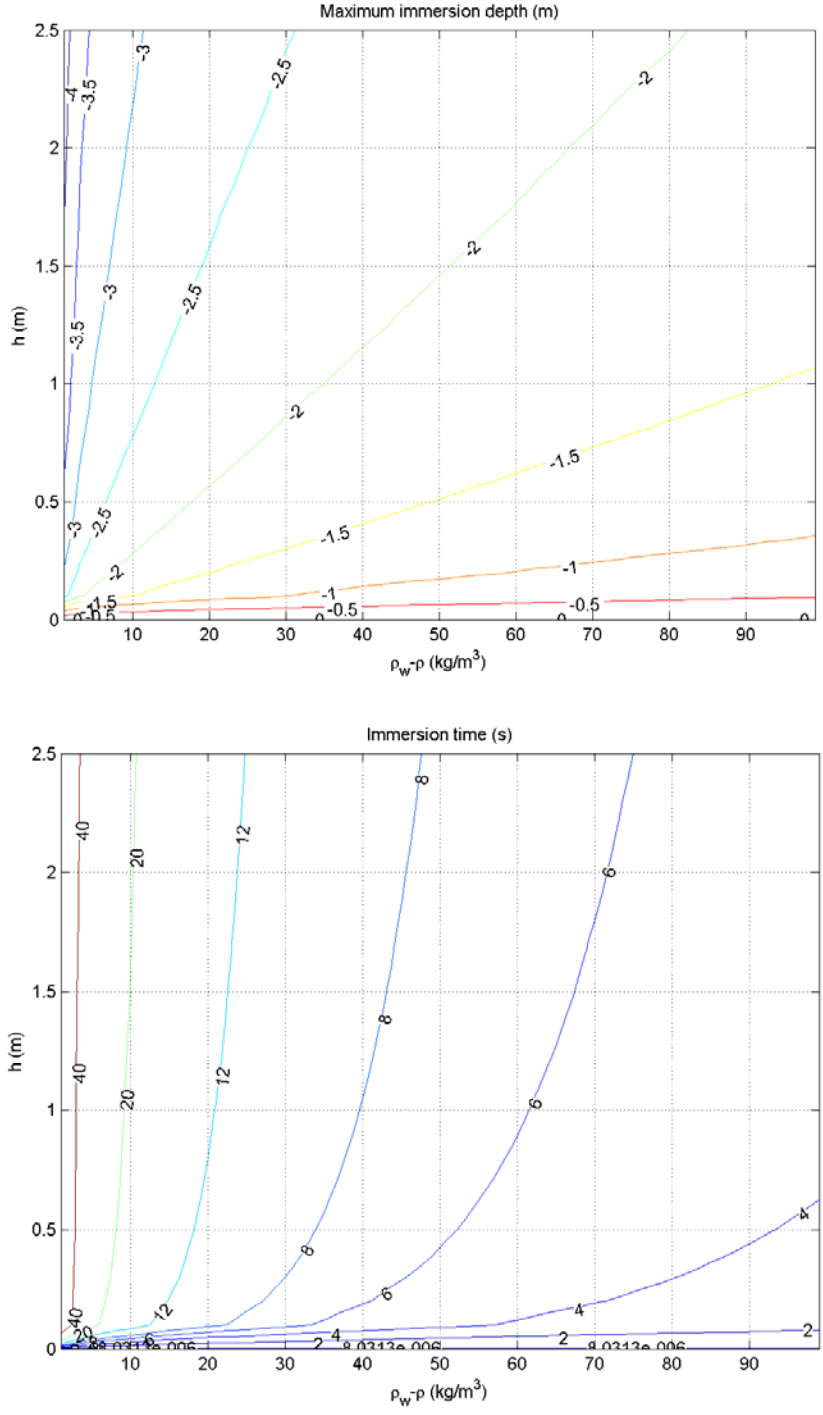

Figure 11.6. Maximum submergence depth (upper plot) and time (lower plot) of a falling lump as a function of density difference and height. Computed from (1) with D = 0.2 m and ρ_w = 1025 kg/m^3.

11.6 Free-falling water

In order to check the effect of free-falling water (assumed to be coming from the crest of a breaking wave) hitting a floating lump, a similar setup to that in Subsection 11.5 was made. The initial condition is a spherical $D = 0.2$ m volume of water falling from a height h onto a floating oil lump, as shown in the first frame of Figure 11.7.

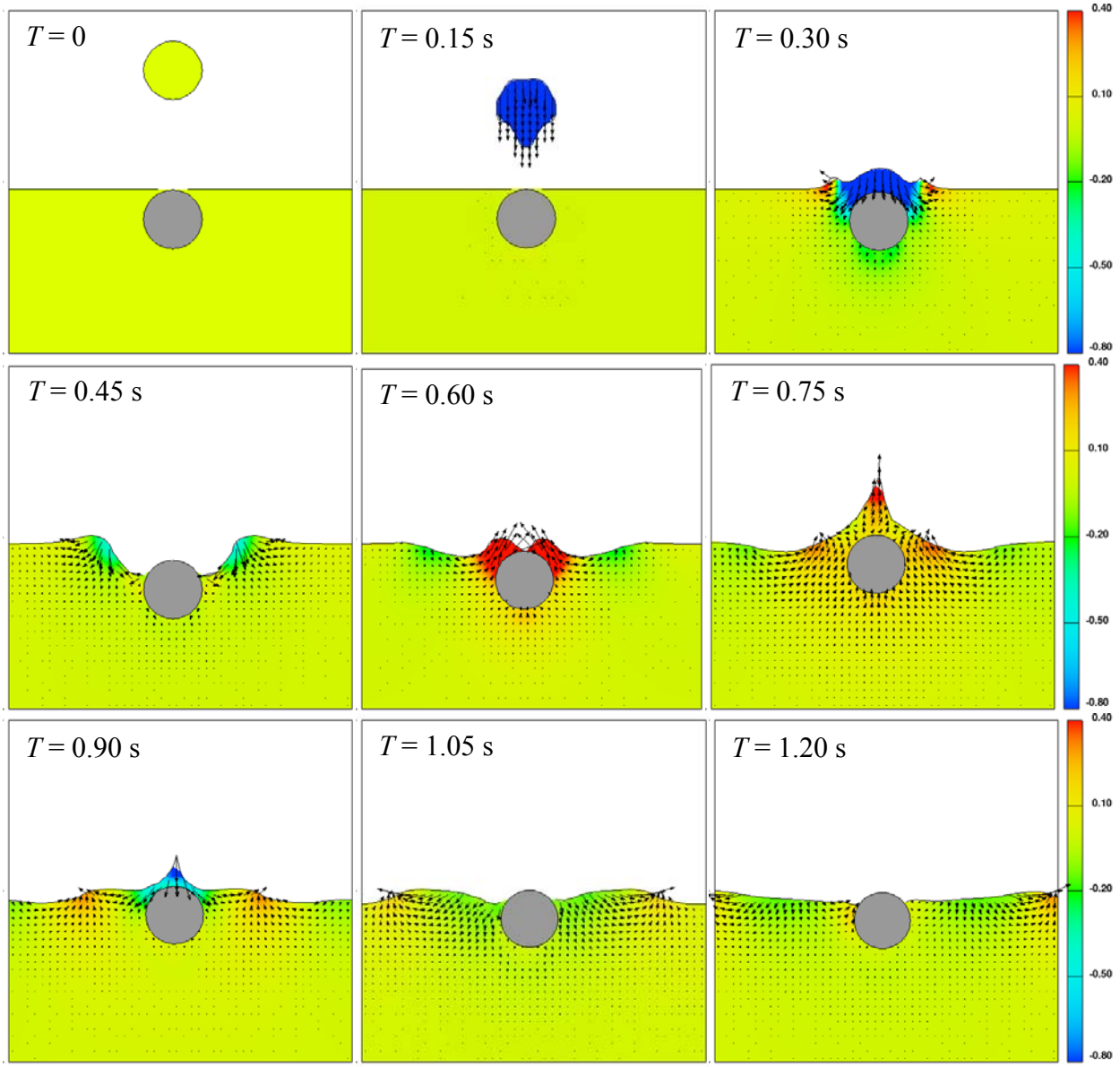

Figure 11.7. Snapshots from simulation with water free-falling on oil lump. Colours represent the vertical component of the fluid velocity. Case with D = 0.2 m, h = 0.4 m, ρ = 984 kg/m^3, ρ_w = 1025 kg/m^3.

The impact of the water proved to have little effect on the lump, pushing it a maximum of only 0.05 m (0.25D) downwards at time $t \sim 0.45$ s, see the time-series in Figure 11.8. At this time, the downward momentum of the water has been diverged outwards, and has generated a trough in the water. While the

lump rises and overshoots its equilibrium position, this trough collapses and generates a “fountain”. It can be seen directly above the lump at $t \sim 0.75$ s. At the end of the sequence, the lump is moving downwards for the second time, towards its equilibrium. The submergence time is only about 0.35 s.

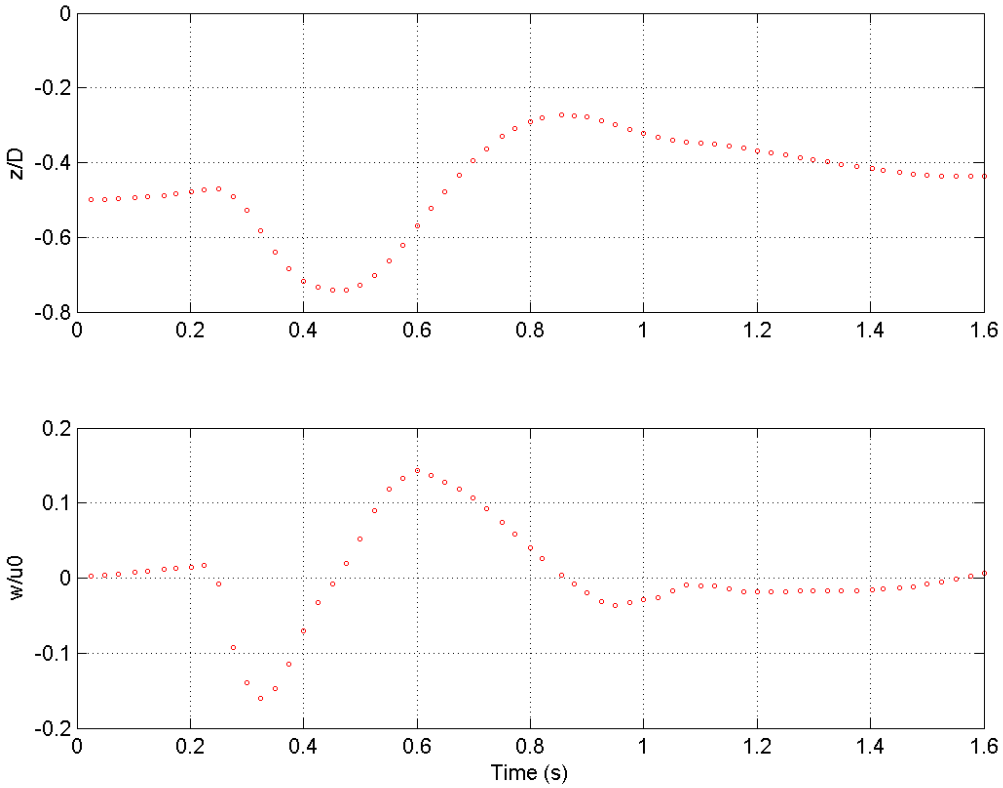

Figure 11.8Vertical position and velocity of oil lump being hit by free-falling water. Scaling with lump diameter D = 0.2 m and max free-fall velocity $u_0 = (2gh)^{½} = 2.8$ m/s. Case as Figure 11.7.

Figure 11.9 shows an animation of the simulation.

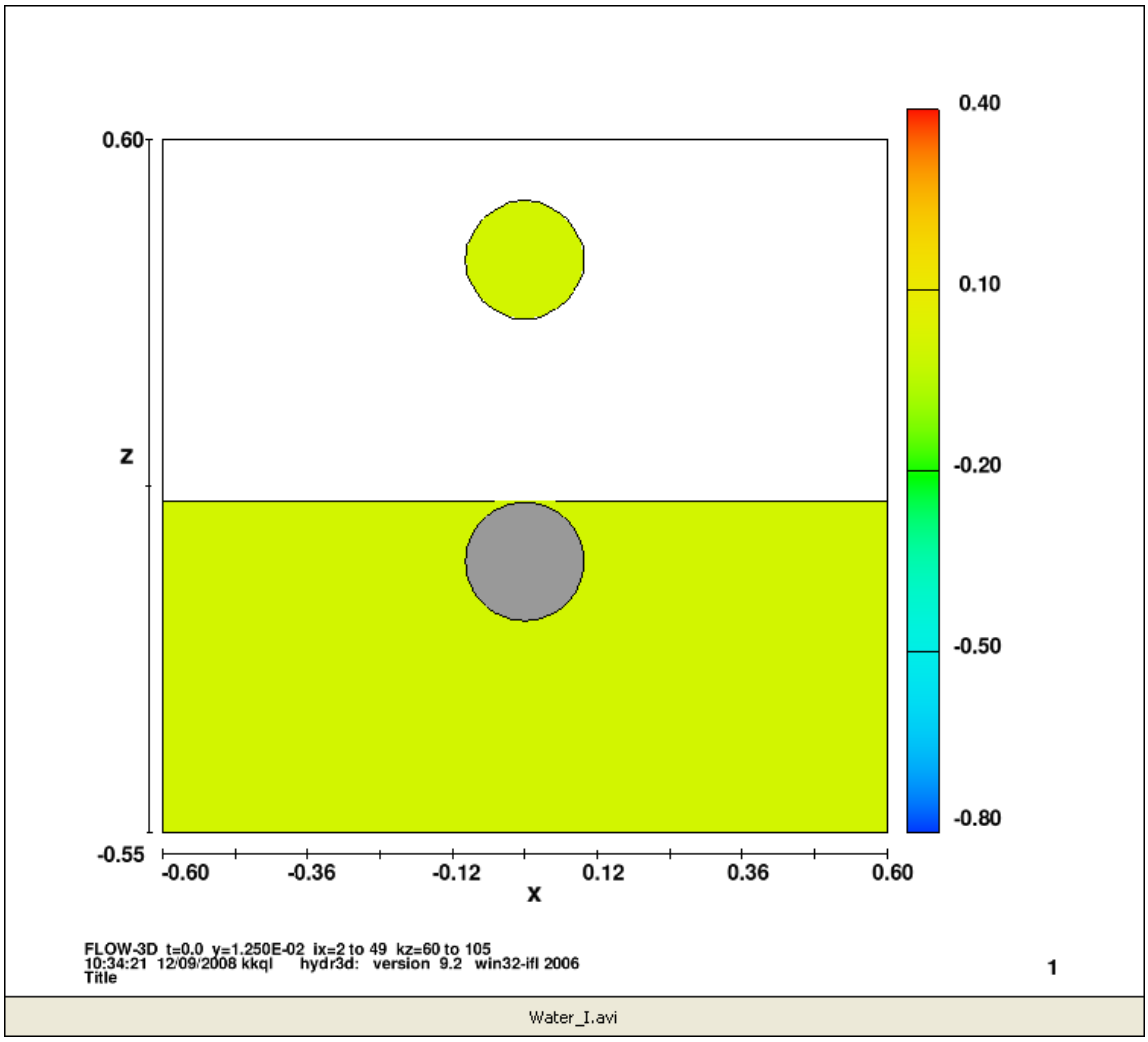

Figure 11.9Initial position and animation of free-falling water hitting oil lump simulation. Colour denotes z-component of velocity. D = 0.2 m, h = 0.4 m, ρ = 984 kg/m^3, ρ_w =1025 kg/m^3 (density of lump 4 % less than water). Double-click figure for animation.

11.7 Summary and conclusions

The motion of a floating sphere (representing a lump of emulsified oil with density on the order of 0.98 times the density of water) was simulated in a "numerical wave tank". It was predicted to stay in contact with the surface, and to be moving (and experiencing Stokes drift) as if it were part of the wave. The input wave had a relatively steep but non-breaking sinusoidal form.

In a cluster of three floating spheres, spheres were predicted to interact and occasionally collide with each other. The forces seemed to be directed parallel to the water surface and none of the spheres became immersed. Waves probably have to be breaking in order for submergence (or significant over-washing) to occur. (A situation with breaking waves could not be set up with the CFD code version available).

The situation at a braking wave crest was simulated in a simplified manner by (1) letting spheres (oil lumps) free-fall into still water and (2) letting water free-fall onto floating spheres. Free-falling lumps (1) were found to go deeper (by a factor of ~ 30) and stay immersed far longer (by a factor of ~ 20) than lumps being hit by water with the same momentum. This indicates that the transfer of momentum from falling water to a floating sphere of similar size is inefficient, and probably on the order of 5 %.